FÍSICA

Revista Cubana de Física

Sociedad Cubana de Física
y Facultad de Física,
Universidad de La Habana

Vol.33 No.1
Julio, 2016

LA FÍSICA EN IMÁGENES

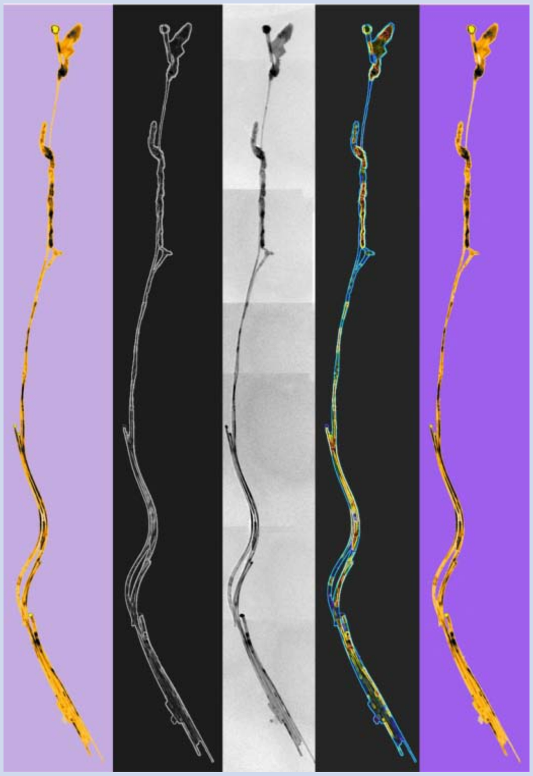

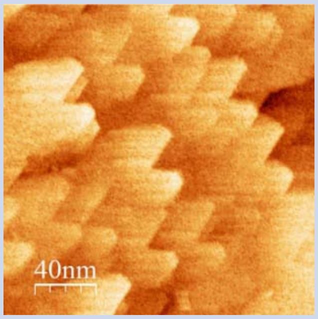

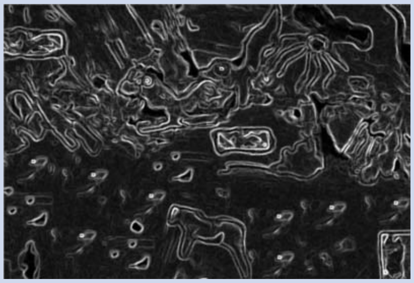

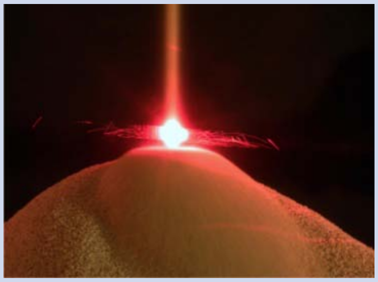

Revista Cubana de Física
ISSN 0253-9268
Online ISSN 2224-7939

REVISTA CUBANA DE FÍSICA
Vol. 33, No. 1, (Julio 2016)
ISSN 0253-9268 Online 2224-7939

Portada: Collage de fotografías ganadoras del concurso CienciArte'2015. Ver la sección "Nuestra Física en noticias", para más detalles.

Todos los artículos en formato -e:
www.fisica.uh.cu/bibloteca

La Revista Cubana de Física es una publicación semestral de la Sociedad Cubana de Física

COORDENADAS

ARTÍCULOS ORIGINALES

***Papers contributed to "Complex Matter Physics: Active Materials, Dynamics and Patterns" (MarchCOMeeting'15). La Habana, June 24 – 26, 2015**
[Contribución al evento "Física de la Materia Compleja: Materiales Activos, Dinámica y Patrones" (MarchCOMeeting'15). La Habana, Junio 24 - 26, 2015]

COMUNICACIONES ORIGINALES

OBITUARIOS

***Papers contributed to "Complex Matter Physics: Active Materials, Dynamics and Patterns" (MarchCOMeeting'15). La Habana, June 24 – 26, 2015**
[Contribución al evento "Física de la Materia Compleja: Materiales Activos, Dinámica y Patrones" (MarchCOMeeting'15). La Habana, Junio 24 - 26, 2015]

NO NEED TO BE FAST AND FURIOUS: A MEETING BETWEEN CUBAN AND U.S. PHYSICAL SOCIETIES OPENS THE ROAD FOR DEEPER RELATIONS

NO HAY NECESIDAD DE SER TAN RÁPIDOS Y FURIOSOS: UNA REUNIÓN ENTRE LAS SOCIEDADES CUBANA Y AMERICANA DE FÍSICA ABRE EL CAMINO HACIA RELACIONES MÁS PROFUNDAS

E. Altshuler

By the end of April, an unusual black helicopter was taking shots at overwhelming speed along Havana's Malecón. On the ground, Chevrolets and Fords from the 1950's were busy playing their role as main characters in Hollywood's super-production Fast and Furious VIII. Indeed, after Obama's visit to Havana with a delegation of the order of 10^3 people on March, 2016, Cuba-U.S. relations have been escalating fast, at least in some very visible ways.

A meeting between members of the Cuban Physical Society (SCF) and the American Physical Society (APS). From left to right: Ernesto Altshuler (Editor of the Revista Cubana de Física), Laura Greene (President-elect, APS), María Sánchez-Colina (President, SCF), Amy Flatten (Director of International Affairs, APS), Juan G. Darias (Vice-president for organizational affairs, SCF), Luis Méndez-Pérez (Vice-president, SCF), Alejandro Cabo (Vice-president, SCF) and Aurora Pérez (Vice-president for financial affairs, SCF). Picture taken on March 8, 2016, at the Colegio San Gerónimo de La Habana (Picture: courtesy of San Gerónimo's staff)

The story of Cuba-U.S. relations in the field of Physics is quite different: they are not escalating so fast, and definitively not so furiously. *There's no need for that*. They have more or less always existed –in a subtler way. A moving article by Irving Lerch (then Director of International Affairs for the American Physical Society, APS) published in 2002 is a nice example of the good feelings between the numerous U.S. physics community and its relatively small Cuban counterpart. It also illustrates that the Cuban-U.S. relations in the field of Physics started to gain momentum by the end of the 20^{th} century. Lerch's[1] article reads: "Nonetheless, this past April, more than 30 U.S. medical physicists participated in an international congress in Havana (International Conference in Medical Physics, April 8-10, 2002) and many more

---

[1] I. Lerch, "Physics in Cuba: Partnerships And A Personal Perspective", APS News, August-September 2002 (http://www.aps.org/publications/apsnews/200208/backpage.cfm)

are expected to attend the VIII Inter-American Conference on Physics Education to be convened July 7-11, 2003, in Havana." Miriam Sarachik, then President of the APS, participated in the latter, as well as Charles H. Holbrow, President of the American Association of Physics Teachers (AAPT), who later wrote: "Havana's cars may be old, but the conference's physics and physics pedagogy were up-to-date. Physics teachers from 14 countries in the Western Hemisphere and 12 in Europe, Africa, and Asia presented more than 200 talks and posters"[2]. Nobel laureate Leon Lederman also attended the meeting, and even gave an interview to the Cuban press. More recently, U.S. physicists have participated in scientific gatherings in Cuba –one of the biggest being Physics and Applications of High Brightness Beams, that took place in Havana, from March 28 to April 1, 2016.

A much smaller event, however, may be more significant for the future of the Sociedad Cubana de Física (SCF). Last March, Laura Greene (President-elect of the APS) and Amy Flatten (Director of International Affairs of the APS) participated in the Latin American Workshop on Physics Teaching (TIBERO'16), organized by the Physics Faculty, University of Havana. They used the opportunity to meet with the Direction Board of the Sociedad Cubana de Física (SCF), following an invitation by its president, María Sánchez-Colina. The meeting, which took place at the Colegio Universitario San Gerónimo de La Habana –a branch of the University of Havana– was devoted to explore future roads for cooperation, in a relaxed and friendly environment. Some ideas were discussed and the Cuban physicists identified three main goals of cooperation with the APS:

1. Connecting young Cuban physicists with their U.S. counterparts.
2. Inviting senior U.S. physicists to teach courses in Cuban universities.
3. Finding ways to collect equipment donations and send them to Cuban physics institutions.

The APS has concrete plans for addressing each of these goals in the upcoming year. In 2017, APS will host a meeting of North American and Cuban physics graduate students in Washington, D.C. It also has established programs for sending senior physicists to Brazil and India, and hopes to use that as a model for future Cuban programs. It is also working with other scientific organizations toward collecting equipment donations and finding possible ways to transport them to Cuba, a nontrivial matter: while diplomatic relations between U.S. and Cuba have been successfully reopened, there are still serious restrictions as part of the embargo[3].

A massive opening to U.S. Physics is not, however, a trivial matter. Due to the small size of the Cuban community of physicists, it may provoke the downsizing of the exchange with Europe and some Latin American countries like México and Brazil, which has flourished during the last couple of decades. It would also contribute to the already worrying emigration of young Cuban physicists to places with much better scientific infrastructure and economical benefits at the personal level. Those elements were also approached during the meeting between the SCF and APS members. However, the proximity of research institutions in the U.S. to Cuba, can help facilitate to train students and provide collaborations in large facilities, such as the National High Magnetic Field Lab in Florida, where Laura has just joined.

Beyond technical matters, we had the opportunity to get a feeling of the pleasant personality and human warmth of both Laura and Amy during and outside the meeting. If it is a hint of the future relations between Cuban and U.S. Physics, there must be an uplifting future in the bilateral relations.

The author thanks useful comments of María Sánchez-Colina, Laura Green and Amy Flatten.

---

[2] Ch. H. Holbrow, "Across a Bridge to Cuba", Announcer, Vol. 33, issue 3, 2003 (http://www.aapt.org/aboutaapt/reports/pres-fall03.cfm).

[3] Known as "El bloqueo", in Cuba.

Rev. Cub. Fis. **33**, 4 (2016) ARTÍCULOS ORIGINALES

STRUCTURAL, EPR AND OPTICAL STUDIES ON Cu-DOPED ZnO NANOPARTICLES SYNTHESIZED BY THE SOL-GEL METHOD AT DIFFERENT CALCINATION TEMPERATURES

ESTUDIO ESTRUCTURAL, ÓPTICO Y POR EPR DE NANOPARTÍCULAS DE ZnO DOPADAS CON Cu, SINTETIZADAS POR SOL-GEL, A DIFERENTES TEMPERATURAS DE CALCINACIÓN

Roman Buchheit[a], F. Acosta-Humánez[b] y O. Almanza[b†]

a) Materials Science Department, Technische Universität Darmstadt, Building L2—01 79, Alarich-Weiss-Straße 2, 64287 Darmstadt, Germany
b) Departamento de Física, Grupo de Física Aplicada, Universidad Nacional de Colombia-Sede Bogotá, Carrera 30 No. 45-03, edificio 404, Colombia; mafacostahu@unal.edu.co, oaalmanzam@unal.edu.co[†]
† corresponding author

Recibido 3/9/2015; Aceptado 8/1/2016

In this work, pure ZnO and Cu-doped ZnO nanoparticles ($Zn_{1-x}Cu_xO$, $x = 3\,at.\%$) were synthesized using the sol-gel method at three different calcination temperatures ($T_C = 773\ K$, $823\ K$ and $873\ K$.). The particles were analyzed by atomic absorption spectroscopy (AAS), X-ray diffraction (XRD), electron paramagnetic resonance (EPR) at different measurement temperatures and diffuse reflection spectroscopy (DRS). All samples have wurtzite structure and the formation of a CuO was observed as additional phase. The Cu-doped nanoparticles have smaller size than the pure ZnO particles. EPR analysis shows that in samples of ZnO there is presence of superficial defects ($g = 2.036$, $g = 1.967$ and $g = 1.958$) in increased amount than in doped samples. Both samples shows Zn vacancy with $g = 2.004$.The Cu EPR signal was simulated by an anisotropic Spin-Hamiltonian with the values of $g_\perp = 2.082$ and $g_\parallel = 2.320$ and indicating that the Cu^{2+} ions in the sample have a local configuration with axial symmetry. Cu doped samples reveal a smaller band gap for the Cu-containing samples than for pure ZnO samples. Additionally, the gap of the Cu-containing samples decreases with increasing calcination temperature. Samples calcinated at $823\ K$ are anti-ferromagnetic or ferrimagnetic at temperature lower than $T_N = 139\ K$ while samples calcinated at $873\ K$ suffer a transition from paramagnetism to ferromagnetism which is characterized by a Curie temperature of $\Theta_C = 137\ K$.

En este trabajo fueron sintetizadas nanopartículas de ZnO puras y dopadas con Cu al 3 % át. ($Zn_{0.97}Cu_{0.03}O$), a temperaturas de calcinación T_C de $773\ K$, $823\ K$ y $873\ K$. Se hicieron análisis de espectroscopía de absorción atómica (AAS), Difracción de Rayos X (XRD), resonancia paramagnética electrónica (EPR) en función de la temperatura y reflectancia difusa (DRS). Todas las muestras tienen estructura tipo wurtzita y se observó la formación de CuO, como fase adicional. Las nanopartículas dopadas con Cu tienen menor tamaño que las no dopadas. Análisis de EPR establecen que en las muestras de ZnO hay presencia de defectos superficiales ($g = 2.036$, $g = 1.967$ y $g = 1.958$) en mayor número que las muestras dopadas. Ambas muestras muestran vacancias de Zn con $g = 2.004$. La señal EPR asociada al Cu fue simulada a partir de un Hamiltoniano anisotrópico dando valores de $g_\perp = 2.082$ y $g_\parallel = 2.320$ e indicando que el ión Cu^{2+} está en una configuración local con simetría axial. Las muestras dopadas con Cu presentan un gap electrónico menor a las muestras no dopadas. Adicionalmente es mostrado que a mayores temperaturas de calcinación, este gap disminuye. Las muestras calcinadas a $823\ K$ tienen comportamiento anti-ferromagnético o ferrimagnético para temperaturas por debajo de $T_N = 139\ K$, mientras que las muestras preparadas a $873\ K$ el comportamiento es ferromagnético a temperaturas por debajo de $\Theta_C = 137\ K$.

PACS: magnetic semiconductors, 75.50.Pp. sol-gel processing, 81.20.Fw. Electron paramagnetic resonance (EPR) in condensed matter, 76.30.-v. X-ray diffraction in crystal structure, 61.05.cp. Semiconductors absorption and reflection spectra of, 78.40.Fy

I. INTRODUCTION

I.1. ZnO, A Promising Material

Zinc oxide (ZnO) as a semiconductor material (gap 3.37 eV) has received much attention lately for its possible application in optoelectronics [1–4]. Since zinc oxide in its crystalline form has wurtzite type structure ($a = 0.325$ nm and $c = 0.521$ nm) [1, 4], this is very stable and has properties that make it a promising material for applications in physics as gas sensor [5], solar cells [6], varistors [7] and UV-light emitting devices [8]. Its possible applications in chemistry are the use as photocatalysts [9], in medicine for its antibacterial activity [10, 11], as well as evaluating the toxicity of cancer cells [12, 13]. However, it was found that doping ZnO with transition metals can further improve the properties of ZnO in some cases. In particular, possible applications of doped ZnO could be transparent electrodes [14], spintronics [15] or enhanced photocatalytic activity [16]. Thus, ZnO has been doped with many transition metal elements such as Co [1], Cu [2,3,17], Ni [18], Mn [19] and Eu [20]. These different types of metal-doped ZnO belong to the material group of diluted magnetic semiconductors (DMS), where the doping element changes the electronic, magnetic and structural properties of the ZnO matrix [1,2,21].

One of the interesting candidates for ZnO doping is Cu, forming $Zn_{1-x}Cu_xO$ materials. There are different preparation methods available to produce thin film or powdered forms of Cu-doped ZnO, namely the sol-gel method [22, 23], aqueous solution method [24], auto-combustion method [20], co-precipitation method [3], mild solution method [17], and solid state reaction method [25]. These preparation methods may lead to vary material properties. For producing $Zn_{1-x}Cu_xO$ nanoparticles, the sol-gel method generally provides good material properties and exact control of the dopant concentration together with an easy synthesis process [21, 26].

I.2. Cu-doped ZnO

The research of many other groups showed that very differing electromagnetic properties were found for Cu-containing ZnO. In many cases, X-ray diffraction (XRD) and electron paramagnetic resonance (EPR) studies were used to reveal the nature of the doping material in ZnO. Elilarassi and Chandrasekaran reported successful substitution of Zn^{2+} ions by Cu^{2+} ions in the ZnO matrix, leading to ferromagnetic material properties [2]. In an earlier work, Elilarassi *et al.* explained the measured EPR signal of Cu-containing ZnO with the presence of both Cu^{2+} and Cu^{1+} in the samples [26]. Udayachandran Thampy *et al.* measured an EPR signal of Cu^{2+} ions on octahedrically distorted interstitial sites in the ZnO wurtzite structure [17]. By different spectroscopic investigations, both Jagannatha Reddy *et al.* and Elilarassi and Chandrasekaran were revealed by substituting Cu^{2+} ions on Zn^{2+} sites for their samples [4, 25].An increase of oxygen vacancies in Cu-containing ZnO was reported by Liu *et al.* and it was explained claiming that some oxygen vacancies would be generated by Cu^{1+} substituting Zn^{2+} [21]. Finally, Elilarassi and Chandrasekaran, Udayachandran Thampy *et al.* and Liu et al. found also the presence of a secondary CuO phase in some of the Cu-containing ZnO samples [2, 17, 21].

The variety of results shows that generally many possibilities exist to show how the Cu can be found in Cu-containing ZnO. It is likely that magnetic properties of the material may depend on the manner of incorporation of the Cu^{2+} ions in the ZnO material. Recently, some authors have reported the synthesis and characterization of Cu^{2+}-doped ZnO nanopowders. X-ray diffraction results confirmed the presence of hexagonal wurtzite structure in their samples. From optical and EPR studies the Cu^{2+} ion occupied tetragonally distorted octahedral site symmetry [27].

This paper presents the investigation of $Zn_{1-x}Cu_xO$ nanoparticles, which were produced using the sol-gel method. Samples were calcinated at three different temperatures, so that the influence of the calcination temperature on some structural and magnetic properties will also be examined. Chemical analysis by atomic absorption made possible to determine real stoichiometry of the synthesized materials. XRD diffractograms are used for characterization of the nanoparticles and investigation of present phases in the samples. EPR measurements and simulation are done in order to contribute to the knowledge about the local configuration of the Cu ion in the samples. From results and for the first time, as far as the authors know, it is suggested that the form in which Cu^{2+} enters the matrix can depend on the calcination temperature. So, this investigation contributes to understanding how Cu^{2+} ions may enter into ZnO matrix. Finally, band gap of powder samples is measured by diffuse reflection spectroscopy (DRS), in order to determine possible changes in the electronic structure of the samples.

II. EXPERIMENTAL

Powder samples of $Zn_{1-x}Cu_xO$ with doping molar ratio $x = 3$ at. % and undoped ZnO samples were produced using the sol-gel method. The precursors were copper(ii) nitrate trihydrate ($Cu(NO_3)_2 \cdot 3H_2O$, 99.5 % purity, *Panreac*), zinc(ii) nitrate hexahydrate ($Zn(NO_3)_2 \cdot 6\,H_2O$, 98 % purity, *Panreac*) and citric acid monohydrate ($C_6H_8O_7 \cdot H_2O$, 99.995 % purity, *Merck*). The nitrates were slowly dissolved in stoichiometric quantities in deionised water at $T = 343\ K$. Stoichiometric amounts of citric acid also was dissolved in deionised water and the solution mixed with nitrates solutions at $T = 343\ K$. The mixture was stirred until a gel was formed. Resulting gel was dried at $T = 403\ K$ for $t = 12\ h$, where a temperature ramp of $1\ K/min$ was used during heating to prevent premature crystallization. After drying, the materials were milled using an agate mortar. The powder samples of $Zn_{0.97}Cu_{0.03}O$ and ZnO were finally calcinated at different calcination temperatures $T_C = 773\ K$, $T_C = 823\ K$ and $T_C = 873\ K$ using a temperature ramp of $1\ K/min$. The sample $Zn_{0.97}Cu_{0.03}O$ were named *ZC3TTT*, where 3 stands for the Cu content of $x = 3 at.\%$ and *TTT* the calcination temperature of the sample in Kelvin, i.e. *ZC*3873 describes the $Zn_{0.97}Cu_{0.03}O$ sample with $T_C = 873\ K$. The samples of ZnO were named *Z0TTT*, where 0 represents the absence of doping materials. In the EPR experiments, the names of the samples are followed by three numbers, which indicate the measurement temperature, i.e. ZC3873090 means a measurement temperature of 90 *K* for the sample ZC3873.

Atomic absorption spectroscopy (AAS) was used for analysing chemical composition. After digestion in an aqueous solution (1:3 HCl : HNO_3), the $Zn_{1-x}Cu_xO$ samples were measured between 213.9 *nm* and 324.8 *nm*. X-ray diffraction (XRD) experiments were done for the samples with T_C =823 *K* and $T_C = 873\ K$ using a Panalytical X'Pert PRO diffractometer. In the experiment, Cu-K_α radiation ($\lambda_{K_\alpha} = 0.1540598\ nm$) and Bragg-Brentano configuration were used, the measurements range was from $2\theta_0 = 10^o$ up to $2\theta_1 = 90^o$ with a step size of $\Delta\theta = 0.0263^o$ and total counting time of the detector of $t = 97.920\ s$. Lattice parameters were determined by Rietveld refinement using *Fullprof* [28].

The sample with T_C =873 *K* was analyzed by Electron Paramagnetic Resonance (EPR) using a Bruker ESP 300 Spectrometer at X-band. The measurements were done with microwave frequency of $\nu = 9.44\ GHz$ and power microwave of $P_w = 20\ mW$, with a modulation frequency of $f = 100\ kHz$ and a modulation amplitude of $A_m = 1.0488\ mT$. The spectra was measured in a sweep width of the magnetic field $\Delta H = 500\ mT$ and a resolution of 4096 points per spectrum in a temperature range from $T = 90\ K$ up to room temperature.

Additionally to the EPR measurements, simulations were done using *MATLAB R2012b* with the *EasySpin 4.5.5* toolbox [29].

Finally, all samples were investigated by DRS using a *Varian Cary 5000* UV-vis spectrometer. The scanning interval was $\lambda_0 = 2500\ nm$ (infrared) to $\lambda_1 = 300\ nm$ (ultraviolet) with a measurement time per step of $\tau_m = 0.1\ s$ and a step interval of $\Delta\lambda = 0.1\ nm$.

III. RESULTS AND DISCUSSION

III.1. AAS Results

The real chemical composition determined by atomic absorption spectroscopy (AAS) was determined by following expression:

$$x = \frac{\eta_{Cu}}{\eta_{Zn} - \eta_{Cu}} \times 100\,\% \tag{1}$$

Where x is doping molar ratio, η_{Zn} is moles of zinc and η_{Cu} moles of copper. Then, $x = 3.45\,at.\,\%, 3.45\,at.\,\%$ and $3.44\,at.\,\%$ were obtained for all Cu-doped samples with $T_C = 773K, 823K$ and $873K$ respectively. So, all samples showed a good agreement of the experimental chemical composition with the nominal value $x = 3\,at.\,\%$.

III.2. XRD Results

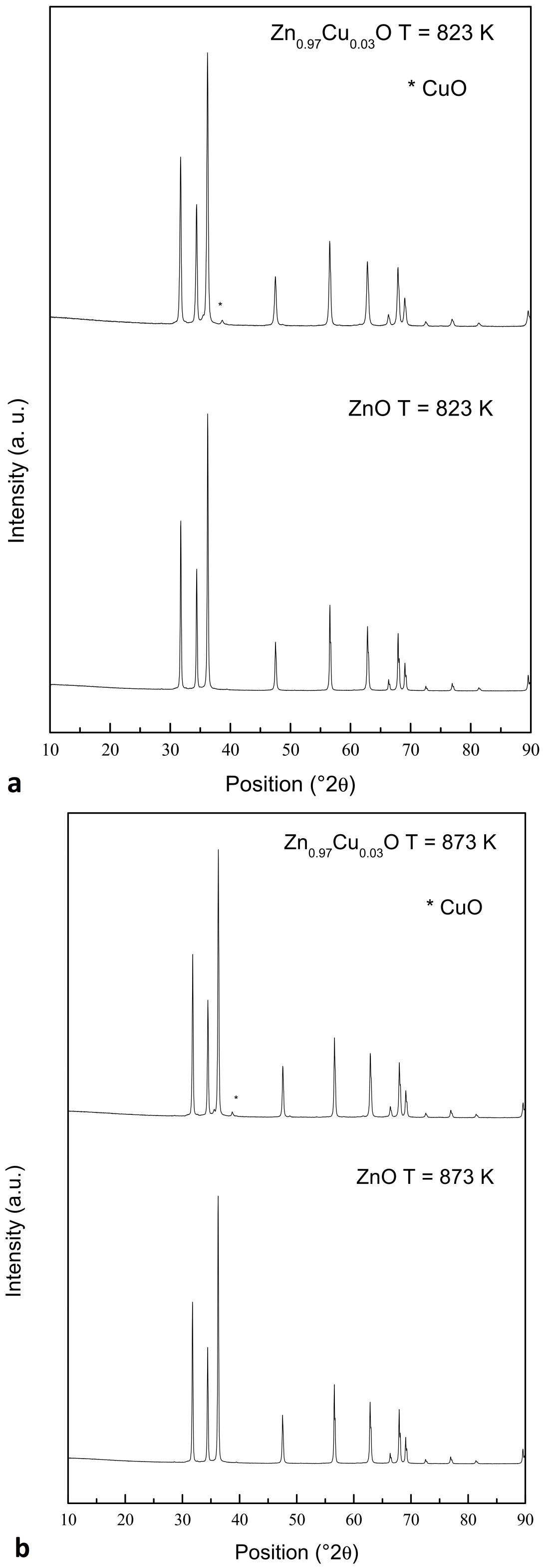

Figure 1. Measured XRD spectra for the samples calcinated at temperature of T_C = 823 K and T_C = 873 K.

The measured XRD spectra for the samples studied are shown in Figure 1(a) and Figure 1(b).

The samples show peaks identifying ZnO in hexagonal wurtzite structure (card JCPDS 36-1451) and very low intensity peaks of copper (II) oxide (card PDF048-1548). Semiquantitative analysis was used for calculating the relative percentage of phases [30]:

$$X = \frac{A_x I_x}{A_s I_s} S \tag{2}$$

Where X is phase percentage in samples, A is mass absorption coefficient and I is apparent density for sample (x) and standard (s). Using the PDF-cards 01-089-0511 for ZnO and 98-00-0316 for CuO gives a relative percentage of the CuO phase of about 5 % in the doped samples. Scherrer's equation [31]

$$D_S = \frac{0.94\lambda_{X-ray}}{\beta \cos\Theta} \tag{3}$$

was used to determine the diameter of the nanoparticles D_S by the experimental spectra, where λ_{X-ray} is the wavelength of the X-ray, β is the full width of half of its maximum intensity (FWHM) of the peaks and Θ is the diffraction angle of the peaks. Taken account the instrument influence to the peak broadening β_i, β was recalculated by the measured peak broadening β_m using the equation [31]

$$\beta = \sqrt{\beta_m^2 - \beta_i^2} \tag{4}$$

D_S was then finally determined using a linear fitting in the $1/\beta$ vs. $\cos\Theta$ plot. The results are shown in Table 1. For all T_C, the samples show a smaller particle size for ZnO with Cu-doping than for pure ZnO. This is in agreement with the observations made by other groups [2, 4, 26]. Furthermore, the particle size is smaller with increasing T_C.

Table 1. Mean particle size, D_S, was extracted from XRD data with Eq. 3. a, c and V were determined from Rietveld refinement. Strains (ϵ) were computed using Eq. 5

Sample	D_s (nm)	a (nm)	c (nm)	V (nm^3)	c/a	ϵ (%)
ZC3823	31.6	0.3250	0.5206	0.04763	1.602	0.0768
Z0823	35.1	0.3251	0.5208	0.04765	1.602	0.0384
ZC3873	25.3	0.3252	0.5208	0.04769	1.602	0.0384
Z0873	33.7	0.3251	0.5208	0.04766	1.602	0.0384

$$\epsilon = \frac{c - c_0}{c_0} \times 100\,\% \tag{5}$$

Figure 2 shows the diffraction peaks (101) and their displacement due to introduction of Cu atoms in ZnO matrix. In Figure 2a the peak related to Cu-doped sample is shifted to the left and has lower intensity that the corresponding peak for ZnO pure.

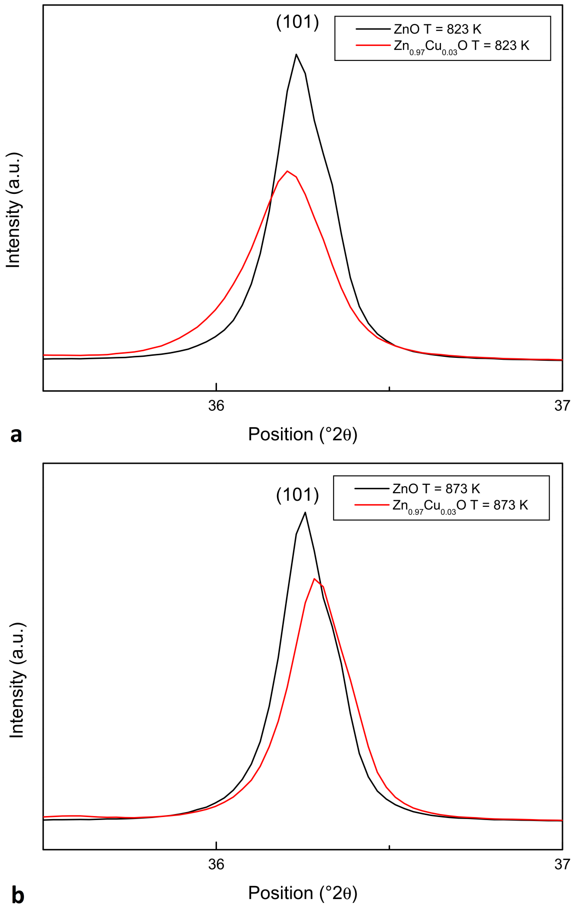

Figure 2. XRD peaks displacement. (a) Samples calcinated at T_c = 823 K. (b) Samples calcinated at T_c = 873 K.

It could be due to microstrains generated by stoichiometric gradient since this first sample is less crystalline. In contrast, for samples calcinated at 873 K the shifting is to the right and could be due to difference between zinc and cooper ionic radius size (Figure 2b). Microstrain values were computed using Eq. 5 [32] and are listed in Table 1.

The lattice parameters of the samples were determined by Rietveld refinement. The parameters a and c, together with the unit cell volume V, are listed in Table 1. For all samples, the c/a ratio is higher than the literature value of c/a = 1.60 for an ideal ZnO structure [33]. This may be explained if we accept the existence of microstrains and defects in the crystal structure. The lattice parameters and the unit cell volume is not depending on T_C or on the presence of the doping element.

III.3. EPR Results

This section presents the results of the EPR investigation of the samples with T_C = 823 K and T_C = 873 K. The EPR spectra for ZC3873 and Z0873 at T = 90 K are shown in Figure 3. Some of the spectra for ZC3873 measured at different temperatures are shown in Figure 4. It can be seen that the spectra changes a bit their shape, depending on the measurement temperature. At higher temperatures, a shoulder is appearing at the main drop of the Cu-signal.

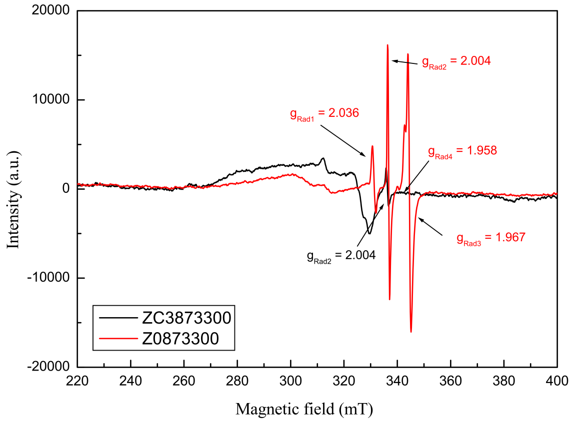

Figure 3. The EPR spectra recorded at T = 90 K for ZC3873 ($Zn_{0.97}Cu_{0.03}O$, black) and Z0873 (ZnO, red).

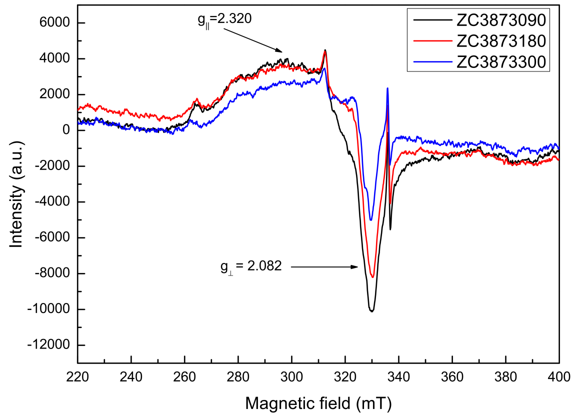

Figure 4. EPR spectra for ZC3873 measured at 90 K (black), 180 K (red) and 300 K (blue).

Z0873 shows only signals from radicals, on contrary to ZC3873, which additionally shows a signal from Cu. Figure 3 shows the g-values for the radicals measured in Z0873 and ZC3873. Z0873 shows radicals at g_{Rad1} = 2.036, g_{Rad3} = 1.967

and $g_{Rad4} = 1.958$, that are connected to shallow donors [4,34] and a radical at $g_{Rad2} = 2.004$, that is generally connected to zinc vacancies (V_{Zn}) [4,35]. ZC3873 only shows a radical at $g_{Rad2} = 2.004$.

The typical signal of *Cu* showed by other authors may differ slightly in shape to the spectra shown in Figure 4, as the Cu^{2+} may be in other configuration [2,4,17,25,26]. Cu EPR signal was indicated in Figure 4 made up of a smaller peak at 290.7 mT ($g_{\parallel} = 2.320$) and a bigger peak at 336.9 mT ($g_{\perp} = 2.082$). At low temperatures, an EPR spectrum is due to Cu^{2+} in axial symmetry.

The *Cu* EPR signal of ZC3873 was described by the Spin Hamiltonian

$$\hat{H} = \beta_e \mathbf{H}^T \cdot \mathbf{g} \cdot \hat{\mathbf{S}} + \hat{\mathbf{S}}^T \cdot \mathbf{A} \cdot \hat{\mathbf{I}}$$

$$= \beta_e \begin{pmatrix} H_x & H_y & H_z \end{pmatrix} \cdot \begin{pmatrix} g_\perp & 0 & 0 \\ 0 & g_\perp & 0 \\ 0 & 0 & g_\parallel \end{pmatrix} \cdot \begin{pmatrix} \hat{S}_x \\ \hat{S}_y \\ \hat{S}_z \end{pmatrix} +$$

$$\begin{pmatrix} \hat{S}_x & \hat{S}_y & \hat{S}_z \end{pmatrix} \cdot \begin{pmatrix} A_\perp & 0 & 0 \\ 0 & A_\perp & 0 \\ 0 & 0 & A_\parallel \end{pmatrix} \cdot \begin{pmatrix} \hat{I}_x \\ \hat{I}_y \\ \hat{I}_z \end{pmatrix} \qquad (6)$$

where β_e is the Bohr magneton, $\mathbf{H^T}$ is the applied magnetic field, $S = \frac{1}{2}$ is the spin magnetic moment for the Cu^{2+} ion (electronic configuration $[Ar]3d^9$), $I = \frac{3}{2}$ is the nuclear magnetic moment for the copper nuclei ^{63}Cu and ^{65}Cu and **g** and **A** are the g and hyperfine tensors, respectively. In Eq. 6, the Spin Hamiltonian was developed for axial symmetry of the Cu^{2+} ion.

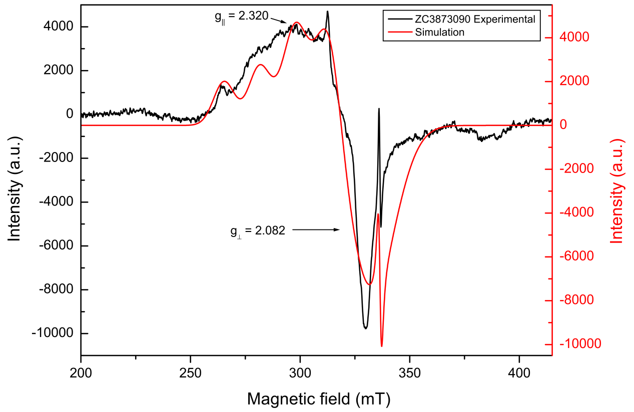

Figure 5. Experimental EPR spectra recorded at $T = 90\ K$ for ZC3873 (black) and the simulation, using the Hamiltonian shown in Eq. 6 and the values in Table 2 (red).

A simulation of the EPR signal together with the experimental spectrum for ZC3873 is shown in Figure 5. Radicals were also simulated using its associated experimental g−values. Table 2 shows the obtained values in the simulation, that best fits in the experimental spectra.

Table 2. Spin Hamiltonian parameters used for the simulation. The values A'_x etc. are derived from the diagonalized hyperfine structure tensor elements via $A'_x = \frac{A_x}{hc}$ etc. with Planck's constant h and the speed of light c.

Sample	$g_\perp$	$g_\parallel$	$A'_\perp$ / MHz	$A'_\parallel$ / MHz	g_{Rad1}	g_{Rad2}	g_{Rad3}	g_{Rad4}
ZC3873090	2.082	2.320	153	516	-	2.004	-	-
Z0873090	-	-	-	-	2.036	2.004	1.967	1.958

As the simulation fits with the experimental spectrum, it is concluded that the main part of the Cu^{2+} ions are in axial configuration. However, it cannot clearly be determined which Cu^{2+} ions are giving the origin of the EPR signal, whether the Cu^{2+} ions belonging to CuO or those which are substituting Zn^{2+} ions on its sites.

In the latter case, the Cu^{2+} ions would have a tetrahedral configuration on its sites in the wurtzite structure. In an ideal case, tetrahedral configuration would create an isotropic symmetry and an isotropic EPR signal. However, as listed in Table 1, the c/a ratio measured by XRD was different from the ideal value. Hence, the Cu^{2+} ions are found in axial symmetry.

The substitution is possible, as the ionic radius for Cu^{2+} with coordination number (CN) $CN = 4$, $r_{Cu^{2+}} = 0.057\ nm$, is very close to the ionic radius for Zn^{2+} with $CN = 4$, $r_{Zn^{2+}} = 0.060\ nm$ [36]. A similar EPR signal for Cu^{2+} ions, that substitute Zn^{2+} ions in the ZnO matrix, was also reported by Elirassi and Chandrasekaran [2,25] and Elirassi *et al.* [26]. However, as it is seen in the XRD results, the sample contains also the CuO phase. CuO has a monoclinic crystal structure with C2/2 symmetry [37]. Therefore, Cu^{2+} ions in CuO are surrounded by oxygen ions in octahedral configuration. Hence, the Cu^{2+} ions in CuO could also give the origin of the anisotropic EPR signal.

The temperature dependence of the signal intensity associated to Cu^{2+} is due to changes in the magnetic coupling between the Cu^{2+} ions. It is why we can plot 1/Area Vs temperature and determine if the coupling is ferromagnetic or other ordering phase. The intensity is proportional to the area of one signal and it was evaluated by double integration of the spectrum between 260 mT and 360 mT. The area from the radicals signals, evaluated between 335 mT and 338 mT, was subtracted from the total integration area of the previous step. The inverse of the intensity, 1/Area, vs. temperature, T, is shown in Figure 6 a and b for samples calcinated at 823 K and 873 K respectively. A linear fit of this curve and the use of the Curie-Weiss law [1,38]

$$I(T) = \frac{C}{T - \Theta_C} \qquad (7)$$

allows the determination of the Curie-Weiss temperature Θ_C, where C is the Curie constant multiplied with the proportionality factor between I and the magnetic susceptibility χ. The linear fit for ZC3823 sample at $T > 210\ K$ is shown in Figure 6a and in figure 6b for ZC3873 sample at $T > 250\ K$. In this last figure a plateau is observed below this temperature. From figure 6a a negative value of T_C

is obtained. This negative value indicates that the Cu−ZnO suffers a transition to an anti-ferromagnetic or ferrimagnetic state at low temperatures. So, now it is necessary adjust the curve with the equation

$$I(T) = \frac{C}{T + T_N} \tag{8}$$

where T_N is the Néel-temperature and C has the same meaning like in Eq. 7. $T_N = 139\ K$ is obtained showing that the Cu^{2+} ions are not strongly magnetically coupled, so that above $T_N = 139$ K the material is paramagnetic. However, when the sample is cooled below $T_N = 139\ K$, a transition to anti-ferromagnetism or ferrimagnetism is expected. In contrast, in the fit for ZC3873 a Curie temperature value of $\Theta_C = 137\ K$ is obtained. This indicates that the Cu^{2+} ions for the sample with $T_C = 873$ K are ferromagnetically coupled.

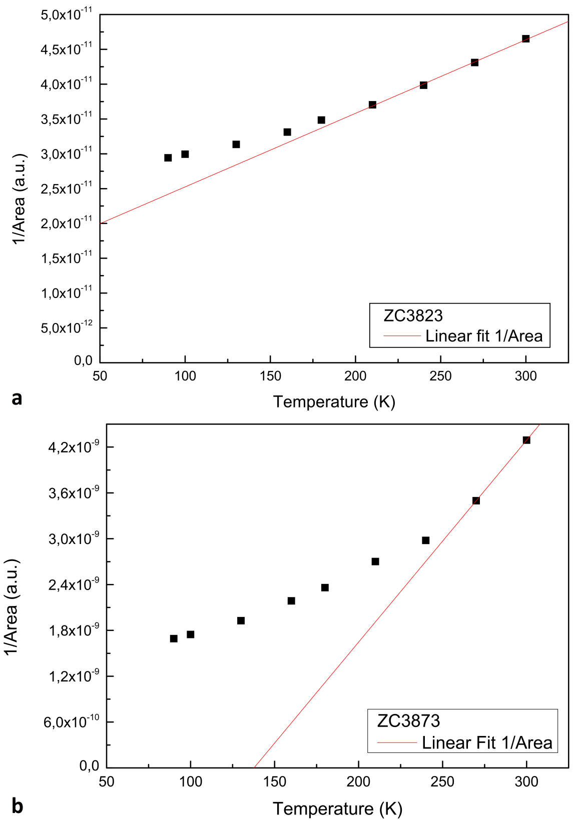

Figure 6. Inverse EPR line intensity of the Cu^{2+} ion depending on temperature for (a) ZC3823, (b) ZC3873.

III.4. UV-DRS Results

UV-Vis spectra for samples calcinated at $T_c = 873\ K$, in the range from 300 nm to 800 nm, are showed in Figure 7. The small absorption ranging from 350-500 nm corresponds to interband transition of ZnO. In case of Cu-doped ZnO samples, it is observed a broad absorption peaks around 600-800 nm associated with $d - d$ transition of Cu^{2+} ions, in addition to ZnO band to band transition [39].

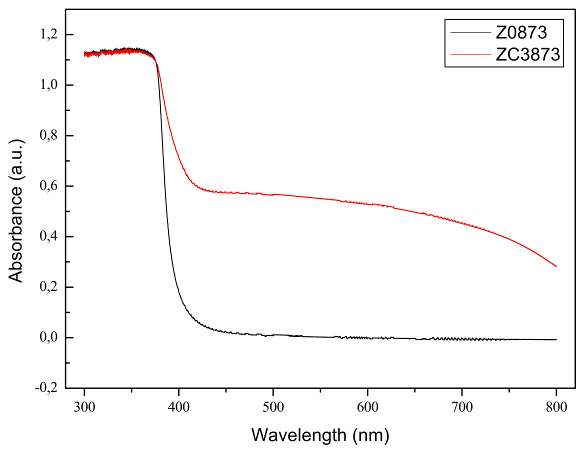

Figure 7. UV-vis spectra for Z0873 (black) and ZC3873 (red).

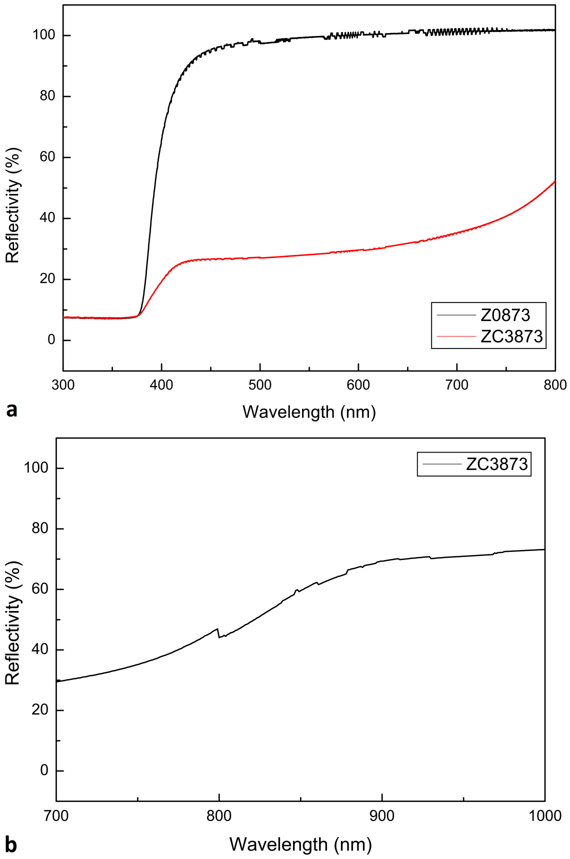

Figure 8. (a) DRS spectra for Z0823 (black) and ZC3823 (red). (b) DRS spectra for ZC3873 sample where signal associated with copper oxide is shown.

The DRS spectra for Z0823 and ZC3873 are shown in Figure 8. The spectra for the other samples studied have similar shape. In order to determine the band gap E_g of the samples, the DRS data were converted using the Kubelka-Munk equation [40]

$$\frac{k}{s} = \frac{(1 - R)^2}{2R} = f(R) \tag{9}$$

where k is an absorption coefficient, s a scattering coefficient and R the measured reflectivity.

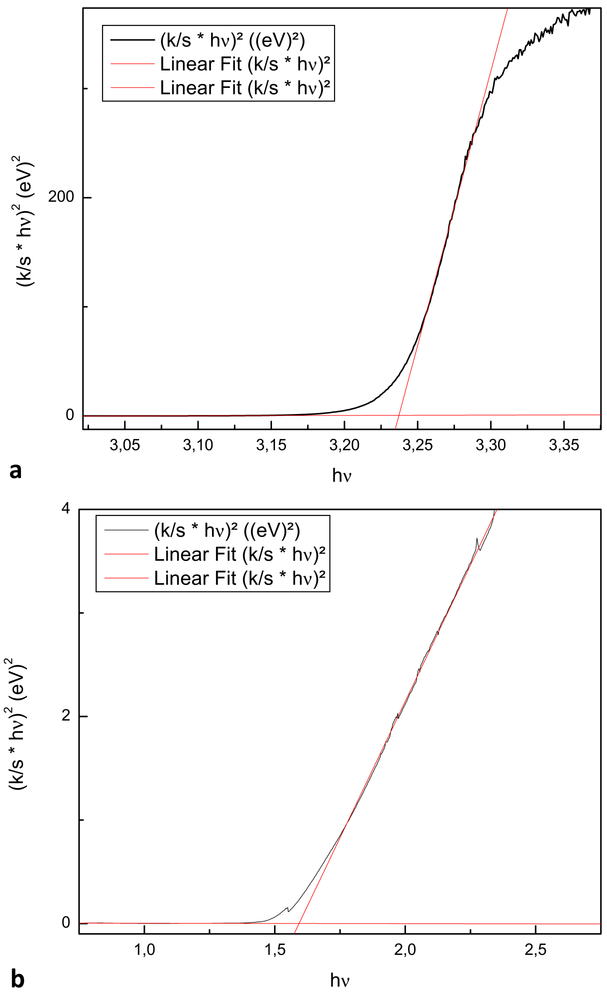

Figure 9. Tauc plots for (a) Z0873 sample. (b) ZC3873 sample.

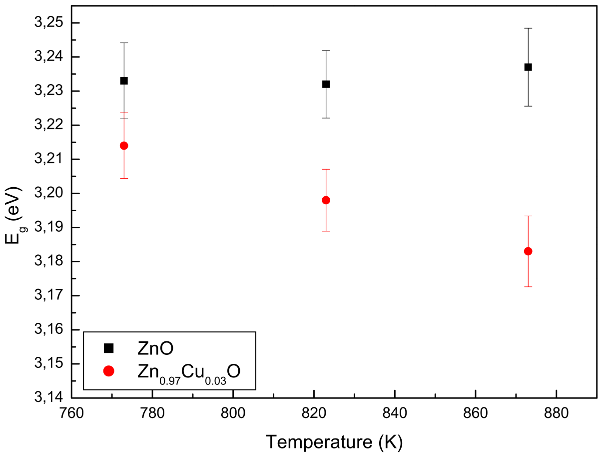

Figure 10. Measured band gap for ZnO by DRS.

The values of Eq. 9 can be used to extract the (optical) band gap of the samples graphically. This is done using a modified Tauc plot, where $\left(\frac{k}{s}\cdot h\nu\right)^2$ is plotted against $h\nu$.This is shown in Figure 9a for the sample Z0873 and Figure 9b for CuO formed in ZC3873 sample.

The measured values of E_g vs. T_C are shown in Figure 10 and in Table 3. It is seen that the Cu-doped samples have a lower band gap than the pure ZnO samples. Furthermore, the band gap of the $Zn_{0.97}Cu_{0.03}O$ samples decreases significantly with T_C.

A band gap at $E_g \approx 1.6\, eV$ was measured in the Cu-containing samples (see Table 3), which is connected to CuO with a band gap of 1.2-1.9 eV [37]. That confirms that some of the introduced Cu^{2+} did not enter the ZnO matrix but formed a CuO phase. That confirms that a small quantity of CuO was formed. However, since Eg related to ZnO lowered with Cu-doping, introduction of Cu atoms in ZnO matrix reduced the band gap. It has been observed by other authors in other materials, as well [39].

IV. CONCLUSION

The experiments show that ZnO nanoparticles with wurtzite phase were synthesized by the sol-gel method. The measured size of the nanoparticles is smaller with $x = 3$ at. % Cu-content than for the pure ZnO samples. However, XRD measurements and the measured band gap by DRS at $E_g \approx$ 1.6 eV revealed the presence of CuO in the Cu-containing samples. In consequence, not all of the Cu^{2+} ions entered the ZnO matrix. However, as the measured band gap by DRS for ZnO was smaller for the Cu-containing samples, it can be concluded, that a part of the Cu^{2+} ions was incorporated in the ZnO matrix and reduced the band gap of the ZnO. Furthermore, the way in which Cu^{2+} ions enter the ZnO samples could be different for the different T_C, as both the band gap for the Cu-containing samples was lower with increasing T_C as the magnetic behavior. The EPR measurements for the sample with $T_C = 873\ K$ show Cu^{2+} ions in axial symmetry, which was confirmed by the simulation with an anisotropic Hamiltonian using the **g** tensor values $g_\perp = 2.082$ and $g_\parallel = 2.320$. It cannot be said that Cu EPR signal is due to Cu^{2+} ions in the CuO phase or due to Cu^{2+} ions substituting Zn^{2+} ions in the ZnO phase, as for both possibilities Cu^{2+} would have an axial configuration. Investigation of the EPR signal intensity depending on the measurement temperature showed that the Cu^{2+} ions in the Cu-containing samples are ferromagnetically coupled when they are calcinated at 873 K. This transition from paramagnetism to ferromagnetism is characterized by the measured Curie temperature $\Theta_C = 137\ K$. If the samples are prepared at 823 K the magnetic behavior is anti-ferromagnetism or ferrimagnetism at temperature lower than 139 K. When magnetic properties of DMS are studied, the obtained results should be taken into account, as the properties do not only depend on the incorporated material, but also on the matter how they enter the matrix or if they form a separate phase and on the calcination temperature T_C.

V. ACKNOWLEDGEMENT

We thank the DIB of the National University of Colombia for the financial support along the project with the code 15848. Additionally, we thank Prof. Mario Barrera for providing the equipment and laboratories used for the material synthesis.

Table 3. Measured band gap E_g by DRS. The Cu-containing samples show a gap related to ZnO ($E_g \approx 3.2\ eV$) and a gap related to CuO ($E_g \approx 1.6\ eV$).

T_C (K)	Gap ZnO (eV)	Error(%)	Gap $Zn_{0.97}Cu_{0.03}O$ (nm)	Error(%)	Gap CuO (nm)	Error(%)
773	3.233	1.11	3.214	0.96	1.563	0.51
823	3.232	0.99	3.198	0.91	1.548	0.78
873	3.237	1.14	3.183	1.04	1.593	0.50

REFERENCES

[1] F. Acosta-Humánez, R. Cogollo Pitalúa and O. Almanza, Journal of Magnetism and Magnetic Materials 329, 39 (2013).

[2] R. Elilarassi and G. Chandrasekaran, Frontiers of Materials Science 7, 196 (2013).

[3] S. Singhal, J. Kaur, T. Namgyal and R. Sharma, Physica B: Condensed Matter 407, 1223 (2012).

[4] A. J. Reddy, M. Kokila, H. Nagabhushana, R. Chakradhar, C. Shivakumara, J. Rao and B. Nagabhushana, Journal of Alloys and Compounds 509, 5349 (2011).

[5] F. Meng, J. Yin, Y.-Q. Duan, Z.-H. Yuan and L.-J. Bie, Sensors and Actuators B: Chemical 156, 703 (2011).

[6] Z. Liu, C. Liu, J. Ya and E. Lei, Renewable Energy 36, 1177 (2011).

[7] K. Hembram, D. Sivaprahasam and T. N. Rao, Journal of the European Ceramic Society 31, 1905 (2011).

[8] Y. Ryu, T.-S. Lee, J. A. Lubguban, H. W. White, B.-J. Kim, Y.-S. Park and C.-J. Youn, Applied Physics Letters 88, 241108 (2006).

[9] N. Daneshvar, D. Salari and A. R. Khataee, Journal of Photochemistry and Photobiology A: Chemistry 162, 317 (2004).

[10] N. Jones, B. Ray, K. T. Ranjit and A. C. Manna, FEMS microbiology letters 279, 71 (2008).

[11] L. Zhang, Y. Jiang, Y. Ding, M. Povey and D. York, Journal of Nanoparticle Research 9, 479 (2007).

[12] M. Premanathan, K. Karthikeyan, K. Jeyasubramanian and G. Manivannan, Nanomedicine: Nanotechnology, Biology and Medicine 7, 184 (2011).

[13] C. Hanley, J. Layne, A. Punnoose, K. M. Reddy, I. Coombs, A. Coombs, K. Feris and D. Wingett, Nanotechnology 19, 295103 (2008).

[14] T. Minami, Semiconductor Science and Technology 20, S35 (2005).

[15] F. Pan, C. Song, X. J. Liu, Y. C. Yang and F. Zeng, Materials Science and Engineering R: Reports 62, 1 (2008).

[16] S. French, A.A. Sokol, S. Bromley, C. Catlow and P. Sherwood, Topics in Catalysis 24, 161 (2003).

[17] U. S. U. Thampy, C. R. Krishna, C. V. Reddy, B. Babu, Y. P. Reddy, P. S. Rao and R. V. S. S. N. Ravikumar, Applied Magnetic Resonance 41, 69 (2011).

[18] R. N. Aljawfi and S. Mollah, Journal of Magnetism and Magnetic Materials 323, 3126 (2011).

[19] A. O. Ankiewicz, M. C. Carmo, N. A. Sobolev, W. Gehlhoff, E. M. Kaidashev, A. Rahm, M. Lorenz and M. Grundmann, Journal of Applied Physics 101, 024324 (2007).

[20] A. Jagannatha Reddy, M. K. Kokila, H. Nagabhushana, C. Shivakumara, R. P. S. Chakradhar, B. M. Nagabhushana and R. Hari Krishna, Spectrochimica Acta Part A: Molecular and biomolecular spectroscopy 132, 305 (2014).

[21] H. Liu, J. Yang, Z. Hua, Y. Zhang, L. Yang, L. Xiao and Z. Xie, Applied Surface Science 256, 4162 (2010).

[22] T. Saidani, M. Zaabat, M. S. Aida, A. Benaboud, S. Benzitouni and A. Boudine, Superlattices and Microstructures 74, 47 (2014).

[23] M. Fu, Y. Li, S. Wu, P. Lu, J. Liu and F. Dong, Applied Surface Science 258, 1587 (2011).

[24] A. Iribarren, E. Hernández-Rodríguez and L. Maqueira, Materials Research Bulletin 60, 376 (2014).

[25] R. Elilarassi and G. Chandrasekaran, Journal of Materials Science: Materials in Electronics 21, 1168 (2010).

[26] R. Elilarassi, P. Sambasiva Rao and G. Chandrasekaran, Journal of Sol-Gel Science and Technology 57, 101 (2011).

[27] B. Babu, T. Aswani, G. Thirumala Rao, R. Joyce Stella, B. Jayaraja and R.V.S.S.N. Ravikumar, Journal of Magnetism and Magnetic Materials 355, 76 (2014).

[28] Rodríguez-Carvajal, J. Fullprof Suite (2012).

[29] S. Stoll and A. Schweiger, Journal of Magnetic Resonance 178, 42 (2006).

[30] K. Norrish and R. M. Taylor, Clay minerals bulletin 5 (28), 98 (1962).

[31] Y. Waseda, E. Matsubara and K. Shinoda, X-Ray Diffraction Crystallography (Springer-Verlag, Berlin Heidelberg, (2011) pp. 123-127.

[32] A. J. Hashim, M. S. Jaafar, A. J. Ghazai and N. M. Ahmed, Optik 124, 491 (2013).

[33] G. Gottstein, Physikalische Grundlagen der Materialkunde, 4th edition (Berlin Heidelberg, 2014), pp. 1-4.

[34] L. S. Vlasenko and G. D. Watkins, Physical Review B 72, 1 (2005).

[35] L. S. Vlasenko, Applied Magnetic Resonance 39,103 (2010).

[36] R. D. Shannon, Acta Crystallographica Section A: Crystal Physics, Diffraction, Theoretical and General Crystallography 32, 751 (1976).

[37] D. Wu, Q. Zhang and M. Tao, Physical Review B: Condensed Matter and Materials Physics 73, 1 (2006).

[38] A. Mauger, Applied Magnetic Resonance 39, 3 (2010).

[39] S. Anandan, N. Ohashi and M. Miyauchi, Applied Catalysis B: Environmental 100, 502 (2010).

[40] A. Murphy, Solar Energy Materials & Solar Cells 91, 1326 (2007).

EFFECTS OF THE LANTHANUM CONCENTRATION ON THE $(Pb_{1-x}La_x)(Zr_{0.95}Ti_{0.05})_{1-x/4}O_3$ ANTIFERROELECTRIC CERAMIC SYSTEM

INFLUENCIA DE LA CONCENTRACION DE LANTANO EN EL SISTEMA CERÁMICO ANTIFERROELÉCTRICO $(Pb_{1-x}La_x)(Zr_{0.95}Ti_{0.05})_{1-x/4}O_3$

Y. Mendez-González[a], A. Peláiz-Barranco[a†], A. Pentón Madrigal[a], J.D.S. Guerra[b], Guo Jie[c], Wang Xiucai[d] y Tongqing Yang[d]

a) Facultad de Física-Instituto de Ciencia y Tecnología de Materiales, Universidad de La Habana. San Lázaro y L, Vedado. La Habana 10400, Cuba; pelaiz@fisica.uh.cu†
b) Grupo de Ferroelétricos e Materiais Multifuncionais, Instituto de Física, Universidade Federal de Uberlândia. 38400-902, Uberlândia – MG, Brazil
c) Electronic Materials Research Laboratory, Key Laboratory of the Ministry of Education, Xi'an Jiaotong University, Xi'an 710049, China
d) Functional Materials Research Laboratory, College for Materials Science and Engineering, Tongji University, 4800 Caoan, Shanghai 201804, China
† corresponding author

Recibido 14/3/2016; Aceptado 14/4/16

Lanthanum modified lead zirconate titanate antiferroelectric ceramics has been studied by using X-ray diffraction, dielectric analysis and ferroelectric hysteresis loops. Both antiferroelectric-orthorhombic (Pbam) and ferroelectric-rhombohedral (R3c) phases co-exist in the studied compositions. The dielectric response has revealed the presence of two peaks in a wide temperature range, which have been associated to different phase transitions. Slim-like hysteresis loops were obtained at room temperature, suggesting a higher stability of the antiferroelectric phase. The hysteresis and dielectric results show that the increase of the La^{3+} ions concentrations disrupts the long-range dipolar order for the ferroelectric phase.

En este trabajo han sido estudiadas cerámicas antiferroeléctricas de circonato-titanato de plomo modificadas con lantano utilizando difracción de rayos-X, mediciones dieléctricas e histéresis ferroeléctrica. Los patrones de difracción de rayos-X muestran, para todas las composiciones, la coexistencia de fases ferroeléctrica con simetría romboédrica (R3c) y antiferroeléctrica con simetría ortorrómbica (Pbam). Los resultados de la respuesta dieléctrica mostraron dos picos en su comportamiento, asociados a diferentes transiciones de fase. La dependencia P-E, a temperatura ambiente, sugiere una mayor estabilidad de la fase antiferroeléctrica. Los resultados de las propiedades dieléctricas y la histéresis ferroeléctrica muestran que el incremento de la concentración de los iones La^{3+} debilita las interacciones de largo alcance que establecen el orden ferroeléctrico.

PACS: Antiferroelectric materials, 77.84.-s; Dielectric properties permittivity, 77.22.Ch; Hysteresis in ferroelectricity, 77.80.Dj

I. INTRODUCTION

The dielectric materials are typically used to increase the energy storage in capacitors. It is also known that for practical applications, high electric breakdown field, large saturated polarization and small remanent polarization are required [1]. From this point of view, it has been considered that antiferroelectric (AFE) materials are potential candidates for electrical energy storage capacitors. These systems, which are characterized by double-like hysteresis loops, possess electric dipoles with antiparallel ordering such that no macroscopic electrical polarization can arise. In the presence of an electric field, an AFE state can be forced into a ferroelectric state, storing large amounts of electrical energy due to the sudden increase in the polarization [1]. AFE materials show interesting physical properties. In addition to their energy storage capacity; they exhibit electrocaloric effect, which is higher than in ferroelectrics and lineal dielectrics. Due to their properties, these systems are very attractive for practical applications such as dielectric capacitors, electrocaloric refrigerators, actuators and transducers [1,2]. Several studies have been performed on these materials [1,3–10]. Lead-containing ceramics, such as lead zirconate [1,5] and modified lead zirconate titanate (PZT) [2,6–14], are considered the most important antiferroelectrics. It has been evaluated, for some systems, that doping by using La^{3+} ions generally provides the stability of the AFE phase over the ferroelectric phase [2,11–14]. The aim of present work is to evaluate the effect of the lanthanum modification on the antiferroelectric phase for $(Pb_{1-x}La_x)(Zr_{0.95}Ti_{0.05})_{1-x/4}O_3$ (x = 0, 1, 2, 3 and 4 at %) antiferroelectric ceramics. Samples are investigated by using structural analysis, dielectric response and hysteresis loop measurements.

II. EXPERIMENTAL PROCEDURE

Ceramics samples of $(Pb_{1-x}La_x)(Zr_{0.95}Ti_{0.05})_{1-x/4}O_3$ (x = 0, 1, 2, 3 and 4 in %) were prepared by the traditional solid-sate reaction method [13]. High purity chemical precursors of PbO (99.9 %, Alfa Aesar), TiO_2 (99.9 %, Johnson Matthey), ZrO_2 (99 %, Merck) and La_2O_3 (99.99 %, Alfa Aesar) were used as starting powders. The mixed oxides were milled for 2 hours, dried and pressed ($1\ ton/cm^2$). Calcination was carried out at 800^oC for 1 hour in air atmosphere. The powders were milled again for 1 hour, dried and pressed (2 ton/cm^2). The sintering was performed in a closed platinum crucible and air atmosphere at 1250^oC for 1 hour. The powder samples were investigated, at room temperature, by using X-ray diffraction (XRD) experiments (Persee XD3 diffractometer, CuKα radiation). It was used a scan step of 0.02^o for 2θ from 10^o to 85^o. Silver painted-electrodes were applied on the parallel faces of the disk-like samples by a heat treatment at 590^oC. The temperature and frequency dependence of the dielectric constant were obtained from room temperature until 350^oC, in a wide frequency range (1 kHz - 1 MHz) by using an LCR meter (IOKI 3532-50). Polarization–Electric field (P-E) hysteresis loops were obtained by using a Radiant system at 10 Hz. The samples were labeled as PLZT x/95/5 for the results and discussion.

III. RESULTS AND DISCUSSION

Figure 1(a) shows the X-ray diffraction patterns (XRD), at room temperature, for the studied ceramics. The indexation is the same for all compositions. It can be seen that both antiferroelectric-orthorhombic (Pbam) and ferroelectric-rhombohedral (R3c) phases co-exist. Figure 1(b) shows two typical regions for a better understanding of the contribution of both phases. An unknown peak (marked with an asterisk) has been found around 28^o, for all compositions. Its origin is currently under study.

The XRD-profile analysis was carried out by using the FullProf Suit software [15], assuming the formation of both phases for the initial structural model. The refinement procedure allowed getting reasonable goodness of fit parameters and a good agreement between the observed and calculated patterns was found. Table 1 shows the unit cell parameters and the unit cell volume (V) for both phases. It can be seen that the lattice parameters depend on the La^{3+} ions concentration. The unit cell volume for the orthorhombic phase increases with the lanthanum content, while for the rhombohedral phase tends to decrease.

Table 1. Values of the unit cell parameters and the unit cell volume for both phases.

Orthorhombic phase (Pbam)	a(Å)	b(Å)	c(Å)	V(Å^3)
PLZT 0/95/5	5.867(2)	11.745(2)	8.207(3)	565.57(6)
PLZT 1/95/5	5.865(8)	11.740(9)	8.208(5)	565.31(1)
PLZT 2/95/5	5.866(1)	11.746(1)	8.213(1)	565.88(2)
PLZT 3/95/5	5.876(5)	11.775(7)	8.224(4)	569.12(8)
PLZT 4/95/5	5.877(4)	11.777(4)	8.227(2)	569.56(9)

Rhombohedral phase (R3c)	a(Å)	b(Å)	V(Å^3)
PLZT 0/95/5	5.837(5)	14.409(9)	425.33(9)
PLZT 1/95/5	5.840(1)	14.407(1)	425.55(4)
PLZT 2/95/5	5.836(4)	14.418(5)	425.38(2)
PLZT 3/95/5	5.835(2)	14.384(2)	424.16(2)
PLZT 4/95/5	5.836(7)	14.388(0)	424.60(9)

The temperature dependence of the real part of the dielectric permittivity (ϵ') is shown in Figure 2, for several frequencies. It can be seen two peaks or anomalies, which could be associated to different phase transitions in the studied temperature range. The observed behavior has been previously reported for PLZT systems [14, 16–18], with an anomaly at lowers temperatures (T_1) and a maximum at the temperature corresponding to ε'_{max} values (T_m). No frequency dependence for T_m is observed.

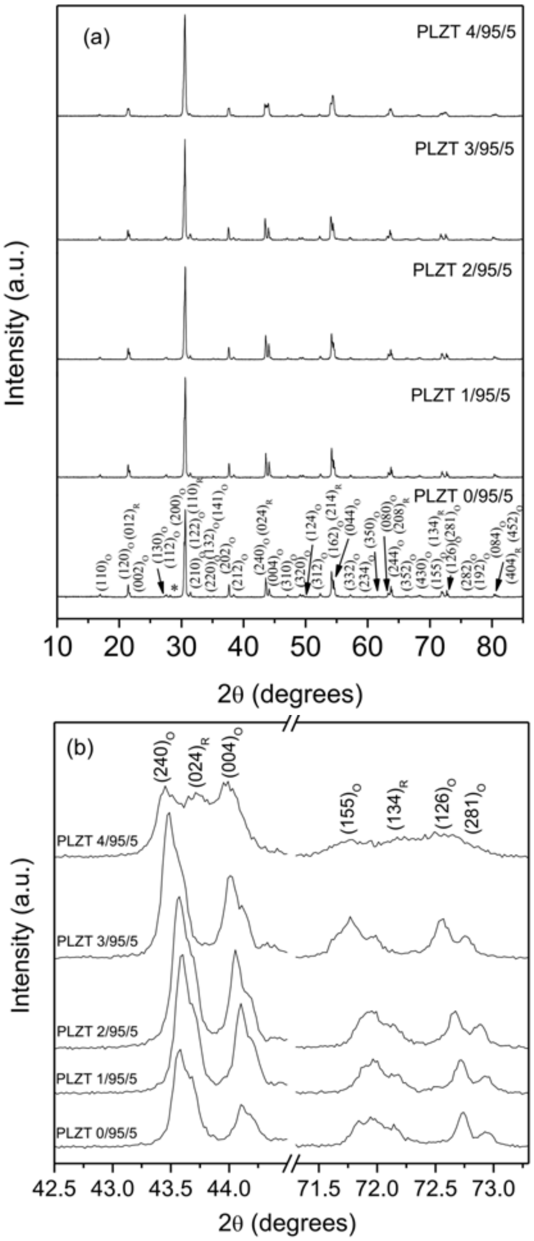

Figure 1. (a). X-ray diffraction patterns, at room temperature, for the studied ceramics; (b) zooms of two XRD pattern regions, 42.5^o – 44.5^o and 71.3^o – 73.3^o.

For doping values up to 2 at%, the T_m values shifts toward lower temperatures with increasing of the La^{3+} ions concentration, reaching a minimum and then increases for higher lanthanum concentrations (see Table 2). This increase could be associated to the increasing of T_1 values for PLZT 3/95/5 and PLZT 4/95/5 or a possible incorporation of a fraction of the rare-earth at B-sites considering that the 6-coordination ionic radius for La^{3+} is 104.5 *pm*, which is greater than that of the ionic radius for Ti^{4+} (61 *pm*) and Zr^{4+} (72 *pm*) [19–21]. Furthermore, a broadening in the dielectric permittivity peaks was observed with the increase of the La^{3+} content. This broadening can be attributed to various factors, such as compositional inhomogeneity, structural disorder and microstrains [22].

Table 2 shows the dielectric parameters for the studied compositions. Clear composition dependence is observed for T_1 and T_m values. With increasing of rare earth concentration, the low-temperature phase transition shows a tendency to increase.

On the other hand, the increase of the La^{3+} ions content causes a strong decreasing of ϵ'_{max} values (see Table 2). This behavior has been also noticed for PLZT x/90/10 [14]. It could be associated with the grain size variation when the lanthanum concentration increases [23]. Scanning Electron Microscopy measurements have showed a decrease in the grain size with the increase in rare earth content for the studied compositions. A decrease in the grain size provides an increase in the volume fraction of the grain boundaries. Then, a clamping of the domain walls at the grain boundaries from its neighbors becomes stronger, making it more difficult the orientation of the domains. The domain wall mobility will decrease, leading to a decrease in the real dielectric permittivity with the grain size.

Table 2. The dielectric parameters for the studied samples.

Samples	$T_1(^oC)$	$T_m(^oC)$	$\epsilon'(1kHz)$	$T_{\epsilon''max}(^oC)$
PLZT 0/95/5	99	244	8309	244
PLZT 1/95/5	133	221	6808	221
PLZT 2/95/5	127	213	3951	213
PLZT 3/95/5	205	234	1556	232
PLZT 4/95/5	213	244	697	240

Another factor that could be inducing the ϵ'_{max} behavior is the influence of the lanthanum concentration on the dipole moment of the system. The La^{3+} ions replace the ferroactive Pb^{2+} ions. Due to the difference in charge and size between these ions, the dipole moment value is affected and thereby the polarization and the real part of the dielectric permittivity values.

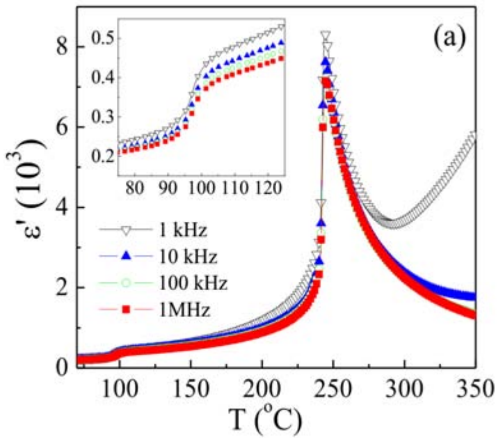

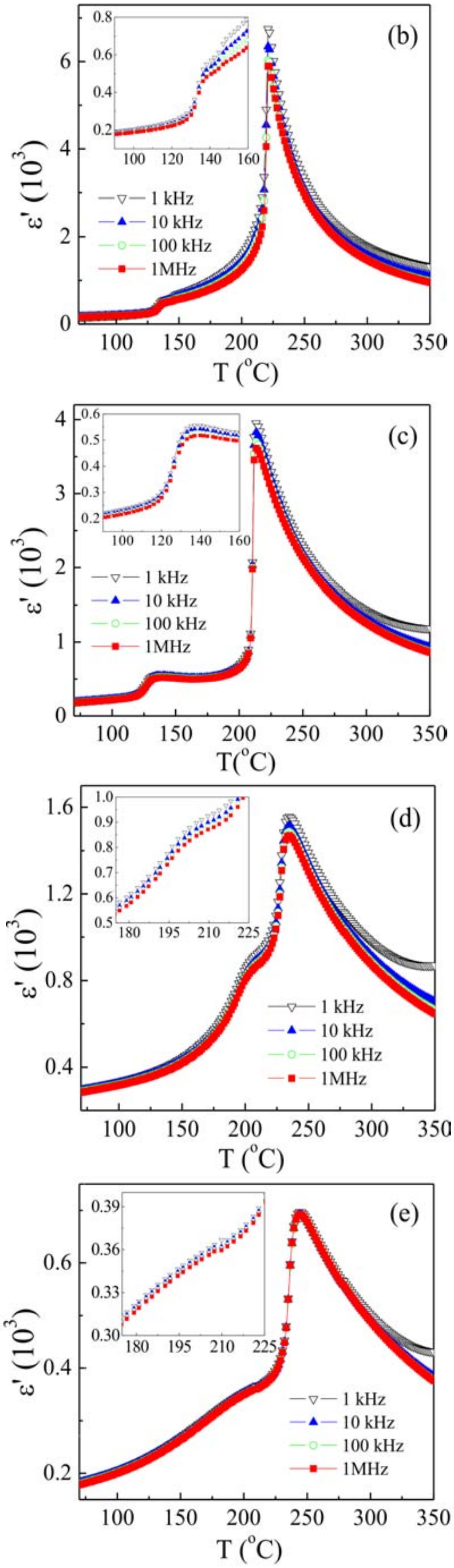

Figure 2. Temperature dependence of the real dielectric permittivity (ϵ'), at several frequencies, for (a) PLZT 0/95/5, (b) PLZT 1/95/5, (c) PLZT 2/95/5, (d) PLZT 3/95/5 and (e) PLZT 4/95/5.

Figure 3 shows the temperature dependence of the imaginary part of the dielectric permittivity (ϵ'') at several frequencies, for the studied compositions. The temperature corresponding to the maximum imaginary dielectric permittivity value ($T_{\epsilon'' max}$) was obtained around T_m values (Table 2) and no frequency dependence was observed. The observed dielectric behavior considering both temperature and frequency dependences (Figures 2 and 3) is typical of materials showing normal behavior in the ferroelectric-paraelectric phase transition. High values of ϵ'' are also observed at the higher temperature range, especially in the low frequency range, which can be attributed to the conduction losses effects [2].

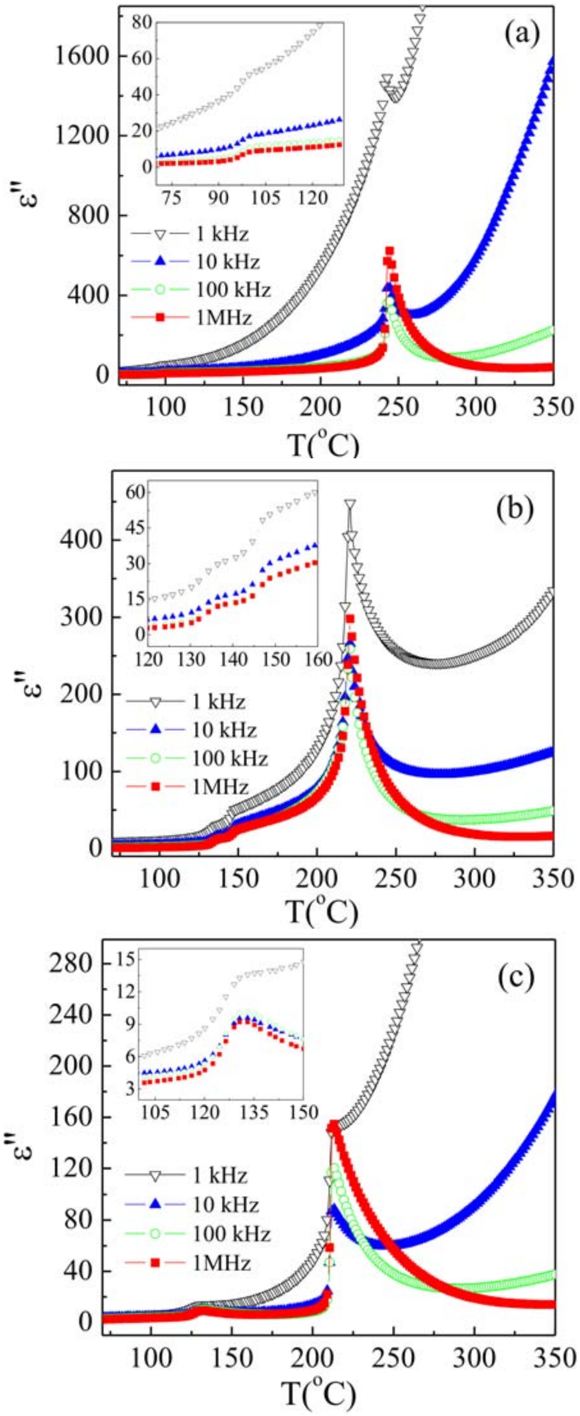

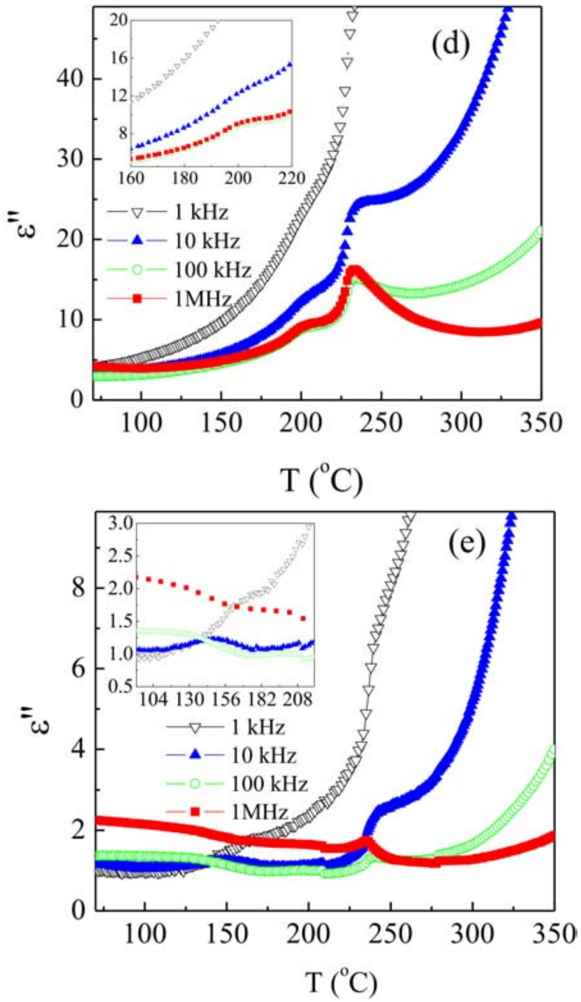

Figure 3. Temperature dependence of the imaginary dielectric permittivity (ϵ''), at several frequencies, for (a) PLZT 0/95/5, (b) PLZT 1/95/5, (c) PLZT 2/95/5, (d) PLZT 3/95/5 and (e) PLZT 4/95/5.

The hysteresis loops, at room temperature, are shown in Figure 4 for the studied compositions. The P-E dependence has revealed a double hysteresis loop for PLZT 0/95/5 (Figure 4**(a)**) and slim-like hysteresis loops for higher La^{3+} concentrations, suggesting an antiferroelectric character for all samples. The lanthanum concentration influences on the remanent polarization values (P_r). When the same electric field is applied on the studied samples, an increase in the La^{3+} content provides a tendency to decrease in the P_r values. This trend seems to be consistent with the observed tendency in the unit cell volume for the ferroelectric-rhombohedral phase. A contraction in its V suggests a decrease in the dipole moment and thereby in the polarization value.

The Pb−O−Zr/Ti bounding coupling in La^{3+}-doped samples plays an important role on these results [24]. Lead Pb^{2+} ions establish the long-range ferroelectric interactions in PZT systems due to the strong Pb−O−Zr/Ti bounding coupling [24]. This bounding defines the energy barrier between different polarization states (0, +P, -P), which are set by shift of Ti^{4+}/Zr^{4+} ions. The Pb^{2+} substitution by La^{3+} ions weakens the bounding, causing a decrease in the energy barrier [24]. The lower is the barrier energy, the dipoles will have greater ability of move back to their original configuration once the applied electric field is removed, and therefore, should expect lower remanent polarization in the studied samples when the lanthanum concentration increases.

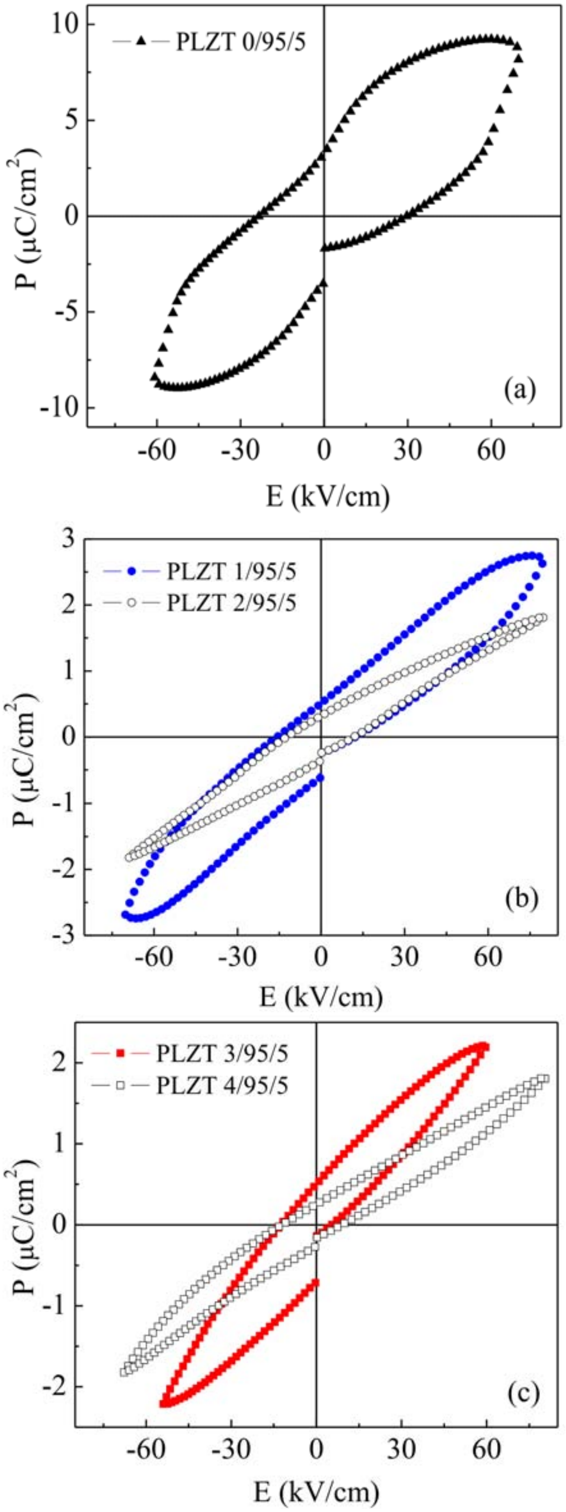

Figure 4. Hysteresis loops, at room temperature, for (a) PLZT 0/95/5, (b) PLZT 1/95/5 and PLZT 2/95/5, (c) PLZT 3/95 and PLZT 4/95/5.

In order to identify the phase transformations sequence, hysteresis measurements at several temperatures were performed for two compositions. Figure 5 shows the P-E behavior for PLZT 1/95/5 at several temperatures. From room temperature to until around $100^{o}C$, the double-like hysteresis loops have suggested the AFE phase stability. Above that, typical ferroelectric hysteresis loops have suggested the FE phase stability, which is confirmed at $140^{o}C$ by the squareness of the hysteresis loop. These results suggest that between $100-140^{o}C$ an AFE-FE phase transition could take place. Then, the first anomaly, which has been observed in the dielectric measurements around $133^{o}C$ could be associated to an AFE-FE phase transition for PLZT 1/95/5 system.

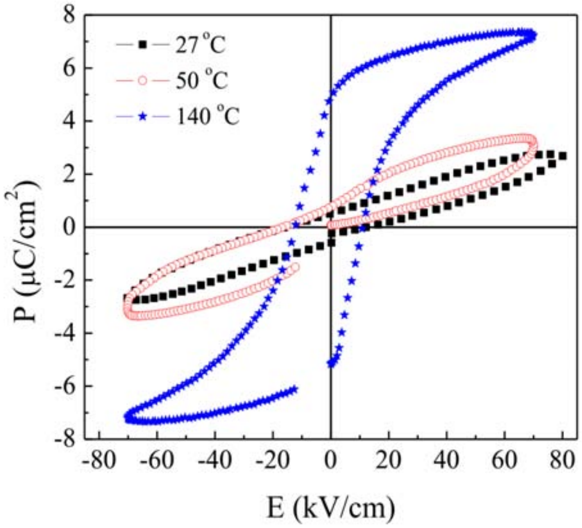

Figure 5. Hysteresis loops for PLZT 1/95/5 at several temperatures.

For PLZT 2/95/5, the results have shown a quite different behavior. Figure 6 shows the hysteresis loops at several temperatures. The results have suggested for all the studied temperature range, the AFE phase stability. Then, the first anomaly in Figure 2 cannot be associated to an AFE-FE phase transition. Previous reports on similar compositions by using transmission electron microscopy (TEM) have suggested an AFE-AFE phase transition, being the second one AFE phase an incommensurate state (AFEin) [12, 17–25].

It is known that ferroelectricity results from long-range Coulomb interactions between atomic dipole moments [13]. On the other hand, antiferroelectricity results from nearest neighbor interactions (sublattice coupling) between dipole moments. The short-range nature of the interactions can be affected for defects into structure. Consequently, the stability of the AFE state may be sensitive to small amounts of impurities. The lanthanum incorporation into PZT perovskite structure, with high Zr^{4+} concentration, provides a competition between the antiferroelectric and ferroelectric ordering, resulting in an AFEin-order around T_1 for 2 at % and higher lanthanum concentration [11, 12]. Thus, it can be considered that the lanthanum concentration favors a change in the phase transition sequence around T_1. Moreover, an increase of the T_1 values when the La^{3+} content increases could suggest a higher temperature range for the AFE phase stability.

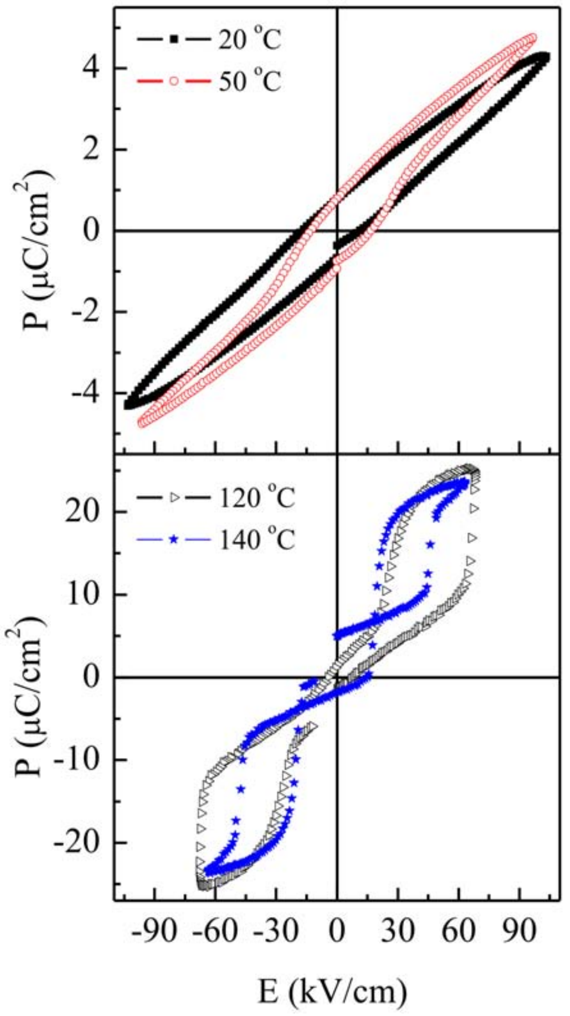

Figure 6. Hysteresis loops for PLZT 2/95/5 at various temperatures.

IV. CONCLUSIONS

Lanthanum modified lead zirconate titanate antiferroelectric ceramics have been studied to evaluate the effect of the lanthanum concentration on the antiferroelectric phase. Structural studies have revealed that both antiferroelectric-orthorhombic and ferroelectric-rhombohedral phases coexist at room temperature for the studied compositions. Dielectric measurements have showed two anomalies, which have been associated to different phase transitions in the studied temperature range. The P-E dependence, at room temperature, has suggested the antiferroelectric phase stability for all the studied samples. The analysis in a wide temperature range has suggested that the phase transition sequence depends on the lanthanum concentration.

V. ACKNOWLEDGMENTS

The authors would like to acknowledge the Third World Academy of Sciences (RG/PHYS/LA Nos. 99-050, 02-225 and 05-043), and the ICTP, Trieste-Italy, for financial support of Latin-American Network of Ferroelectric Materials (NET-43). Thanks to CNPq (300123/2015-9, 401072/2014-2) and FAPEMIG Brazilian agencies for financial support. Dr. Peláiz-Barranco would like to thank to Tongji University (Shanghai, China) and Xi'an Jiatong University (Xi'an, China) for financial support.

REFERENCES

[1] Hao, J. Adv. Dielect. 3, 1330001 (2013).
[2] A. Peláiz-Barranco, J.D.S. Guerra, O. García-Zaldívar, F. Calderón-Piñar, M.E. Mendoza, D.A. Hall , E.B. Araújo, Solid State Commun. 149, 1308 (2009).
[3] G. R. Love, J. Am. Ceram. Soc. 73, 323 (1990).
[4] W. J. Sarjenat, J. Zirnheld and F. W. Macdougall, IEEE Trans. Plasma Sci. 26, 1368 (1998).
[5] A. S. Mischenko, Q. Zhang, J. F. Scott, R. W. Whatmore and N. D. Mathur, Science 311, 1270 (2006).
[6] H. Zhang, X. Chen, F. Cao, G. Wang, X. Dong, Z. Hu and T. Du, J. Am. Ceram. Soc. 93, 4015 (2010).
[7] X. Chen, F. Cao, H. Zhang, G. Yu, G. Wang, X. Dong, Y. Gu, H. He and Y. Liu, J. Am. Ceram. Soc. 95, 1163 (2012).
[8] S. E. Young, J. Y. Zhang, W. Hong and X. Tan, J. Appl. Phys. 113, 054101 (2013).
[9] X. Hao, Y. Wang, L. Zhang, L. Zhang and S. An, Appl. Phys. Lett. 102, 163903 (2013).
[10] A. Peláiz-Barranco, Y. González-Abreu, Jinfei Wang and Tongqing Yang, Rev. Cub. Fis. 31, 98 (2014).
[11] X. Daí and D. Viehland, J. Appl. Phys. 76, 3701 (1994).
[12] D. Viehland, X. H. Dai, J. F. Li and Z. Xu, J. Appl. Phys. 84, 458 (1998).
[13] Y. Xu, Ferroelectric materials and their applications (Elsevier Science Publishers B. V., The Netherlands, 1991).
[14] A. Peláiz-Barranco, J. D. S. Guerra, O. García-Zaldívar, F. Calderón-Piñar, E. B. Araújo, D. A. Hall, M. E. Mendoza and J. A. Eiras, J. Mater. Sci. 43, 6087 (2008).
[15] J. Rodríguez-Carvajal, FULLPROF: A Program for Rietveld Refinement and Pattern Matching Analysis, Abstracts of the Satellite Meeting on Power Diffraction of the XV Congress International Union of Crystallography Toulouse, France (1990), p. 127.
[16] Z. Ujma, J. Haiiderek, H. Hassan, G. E. Kugel and M. Pawelczyk, J. Phys.: Condens. Matter 7, 895 (1995).
[17] D. Viehland, Jie-Fang Li, X. Dai, Z. Xu, J. Phys. Chem. Solids 57, 1545 (1996).
[18] J. Harideriek and Z. Ujma, J. Phys.: Condens. Matter 7, 1721 (1995).
[19] G. P. Espinosa, J. Chem. Phys. 37, 2344 (1962).
[20] R. D. Shannon, Acta Crystallogr. A 32, 751 (1976).
[21] D. R. Lide. Handbook of Chemistry and Physics (CRC Press, 2004).
[22] B. P. Das, R. N. P. Choudhary and P. K. Mahapatra, J. Mater. Sci.: Mater Electron 20, 534 (2009).
[23] L. B. Kong, J. Ma, R. F. Zhang and T. S. Zhang, J. Alloys Comp. 339, 167 (2002).
[24] I-Wei Chen, Ping Li, Ying Wang, J. Phys. Chem. Solids 57, 1525 (1996).
[25] X. Daí and D. Viehland, J. Appl. Phys. 65, 3287 (1994).

Rev. Cub. Fis. **33**, 18 (2016) ARTÍCULOS ORIGINALES

DEL MODELO MENTAL AL MODELO CONCEPTUAL EN LOS LABORATORIOS DE FÍSICA PARA INGENIERÍA

FROM THE MENTAL MODEL TO CONCEPTUAL MODEL IN THE PHYSICS LAB FOR ENGINEERS

M. Fernández†, F. Repilado y Z. Pérez

Facultad de Ciencias Naturales y Exactas, Universidad de Santiago de Cuba; maikelfdy@uo.edu.cu†
† autor para la correspondencia

Recibido 20/1/2016; Aceptado 20/4/2016

Se analizan las principales deficiencias que presentan los estudiantes en la ejecución de las prácticas de laboratorio de la Física I en las carreras de ingeniería de la Universidad de Oriente y las posibles causas que las originan, sobre la base de los modelos conceptuales que supuestamente dominan y se indican posibles vías para transformar los modelos mentales que poseen en modelos conceptuales de la ciencia. Se propone una metodología que emplea el "diálogo socrático" sustentada en la teoría de los modelos mentales de Johnson – Laird como herramienta heurística, con el objetivo de transformar dichos modelos y consolidar los conocimientos adquiridos. La metodología fue aplicada a la carrera de Ingeniería Eléctrica y se muestran los resultados.

The main difficulties that students of engineering careers in the Universidad de Oriente have in the practices of laboratory in Physics I, and their possible causes are analyzed. It is done by a methodology using of the "socratic dialogue", sustained in the Johnson-Laird's theory of mental model with the objective of transforming the mental models of the students in conceptual models. The methodology was applied to the career of Electric Engineer and the results are shown.

PACS: 01.30.lb Physics laboratory manuals undergraduate schools, 01.40.gb Teaching methods, 66.20.Cy Theory and modeling

En el proceso de enseñanza – aprendizaje de la Física en los Centros de Educación Superior un lugar preponderante lo ocupan las clases de laboratorio donde se manifiestan simultáneamente, diversos modos de actividades, tales como:

- Enfrentamiento a problemas cuyas soluciones requieren un arsenal de recursos experimentales.
- Movilización del pensamiento hacia lo intelectual y experimental.
- Búsqueda y aplicación de métodos experimentales para alcanzar soluciones factibles.
- Análisis científico exhaustivo.
- Comprobación de ciertas leyes y fenómenos.
- Desarrollo de habilidades intelectuales y experimentales de manera sistemática.

Aunque en las prácticas del laboratorio docente son reveladas y comprobadas las leyes y regularidades físicas más importantes, con frecuencia los estudiantes carecen - entre otras - de las nociones sobre:

- Enfrentamiento a problemas cuyas soluciones requieren un arsenal de recursos experimentales.
- ¿Por qué se emplea determinada instalación experimental?
- ¿Cuál es su finalidad?
- ¿Sobre qué bases se sustenta?
- ¿Qué criterios constructivos la sostienen?
- ¿Por qué ciertas magnitudes físicas son objeto de medición mientras que otras no?

El presente trabajo es parte de un estudio que se realiza con los estudiantes de la carrera de Ingeniería Eléctrica de la Universidad de Oriente, en Santiago de Cuba, que apunta a la determinación de su nivel de "interpretación y aplicación" de los contenidos objeto de aprendizaje de la Física a partir de:

- Los datos obtenidos directamente de las mediciones.
- Los resultados conseguidos después al procesarlos en cada una de las prácticas de laboratorio de Física I.
- Las informaciones que aparecen en la bibliografía.

En el estudio se resalta la necesidad de transformar - o al menos aproximar aún más - los modelos mentales con que inicialmente operan los estudiantes a los modelos conceptuales que establece la ciencia, constatándose que persisten grandes dificultades en la comprensión, tanto teórica como experimental, de los fenómenos o procesos físicos abordados en las prácticas. Se considera que una de las influencias más sobresalientes en la persistencia de dichas insuficiencias radica en que los docentes no dedican el tiempo y atención requeridos a:

- “Proceso de modelización” de fenómenos y procesos físicos.
- Conocimiento de “lo que el estudiante sabe”, “cómo lo sabe” y “cómo percibe y explica el mundo que le rodea”, es decir, cuáles son sus modelos mentales y preconceptos.
- Vínculo: modelo conceptual → instalaciones experimentales

Ese último aspecto coincide en lo esencial con lo expresado por Moreira y Greca [1].

Resulta interesante la pregunta “¿Es posible enseñar a pensar?” [2]. Se puede afirmar que no se han agotado las respuestas a esa pregunta. Los autores de este artículo intentan contribuir a ese debate con un enfoque vinculante de varias facetas del proceso de formación del profesional de Ingeniería, a partir de la necesaria transformación de los modelos mentales de los estudiantes en conceptuales con ayuda del diálogo socrático en las prácticas de laboratorios de la Física I.

Son muchos los criterios, enfoques y aproximaciones que se han vertido sobre la formación del pensamiento experimental y la transformación en los estudiantes de los modelos mentales en los modelos conceptuales de la ciencia. Sin embargo, los autores asumen la opinión de Johnson - Laird [3] cuando considera que, de una u otra forma, todas las personas operan cognitivamente con modelos mentales y, además, que eso es simplemente un proceso natural en el ser humano.

Uno de los procesos primarios y esenciales en la formación del pensamiento, en el caso de los estudiantes de ingeniería, descansa en su “ordenamiento y sistematización” a partir de disímiles situaciones físicas – ¡que de ningún modo constituyen “recetas” preconcebidas o elaboradas previamente! – para facilitar la ejecución y concreción del mismo.

El proceso de transformación: desde los modelos mentales hacia los modelos conceptuales de la ciencia, debe ser algo paulatino e intencionado a la vez que consolida métodos de enfrentamiento y solución de situaciones y problemas. En ese proceso se crean y moldean “herramientas” que posibilitan enfrentar y resolver nuevas situaciones, pasando, en una especie de “salto epistemológico progresivo”, de una síntesis sustancial a otra. En esencia: Lo trascendente, es enseñar a pensar de manera eficiente. “Los pensamientos con el consejo se ordenan.” [4]. Así, los pensamientos ofrecerían pistas sobre los posibles modelos mentales de los estudiantes que permitirían al profesor contrastarlos y corregirlos acercándolos, con una sabia conducción, a los modelos conceptuales. Por eso, el aprendizaje tiene un carácter natural y el docente debe conducir y optimizar el mismo, es decir, transformarse en un agente desarrollador.

En resumen, en el presente trabajo se elabora una metodología a partir del conocimiento de las características generales de sus modelos mentales [5], para la dinámica del proceso de enseñanza - aprendizaje que permita que los estudiantes comprendan, en toda su riqueza, y apliquen, a disímiles situaciones, las leyes fundamentales de la física.

I REFERENTES TEÓRICOS DE LA METODOLOGÍA

La metodología que se propone tiene su basamento en los modelos mentales, conceptuales y la modelización en sus diversos usos en la docencia según [3,5,6], además, se asumen los tres tipos de representaciones mentales propuestos por Johnson – Laird:

1. Proposicionales: vinculadas con la memorización de conceptos y leyes.
2. Los modelos mentales como análogos estructurales de la realidad.
3. Las imágenes.

Una de las exigencias que impone la concepción de Johnson – Laird y Moreira [1], además de afianzarse en que se opera cognitivamente con modelos mentales es que estos sean funcionales y, según Moreira [1] se entenderá por funcionalidad aquello que le permite al sujeto describir, explicar, predecir y controlar conductas de los fenómenos o características presentes en el objeto de estudio, aunque éstas no sean correctas científicamente. Por otra parte, entre las características básicas de los modelos mentales a superar se encuentran, según Norman [5]:

- Son incompletos.
- La habilidad de las personas para ejecutar sus modelos es muy limitada.
- Son inestables.
- No tienen fronteras bien definidas.
- No son “científicos”, más bien “supersticiosos”.
- Son parsimoniosos.

Con respecto a los modelos conceptuales, para Moreira “los modelos conceptuales son representaciones precisas, completas y consistentes con el conocimiento científicamente compartido” [6].

La modelización es otra cuestión importantísima y será entendida como el proceso de construcción y uso de los modelos conceptuales tomando como punto de partida los modelos mentales de los estudiantes. Esta es, precisamente, la habilidad esencial a desarrollar en el colectivo de estudiantes pues, según Gangoso y García [7–9], incluye en sí misma al resto de las otras habilidades. En ese sentido, se sostiene la tesis que los modelos mentales de los estudiantes pueden ser investigados por los “pasos o etapas” que supone su transformación en modelos conceptuales.

Los autores comparten las opiniones de Moreira [1] de que el proceso de modelización debería ser guiado por el profesor con ayuda de los modelos conceptuales para ordenar y evaluar sus modelos mentales (maximizando su recursividad), haciéndolos cada vez más semejantes a ellos.

Por otro lado, el reajuste de los modelos mentales en el proceso de modelización que realizan los estudiantes procura, básicamente, el empleo del arsenal científico disponible para la explicación de situaciones y problemas físicos y no sólo la transposición eventual de las experiencias distorsionantes de cada persona.

En el proceso de modelización se profundizan en todos los detalles del objeto de estudio y se muestra que los modelos mentales - al ser incompletos – requieren, para superarlos, de un abordaje más próximo a los modelos conceptuales para optimizar el proceso de modelización. Otro criterio considerado fue el de Crespo [10] y Perales [11] sobre el carácter semi abiertos - de verificación – cíclicos – temporales en el desarrollo de las prácticas de laboratorio.

Por otro lado, y como herramienta complementaria para conseguir el objetivo, se emplea el diálogo socrático - ¡pero sujeto a la teoría de los modelos mentales! - con ello se espera superar la insuficiencia de no ser efectivo para todos los auditorios como expresa Julian [12], proporcionándole al profesor la habilidad de hacer uso con destreza de esta herramienta, como lo sugiere Hake [13] y ser certeros en la formulación de preguntas de forma más adecuada, que facilite la conducción del proceso de modelización.

Sirva como ilustración para apreciar el valor del diálogo socrático en los laboratorios, una pequeña interacción profesor - estudiante sobre el tema de cinemática.

Profesor: ¿Siempre que la velocidad sea cero, la aceleración también lo será? *Estudiante:* ¡sí. . . ! ¡sí. . . ! *Profesor:* ¿Puede poner un ejemplo? *Estudiante:* ¡Bueno, uuuuhhh. . . uuuh...! *Profesor:* Un ejemplo puede ser cuando lanzamos un objeto en línea recta hacia arriba. Se conoce que al llegar al punto más alto su velocidad es cero, pero si su aceleración fuera cero, según la segunda ley de Newton, las fuerzas externas que actúan sobre él estarían compensadas y, por la primera ley de Newton, los cuerpos lanzados hacia arriba deberían quedarse en reposo y no caer, sino que levitarían, lo que es una flagrante contradicción con la realidad. Aquí el planteamiento del profesor es un ejemplo de modelización a partir de la reducción al absurdo.

Como se aprecia, este enfoque difiere esencialmente del pequeño diálogo que propone Lara [2], pues el propósito esencial de la enseñanza de la física es la física del fenómeno y no tanto las unidades de las magnitudes (aunque ellas juegan un importante papel), pues algunas magnitudes físicas se expresan en iguales unidades, pero responden a conceptos diferentes.

En este ejemplo – y en correspondencia con la teoría de los modelos mentales –las ecuaciones y algoritmos matemáticos, o sea, las representaciones proposicionales, ocupan un plano secundario, no así los “análogos estructurales de la realidad”, (modelos mentales), los cuales reflejan o transponen la esencia de esa realidad reajustándola a condiciones cambiantes.

De la estructura del diálogo sostenido se aprecian la lógica de la pregunta y la contra pregunta para conformar el conjunto de preguntas a realizar e incidir en la concepción futura de las clases y sus objetivos, dadas eventuales condiciones. Ellas deben cumplir con las peculiaridades generales de los modelos mentales, pero sobre todo, hacerlo en cualquier circunstancia.

Finalmente, y como elemento esencial para elevar la eficiencia organizativa y cognitiva del proceso, se consideró prudente dividir la clase de laboratorio en tres momentos básicos:

- Diagnóstico: una entrevista profesor – estudiantes sobre un problema revelado previamente y cuya posible respuesta es discutida y construida con ellos.
- Desarrollo: En la instalación y con instrumentos de medición y en principio, conociendo lo que hace, se realiza un conjunto de mediciones y ejercicios orientados por el profesor.
- Defensa de resultados o evaluación del informe: los estudiantes presentan un informe crítico sobre la práctica realizada siendo discutido en una sección posterior de laboratorio y cuya nota final será el promedio de las tres etapas.

Todas estas etapas “atacan” el carácter parsimonioso de los modelos mentales.

Por eso, la metodología que se propone se basa en el “cuestionamiento” de la funcionalidad de los modelos mentales en cada una de las etapas descritas para acercarlos y transformarlos en modelos conceptuales en el proceso docente.

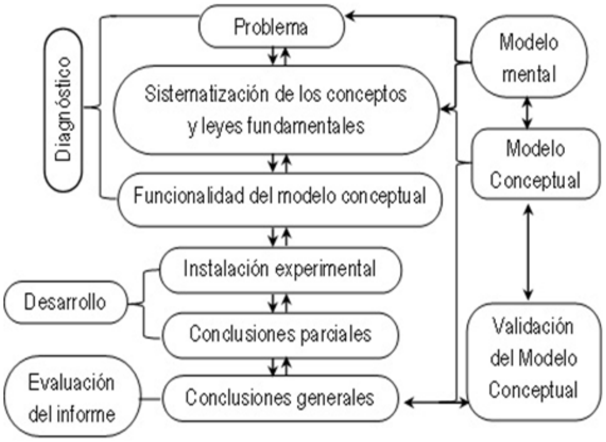

Figura 1. Estructura metodológica para la dinámica de las clases de laboratorio.

En cualquier caso, es recomendable “llevar” una especie de bitácora para las respuestas más interesantes de los estudiantes, y así posteriormente transformarlas en fuente de nuevos recursos didácticos.

II METODOLOGÍA PARA EL PROCESO DE MODELIZACIÓN (MDPPM) EN LAS CLASES DE LABORATORIO DE FÍSICA I

Como se ha indicado, las prácticas de laboratorio se realizan en tres etapas: a) Diagnóstico, b) Desarrollo y c) Defensa y evaluación del informe. La implementación de la metodología que se propone transita por las tres etapas antes referidas y su integración (Figura 1).

Aunque explícitamente no aparezcan, el método socrático y el método experimental en la figura, a lo largo de toda la clase de laboratorio la interacción profesor - estudiantes se hará con el uso de ambos como fuentes imprescindibles de activación mental sujeto a la teoría de los modelos mentales.

III ETAPA DE DIAGNÓSTICO

Consta de dos momentos:

A Momento de diagnóstico.

B Momento de corrección y ajuste de los modelos mentales con respecto al modelo conceptual.

El primero busca hurgar y contrastar los modelos mentales con los modelos conceptuales. El segundo busca también contrastar, corregir y ajustar los modelos mentales originales de los estudiantes para que se asemejen cada vez más a los conceptuales

¿Cuál es el objetivo expreso de la primera etapa?

Al menos se presupone pasar por las siguientes subetapas:

- Diagnosticar.
- Sistematizar conceptos y leyes fundamentales.
- Revelar la funcionalidad del modelo conceptual.
- Realizar un resumen - síntesis.

Diagnosticar las principales insuficiencias y deficiencias que presentan los estudiantes cuando intentan resolver el problema o situación experimental de la práctica correspondiente. Tal objetivo implica conocer:

- La forma en que piensan.
- El manejo de los modelos mentales y conceptuales.
- El nivel de argumentación, abstracción y generalización que poseen.

Sobre esas bases y aplicando, entre otros, el método socrático, es posible corregirlos.

¿Cuál es el punto de partida?: *El problema experimental*.

El problema de la práctica, concreto y asociado con hechos cotidianos (analogías de la realidad), se escoge para que el estudiante pueda resolverlos sin tantos detalles de las instalaciones, minimizando así el uso de las proposiciones en los intercambios profesor - estudiante. La construcción de un problema es, de hecho, *un proceso de modelización*.

Sistematización de los conceptos y leyes fundamentales:

El diálogo socrático estará presente en la activación o reactivación de cualquier concepto o situación física, lo que supone identificar los temas a debate y verificar el dominio de los conocimientos mínimos de los estudiantes, en esencia: se debe alcanzar una especie de resumen - síntesis sobre los modelos conceptuales a emplear en la práctica de laboratorio. Éste, posiblemente, es uno de los méritos más importantes del empleo del diálogo socrático en el laboratorio.

Funcionalidad del modelo conceptual:

Se enfatizará en las posibles aplicaciones del modelo conceptual en la vida cotidiana y en la práctica de su profesión (funcionalidad), a partir de ejemplos concretos, similar al proceso de resolución de problemas. Los modelos mentales no tienen fronteras bien definidas en tanto un mismo modelo sirve para situaciones diversas.

Resumen de la etapa de diagnóstico:

Al finalizar la etapa de diagnóstico, el continuo uso de los modelos conceptuales asegura, como tipo de representación predominante, modelos mentales más próximos a los modelos conceptuales.

IV ETAPA DE DESARROLLO

Esta parte consta de los siguientes elementos y subetapas:

- Modelo conceptual → diseño experimental
- Instalación experimental
- Ejercicios a resolver
- Obtención de la data experimental
- Valoración de los resultados

Objetivo: desarrollar la dinámica del proceso de enseñanza-aprendizaje de las clases de laboratorio a partir de la correspondencia entre los modelos mentales, conceptuales y la instalación experimental.

En realidad, el modelo conceptual obtenido anteriormente permite, sin tantas dificultades, derivar un diseño de experimento donde se precisen las magnitudes a medir, las constantes, y cualquier otra magnitud, y de ahí, el tipo de instalación experimental necesaria para llevarlo a cabo.

Instalación experimental: Se discute el funcionamiento de la instalación experimental en base a los modelos conceptuales y haciendo uso de su funcionalidad, se analiza el objeto real de estudio.

Es tema de particular atención, la "ecuación de trabajo o materialización del modelo conceptual" [1] pues permite precisar: el posible método a emplear y del conjunto de magnitudes involucradas en el proceso, cuáles son: a) constantes, b) parámetros controlables, c) magnitudes medibles y d) las magnitudes que cargan con los mayores errores.

En esa situación, con el diálogo socrático se accedería "continua y suavemente" a esta subetapa, por los tipos de preguntas que proponen, por ejemplo: a) De las magnitudes involucradas en la ecuación de trabajo ¿cuáles serán medibles experimentalmente? b) ¿Cómo?, c) ¿De qué manera hacerlo?, entre otras.

¿Y ahora. . . . qué sigue?

Precisamente ahora comienza una de las etapas más trascendente en la ejecución de la práctica: el desarrollo conjunto de habilidades, tanto intelectuales como experimentales. La discusión del posible método a emplear, abre dos sendas epistemológicas necesarias:

1. La idea de la aplicación de cierto método "general", válido en correspondencia al tipo de problema a resolver
2. La idea del "ajuste y concreción del método "general" para precisar los ejercicios a resolver, las magnitudes a medir, la posible data a obtener y los rangos de valores esperados de las magnitudes a medir y sus posibles causas, o viceversa, siempre sobre la base de los modelos conceptuales.

Obviamente requieren especial atención:

- Identificar las variables que intervienen en el problema.
- Planificar los pasos según la guía que da cuenta de la realización del experimento, preparar tablas de recogida de datos, así como interpretar los resultados.
- Concebir variantes alternativas para medir las variables que intervienen y decidir los instrumentos más adecuados a utilizar (lo que implica, a su vez, conocer sus características más importantes, intervalos que puede medir, sensibilidad, manipulación entre otros elementos).
- Tener presente todas las precauciones o medidas de seguridad en lo que respecta al proceso de medición, así como las incertidumbres inherentes a este proceso.

Conclusiones parciales de la práctica: Sobre la base del modelo conceptual discutir cómo éste se refleja en la instalación experimental y significar cómo cada una de las mediciones que se realizaron en los diferentes ejercicios estaban dirigidas a la solución del problema experimental, o sea, indirectamente, a la comprobación del modelo conceptual.

Como recomendación o alternativa, el profesor pudiera proponer un posible resultado concebido con anterioridad (diseñar un ejemplo por prácticas) y pedirle a los estudiantes explicar cómo desarrollarían ellos las conclusiones de su informe en función de estos resultados.

Finalmente, el profesor con todos los criterios de los estudiantes y su experiencia docente, debe valorar las posibles conclusiones del resultado propuesto, dejando algunas preguntas como estudio independiente para el momento de la revisión del informe.

Resumen de la etapa de desarrollo: Se continúa cuestionando el proceder de los estudiantes ante disímiles situaciones físicas de manera que se supere la inestabilidad de sus modelos mentales y se fomente aún más su transformación en modelos conceptuales.

V ETAPA DE REVISIÓN DEL INFORME

Objetivo: conocer si los estudiantes lograron apropiarse del conocimiento de los modelos conceptuales y permitirle al docente, a partir de sus respuestas, hacer un análisis recursivo de la metodología propuesta en aras de mejorar de forma empírica (como ha sido en este caso) y ajustarla a su propia experiencia personal, y analizar si los resultados obtenidos concuerdan con las predicciones del modelo conceptual.

Conclusiones generales: Esta etapa corresponde a un momento posterior de la realización del laboratorio y, por ende, el estudiante ha tenido tiempo para preparar el informe y pensar en las preguntas que el profesor pudo dejarle. El profesor por su parte, empleando el diálogo socrático, podrá retomar todos los conceptos y definiciones y conocer como los usó el estudiante en el proceso de modelización.

VI RESULTADOS DE LA APLICACIÓN DE LA (MDPPM)

En la aplicación de la metodología para las prácticas de laboratorio de Física General (cada encuentro de laboratorio tiene una duración de tres horas lectivas), se realizó un análisis tanto cualitativo como cuantitativo de los datos obtenidos de su aplicación.

En cada etapa de la metodología se realiza, esencialmente, de acuerdo con una rúbrica para evaluar las habilidades del razonamiento de los estudiantes. Ella pondera la medida en que los estudiantes están razonando bien a través de los contenidos del curso. La fuente principal fue obtenida del sitio web, *The Critical Thinking Community* dedicada a la investigación y difusión de todo tipo de información relacionada con la enseñanza, (*http://www.criticalthinking.org/*).

El criterio de evaluación fue ajustado a una escala del 2 al 5 para un total de cuatro niveles (ver Anexo):

Sobresaliente (5pt): hábil, se distingue por excelencia en claridad, exactitud, precisión, relevancia, profundidad, amplitud, lógica e imparcialidad.

Satisfactorio (4pt): competente, efectivo, preciso y claro, pero le falta la profundidad, exactitud y la perspicacia del sobresaliente.

Regular (3pt): inconsistente e inefectivo; muestra falta de competencias consistentes: con frecuencia es poco claro, impreciso, inexacto y superficial.

No satisfactorio (2pt): incompetente, se distingue por imprecisión, falta de claridad, superficialidad, poco lógico, inexactitud y parcialidad.

Este criterio se aplica de la misma manera en cada etapa de la metodología, considerando:

- en la etapa de diagnóstico qué tareas o problemas pueden significar.
- en la etapa de desarrollo el uso de las instalaciones experimentales y los instrumentos de medición para la realización de los ejercicios indicados.
- en la etapa de evaluación del informe el uso que hacen de los modelos conceptuales para interpretar sus propios resultados.

En todos los casos se fue coherente con el sistema de evaluación convencional de 2, 3, 4 y 5, evaluando la calidad de los resultados en orden ascendente conforme al criterio del profesor basados en la rúbrica propuesta anteriormente (ver Anexo). Las clases de laboratorio se comenzaron con una conferencia introductoria (no evaluativa), ejemplificando una práctica de laboratorio por el método de elaboración conjunta siguiendo la metodología propuesta, con la finalidad de, posteriormente, aplicarla y controlarla. Lo que se esperaba de la conferencia introductoria es trasmitirles a los estudiantes qué significa en la asignatura de física resolver un problema.

En este curso los estudiantes tuvieron contacto por primera vez con la asignatura, y por ende, con la metodología propuesta. Al momento de iniciarse las prácticas del laboratorio solo habían recibido dos conferencias y una clase práctica (de ejercitación) del contenido. No se contaba con una referencia anterior de su desenvolvimiento por grupos. A continuación, mostramos los promedios de los trabajos de controles (TC) a lo largo de todo el curso y el promedio del curso hasta el tercer trabajo de control (PG) por grupos (enumerados con números romanos) en la tabla 1.

Tabla 1. Promedio de los tres trabajos de controles y promedios del semestre por grupos.

	TC1	TC2	TC3	PG
I	$3,54$	$3,08$	$2,26$	$2,96$
II	$3,46$	$2,96$	$2,86$	$3,09$
III	$3,54$	$3,40$	$2,26$	$3,07$

Los resultados en la tabla 1, muestran que los tres grupos están en igualdad de condiciones, incluso, muestran un comportamiento similar a lo largo de todo el semestre. La categoría docente de los profesores se enmarca entre Profesor Instructor (se entiende como el primer escalón en la escala docente con la única prerrogativa de desarrollar clases de ejercitación) y Profesor Asistente (es el segundo escalón en esta escala y ya puede, con autorización, dictar conferencias). Algunos de ellos ya eran Máster, además poseían gran experiencia docente en las clases de laboratorios.

Al final de un semestre (para un total de cinco prácticas de laboratorio), se dividió cada grupo en dos subgrupos de observación. El primer subgrupo (SG1) lo constituyen los estudiantes que recibieron seguimiento de la metodología al menos dos veces o más, a lo largo de todo el semestre y el segundo subgrupo (SG2) el resto de los estudiantes que no recibieron la metodología en más de un encuentro como máximo. Las características de los (SG1), por grupos y teniendo en cuenta el total de estudiantes por grupos (Total), cantidad (No) y porciento (%) de estudiantes que recibieron la metodología tres o más veces, al menos 2 veces, números de encuentros máximos por grupos (L) y el porciento que representan de los 5 totales, se muestran en la tabla 2.

Tabla 2. Las características de los (SG1), por grupos enumerados con números romanos.

	Total	Recibida 3 o más		Recibida 2 veces		L	
		No	%	No	%	No	%
I	19	8	42,1	11	57,9	4	80
II	21	7	33,3	14	66,7	3	60
III	20	9	45,0	11	55,0	3	60

Se debe resaltar de esta tabla que el grupo 1 fue al que mayor número de veces se le aplicó la metodología con 4 encuentros máximos, le sigue el grupo 3, con el mayor porciento de estudiantes con al menos tres encuentros y finalmente el grupo 2 con los peores índices.

La metodología fue aplicada solamente por un profesor a lo largo de todo el semestre, el resto de los profesores continuaron impartiendo las clases como tradicionalmente lo hacían, es decir sin apego a la teoría de los modelos mentales en el proceso de modelización a través del diálogo socrático como herramienta fundamental, ni fueron consecuente con los pasos y el orden propuestos por la (MDPPM).

Las evaluaciones fueron organizadas en el orden en que recibiendo la metodología (L) y no en el orden en que realizaron las prácticas según su planificación docente. Los resultados promedios por etapa de diagnóstico (P), desarrollo (D) y evaluación del informe (I), de los SG1, finalmente fueron promediados (Pr) y sistematizados por grupos en la tabla 3:

Tabla 3. Las evaluaciones de los (SG1), por grupos enumerados con números romanos.

	$L1$				$L2$			
	P	D	I	Pr	P	D	I	Pr
I	2,68	5,00	3,00	3,56	3,47	5,00	3,86	4,11
II	3,95	4,76	3,76	4,16	3,30	4,36	4,18	3,95
III	3,95	4,67	4,20	4,27	3,90	4,82	4,36	4,37
	$L3$				$L4$			
	P	D	I	Pr	P	D	I	Pr
I	4,75	5,00	4,00	4,80	4,80	5,00	4,80	4,85
II	4,13	5,00	3,00	4,04	-	-	-	-
III	4,63	5,00	4,25	4,63	-	-	-	-

De la tabla 3, se puede destacar que en la (D), los tres grupos, prácticamente siempre obtuvieron la máxima calificación, lo que se interpreta como que los estudiantes fueron capaces de crear modelos mentales que les permitieran entender cómo funcionan las instalaciones experimentales y el porqué del uso de los diferentes instrumentos de medición.

Para hacer más comprensible el análisis de los datos, se graficaron solo los resultados promedios por encuentro y se le ajustó una recta a cada grupo. Se asumió que según el signo de la pendiente - positiva o negativa - se manifestaba como un avance significativo o lo contrario del desarrollo del proceso de modelización como habilidad fundamental en los estudiantes.

El coeficiente de correlación (r), se interpreta, ora como un mejoramiento paulatino, ora como un retroceso en la formación de la habilidad de la modelización como habilidad fundamental. Para dejar poco margen a la dispersión, se asume $r \geq 0.70$, como criterio valorativo favorable [14,15].

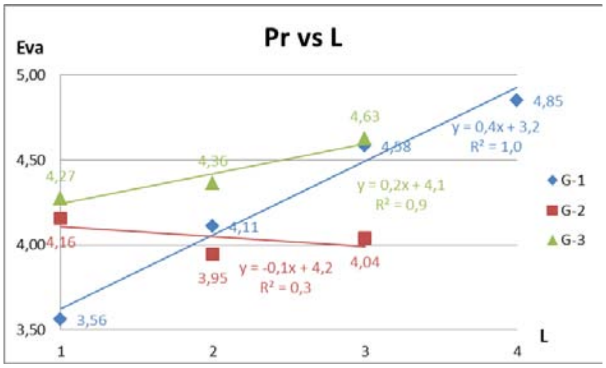

Figura 2. Evaluaciones promedios por encuentro en cada clase de laboratorio.

En la figura 2, se puede observar que los grupos 1 y 3, tienen pendientes positivas y $r \geq 0.9$. Estos grupos son los que representan las mejores muestras en cuanto al seguimiento de la metodología, por tener el mayor número de encuentros y los mayores porcientos de estudiantes que la recibieron en 3 o más veces. No así con el grupo 2, que tuvo el menor porcientos de estudiantes que recibieron la metodología. Los resultados en este grupo fueron con pendiente negativa y $r = 0.3$.

Tabla 4. Comparación según las evaluaciones obtenidas en los exámenes finales de los (SG1) con los (SG2), por grupos.

Grupo1			Grupo2			Grupo3		
SG1	SG2	Dif	SG1	SG2	Dif	SG1	SG2	Dif
3,50	3,08	0,42	4,00	3,08	0,92	3,44	3,00	0,44

Se estableció una tendencia comparativa según los resultados obtenidos en los exámenes finales, entre el método tradicional y la metodología propuesta, escogiendo de los (SG1), los estudiantes que recibieron la metodología tres o más veces y de los (SG2) (que no recibieron la metodología más de una vez), aquellos estudiantes que terminaron con 4 o 5 puntos en los laboratorios. Se escogió este criterio como tendencia comparativa por la similitud que existe entre una práctica de laboratorio y un examen final debido a que ambos, son orales. Los exámenes fueron hechos por el mismo tribunal y, al menos en la etapa de diagnóstico, se compararon las notas promedio de los exámenes finales por grupos, los cuales se muestran en la tabla 4.

Los resultados arrojaron diferencias apreciables (Dif) entre las notas promedios de los (SG1) que recibieron la metodología, la cual fue en todos los casos mayor que la de los (SG2) de cada grupo. La mayor diferencia la tuvo el grupo 2 con 0.92, luego le siguió en orden ascendente el grupo 3 con 0.44, que tuvo el mayor porciento de estudiantes que recibieron la metodología tres veces (45.0%) y el grupo 1 tuvo la menor diferencia 0.42, pero fue el único grupo cuyo 42.1% pudo recibir hasta 4 encuentros con la metodología. Esto es un resultado favorable, pues implica que el método tradicional no es el adecuado como se evidencia con los resultados del grupo 2, y que mientras más estudiantes puedan recibir la metodología y en la mayor cantidad de encuentros posibles, los resultados como tendencia, podrían considerarse cada vez mejores, en cuanto al desarrollo de la habilidad de modelización.

Esto indica que la propuesta de MDPPM, tuvo de forma general resultados satisfactorios y el análisis de los diferentes indicadores reveló que los estudiantes lograron resolver correcta e independientemente problemas con cierto grado de complejidad.

De manera general se obtuvieron evidencias de que los alumnos de mejor desempeño fueron los que aparentemente habían formado un modelo mental que se aproximaba al modelo conceptual. Los que trabajaron sólo con proposiciones (fórmulas o algoritmos matemáticos), limitándose a intentar aplicarlas mecánicamente, tuvieron el peor desempeño. Es decir, el aprendizaje sería tanto más significativo si el estudiante fuese capaz de construir modelos mentales y que estos además fuesen consistentes con los modelos conceptuales.

VII CONCLUSIONES

De los análisis efectuados se establecen las siguientes conclusiones:

- Persiste aún insuficiente correspondencia entre los modelos mentales, conceptuales y la instalación experimental en los estudiantes de las carreras de Ingeniería
- Cuando se modeliza, el emplear las características generales de los modelos mentales facilitaría la construcción de modelos de explicación más elaborados, expresados en lenguajes de nivel de abstracción cada vez mayor
- Se precisan rediseñar las tareas o ejercicios docentes de las guías de laboratorio para potenciar la concreción de esta metodología y, a su vez, un cambio esencial en la búsqueda y adquisición de los conocimientos y desarrollo de habilidades de modelización en la asignatura de Física para ingenieros
- Una de las mayores fortalezas del empleo la teoría de los modelos mentales es que permite concebir las clases para que estén más próximas a la realidad concreta del aula, pues posibilita valorar más certeramente los tipos de preguntas a seleccionar.

	5-Sobresaliente	4-Satisfactorio	3-Regular	2-No satisfactorio
Propósito	-Demuestra clara comprensión del propósito de la tarea	-Demuestra un entendimiento del propósito de la tarea	-Tiene poca claridad del propósito de la tarea	-No entiende el pro-pósito de la tarea
Pregunta clave o problema	-Define claramente el problema; identifica con precisión los aspectos centrales del problema -Percibe la profundidad y el alcance del problema -Demuestra objetividad e imparcialidad respecto al problema	-Define el problema; identifica los aspectos centrales, pero no explora la profundidad y alcance del problema -Demuestra objetividad e imparcialidad	-Define el problema, pero de manera superficial o reducida; puede pasar por alto algunos aspectos centrales. -Tiene problemas para mantener un enfoque objetivo e imparcial del problema	-No define clara-mente el problema; no reconoce los aspectos centrales. -No mantiene un enfoque objetivo e imparcial del problema
Punto de vista	-Identifica y evalúa puntos de vista relevantes y significativos. -Muestra empatía; es imparcial al examinar los puntos de vista relevantes	-Identifica y evalúa puntos de vista relevantes. -Es imparcial al examinar esos puntos de vista	-Puede identificar otros puntos de vista, pero le cuesta trabajo ser imparcial; puede enfocarse hacia pun-tos de vista irrelevantes o no significativos	-Ignora o evalúa superficialmente puntos de vista alternativos. -No puede separar sus propios intereses y sentimientos al evaluar otros puntos de vista
Información	-Acopia suficiente información, creíble y relevante: observaciones, afirmaciones, datos, preguntas, gráficas, temas, descripciones, etc. -Incluyen información que refuta tanto como que apoya la posición argumentada. -Distingue entre información e inferencias obtenidas de la información	-Acopia suficiente información creíble y relevante. -Incluye alguna información que refuta su posición. -Distingue entre in-formación e inferencias obtenidas de la información	-Acopia alguna información creíble pero no suficiente; parte de la información puede ser irrelevante. -Omite alguna información significativa, incluidos algunos contraargumentos. -Puede confundir algo de la información con inferencias	-Se apoya en información irrelevante, poco confiable e insuficiente. -No identifica o rápidamente descarta contraargumentos relevantes. -Confunde información e inferencias obtenidas de la información.
Conceptos	-Identifica y usa/explica con precisión conceptos clave relevantes	-Identifica, y usa/explica conceptos claves relevantes	-Identifica algunos (no todos) conceptos claves relevantes, pero su uso es superficial y en ocasiones imprecisos	-Interpreta mal conceptos claves y relevantes, o los ignora por completo
Asunciones (hipótesis)	-Identifica con precisión las asunciones (lo que se da por hecho). -Hace asunciones consistentes, razonables y válidas	-Identifica asunciones. -Hace asunciones válidas.	-Se equivoca al identificar asunciones o al explicarlas, o las asunciones identificadas son irrelevantes, no están enunciadas claramente, y/o son inválidas.	-Se equivoca al identificar asunciones. -Hace asunciones inválidas.
Interpretaciones, inferencias	-Sigue el camino que marcan la evidencia y el razonamiento para obtener conclusiones o soluciones pensadas, defendibles y lógicas. -Hace inferencias profundas más que superficiales. -Hace inferencias consistentes unas con otras.	-Sigue el camino que marcan la evidencia y el razonamiento para obtener conclusiones justificables y lógicas. -Hace inferencias válidas.	-Sigue algo de la evidencia para obtener inferencias las que pueden ser ilógicas, inconsistentes, poco claras, y/o superficiales	-Usa razonamientos simplistas, superficiales o irrelevantes y/o afirmaciones injustificadas. -Hace inferencias ilógicas o inconsistentes. -Muestra cerrazón de pensamiento o rechazo a razonar; a pesar de la evidencia, mantiene o defiende puntos de vista basados en el interés personal.
Implicaciones o consecuencias	-Identifica las implicaciones o consecuencias del razonamiento (ya sean positivas o negativas). -Distingue las implicaciones probables de las improbables.	-Identifica implicaciones o consecuencias significativas y distingue las implicaciones probables de las improbables (en menor grado de profundidad).	-Tiene problemas para identificar implicaciones o consecuencias significativas; identifica implicaciones improbables.	-Ignora implicaciones y consecuencias significativas del razonamiento.

REFERENCIAS

[1] Marco Antonio, M., Greca, I.M., and Rodríguez Palmero, M.L., Modelos mentales y modelos conceptuales en la enseñanza & aprendizaje de las ciencias Revista Brasileira de Pesquisa em Educação em Ciências, Porto Alegre 2, 3 p. 23 (2002).

[2] Lara-Barragán Gómez, A. and Cerpa Cortés, G., Enseñanza de la Física y desarrollo del Pensamiento Crítico Latin American Journal of Physics Education 8, 1 p. 8 (2014).

[3] Johnson-Laird, P., *Mental models*, (Harvard University Press., Cambridge, 1983).

[4] Santa Biblia, R.-V., Revisión de 1960. Proverbios 20:18, Sociedades Bíblicas Unidas. (2000).

[5] Norman, D.A., Some observations on mental models. En Gentner y Stevens, A.L. (Eds.). Mental models. Hillsdale, NJ : Lawrence Erlbaum Associates. 6-14 (1983).

[6] Greca, I.M. and Moreira, M.A., Modelos mentales, modelos conceptuales y modelización. Caderno Catarinense de Ensino de Física, Florianópolis. 15 (2), 107-120 (1998).

[7] Gangoso, Z., *et al.*, Resolución de problemas, comprensión, modelización y desempeño: un caso con estudiantes de ingeniería. Latin American Journal of Physics Education. 2, 3 p. 8 (2008).

[8] García García, J.J. and Rentería Rodríguez, E., La medición de las capacidades de modelización en las ciencias experimentales. Revista Virtual Universidad Católica del Norte 33, 1-28 (2011). (http://www.redalyc.org/articulo.oa?id=194218961009, http://revistavirtual.ucn.edu.co/).

[9] García García, J.J. and Rentería Rodríguez, E., La modelización de experimentos como estrategia didáctica para el desarrollo de la capaciada para resolver problemas. 11, 13 (2011).

[10] Crespo Madera, E.J. and Álvarez Vizoso, T., Clasificación de las prácticas de laboratorio de física. 6, 1-8 (2001)

[11] Perales Palacios, F.J., Los trabajos prácticos y la didáctica de las ciencias. Enseñanza de las Ciencias. 12, 1 p. 122-125 (1994).

[12] Glenn, M.J., Socratic dialogue—with how many? The Physics Teacher. 33, 6 p. 338-339 (1995) (http://scitation.aip.org/content/aapt/journal/tpt/33/6/10.1119/1.2344233).

[13] Hake, R.R., Socratic pedagogy in the introductory physics laboratory. The Physics Teacher. 30, 9 p. 546-552 (1992) (http://scitation.aip.org/content/aapt/journal/tpt/30/9/10.1119/1.2343637).

[14] Coletta, V.P. and Phillips, J.A., Interpreting FCI scores: Normalized gain, preinstruction scores, and scientific reasoning ability. American Journal of Physics. 73 p. 1172 (2005).

[15] Lasry, N., et al., The puzzling reliability of the Force Concept Inventory, in American Journal of Physics (2011): American Association of Physics Teachers. p. 909.

PROPIEDADES ÓPTICAS DEL DIÓXIDO DE TITANIO MESOPOROSO Y NANOCRISTALINO OBTENIDO CON LA TÉCNICA DE *DOCTOR BLADE*

OPTICAL PROPERTIES OF MESOPOROUS AND NANOCRYSTALLINE TITANIUM DIOXIDE OBTAINED USING *DOCTOR BLADE* TECHNIQUE

K. Padrón[a], B. González[b], F. Forcade[b], I. Zumeta[c] y E. Vigil[ab†]

a) Facultad de Física, Universidad de La Habana, Cuba; evigil@fisica.uh.cu
b) Instituto de Ciencia y Tecnología de Materiales (IMRE-UH), Universidad de La Habana, Cuba
c) Univ. Autónoma de México, UNAM.
† autor para la correspondencia

Recibido 8/4/2015; Aceptado 21/7/2015

Se analizan propiedades ópticas de películas del dióxido de titanio (TiO_2) nanocristalino y mesoporoso obtenido utilizando la técnica de “doctor blade”. Las películas de este material se utilizan tanto en distintos tipos de celdas solares sensibilizadas como en las recientes y novedosas celdas solares de perovskita. Se reportan y comparan los espectros de transmitancia, así como los de reflexión difusa de diferentes películas depositadas sobre vidrio óptico. A partir de los espectros de transmitancia se determina el índice de refracción utilizando el método de Swanepoel en el rango espectral $600-800$nm. Se argumenta la factibilidad de hallar la dependencia espectral de un coeficiente de absorción efectivo para el TiO_2 mesoporoso, el cual es reportado. Se discute la utilización de las constantes ópticas halladas para determinar el espesor de películas de TiO_2 similares a las estudiadas.

The optical properties of nanocrystalline and mesoporous titanium dioxide (TiO_2) layers, obtained using the “doctor blade” technique, are analyzed. These layers are used in different sensitized solar cell types, as well as, in the novel perovskite solar cells. Transmittance and diffused reflection spectra of different layers deposited on optical glass are reported and compared. Using Swanepoel method, the refractive index is determined in the 600-800 spectral range from transmittance spectra. Feasibility of obtaining the spectral dependence of an effective absorption coefficient for mesoporous TiO_2 is discussed and the spectra are reported. The use of the obtained optical constants to find the thickness of TiO_2 films, similar to those studied, is discussed.

PACS: optical properties of specific thin films, 78.66.-w; thin film thickness, 68.55.jd; absorption and reflection spectra of semiconductors, 78.40.Fy

I. IINTRODUCCIÓN

Es conocida la importancia creciente que tiene el empleo de las fuentes renovables de energía debido al agotamiento de las reservas de combustibles fósiles y a los daños medioambientales que produce el ritmo actual del consumo de estos. Las celdas solares para la obtención de energía renovable constituyen un elemento clave en los sistemas fotovoltaicos y son intensamente investigadas. Como caso especial de estas se encuentran las celdas solares fotoelectroquímicas. Estas celdas basan su principio de funcionamiento en la unión de un semiconductor con un electrolito. Las características del TiO_2 lo han hecho el semiconductor más ampliamente utilizado en el diseño de celdas fotoelectroquímicas tipo Gräetzel llamadas celdas solares sensibilizadas con colorante (DSSC, por sus siglas en inglés) [1].

Estas son ampliamente estudiadas en la actualidad, con variadas y múltiples aplicaciones potenciales. Una de las propiedades más ventajosas del TiO_2 es la gran resistencia que presenta a la corrosión o descomposición en presencia de reacciones químicas [2]. El TiO_2 nanocristalino resulta además un material muy barato y fácil de adquirir. La tecnología necesaria para preparar películas de TiO_2 para las celdas solares mencionadas es relativamente simple [3].

En el presente trabajo se estudian las propiedades ópticas del TiO_2 mesoporoso obtenido por la técnica de “doctor blade” a partir del polvo nanocristalino Degussa P25, extensamente utilizado en la fabricación de DSSC. Las películas así obtenidas son utilizadas en las DSSC [4], así como en las muy recientes celdas solares de perovskita [5].

Es conocido que las constantes ópticas de las películas de TiO_2 dependen de la técnica de crecimiento empleada debido a las inhomogeneidades en la densidad [6, 7], así como la porosidad, [8, 9]. No se han encontrado reportes de las constantes ópticas de películas mesoporosas de TiO2 obtenidas con la técnica de “doctor blade”.

En los siguientes epígrafes se reportan y comparan los espectros de transmitancia, así como los de reflexión difusa, de diferentes películas depositadas sobre vidrio óptico. A partir de los espectros de transmitancia se determina el índice de refracción utilizando el método de Swanepoel en el rango espectral $600-800$ nm. Se discute la conveniencia y factibilidad de hallar la dependencia espectral de un coeficiente de absorción efectivo, el cual es reportado. Se argumenta que estos resultados pueden servir para determinar el espesor de estas películas de TiO_2 mesoporoso y nanocristalino; el cual es hallado tradicionalmente utilizando perfilometría o microscopía electrónica de barrido de la sección transversal. Conocer el espesor de esta película es esencial para el análisis del comportamiento y funcionamiento de las estructuras y dispositivos que se fabriquen.

II. PARTE EXPERIMENTAL

II.1. *Obtención de las películas de TiO_2*

Todas las películas de TiO_2 nanoestructurado obtenidas en este trabajo fueron depositadas empleando como substratos vidrio óptico transparente (*soda lime glass*). La limpieza de los substratos se realizó primeramente con agua destilada en un baño de ultrasonido, seguido por acetona y/o etanol en sendos baños. Finalmente, se enjuagan con agua destilada.

Para preparar la suspensión coloidal acuosa se usó el polvo nanocristalino de TiO_2 Degussa P25. Se siguió el procedimiento descrito en la referencia [10] utilizando acetilacetona y Tritón X-100. La acetilacetona impide, o al menos dificulta, la agregación de las partículas de TiO_2 en la mezcla. El Tritón X-100 es una sustancia tensoactiva que favorece la mojadura del substrato por la suspensión coloidal de TiO_2.

La suspensión coloidal de color blanco se aplica utilizando la técnica de "doctor blade" (paleta del doctor). Esta se esparce sobre el substrato con una especie de rodillo o paleta, de ahí el nombre de la técnica.

Para aplicar la suspensión, los vidrios utilizados como substratos se fijan con cinta adhesiva a lo largo de dos bordes paralelos. En el borde superior se dejan caer algunas gotas de la suspensión para luego esparcirlas homogéneamente por la superficie del vidrio con ayuda de la "paleta". De esta forma, las cintas adhesivas delimitan el espesor de la película de TiO_2. Con este método se pueden obtener espesores mayores para las celdas solares sensibilizadas utilizando dos espesores de cinta adhesiva y/o repitiendo el proceso.

Las películas se dejan secar al aire antes de retirar las cintas adhesivas. Después se someten a un tratamiento térmico en aire a 450 ^{o}C durante una hora. Todas las muestras analizadas se obtuvieron siguiendo exactamente el mismo procedimiento. Las dimensiones de las muestras analizadas son aproximadamente de 2 $cm \times 1.5\ cm^2$.

II.2. *Medición de la transmitancia espectral*

Las mediciones de transmitancia, T, se realizaron en el intervalo de longitudes de onda de 400 a 800 nm utilizando un espectrómetro UV-visible Ultrospec, modelo 2100 Pro. Para obtener el espectro de la película de TiO_2 se utilizó como blanco el vidrio empleado como substrato.

II.3. *Medición de la transmitancia espectral*

La dependencia espectral de la reflexión difusa fue obtenida en un espectrofotómetro Cary-5E Varian, auxiliado por la esfera de integración correspondiente. El intervalo de longitudes de onda registrado fue de 300 a 800 nm.

II.4. *Medición de los espesores*

Las muestras estudiadas en este trabajo fueron medidas en varios puntos por perfilometría con un equipo Dektak 150. Esta información se utiliza no solo para caracterizar el espesor de las capas sino también su variación.

III. RESULTADOS Y DISCUSIÓN

III.1. *Espesor de las muestras medidas por perfilometría*

Las muestras fueron medidas a lo largo de tres direcciones paralelas para caracterizar las variaciones en el área de la muestra. El valor dado para cada posición en la Tabla 1 es el promedio dado por el equipo, del valor a lo largo de esa dirección. Se exceptúan las muestras G9 que fueron medidas a lo largo de dos direcciones en lugar de tres. Todos los valores aparecen con solo dos cifras significativas debido a la superficie rugosa de las muestras. Las desviaciones estándar que caracterizan la rugosidad de las muestras dadas por el perfilómetro inteligente Dektak 150 fueron menores que 0.05 μm.

Tabla 1. Espesores de las películas.

	Espesor (μm)			Valor medio (μm)
M2-2	3.6	3.5	3.6	3.6
M2-6	4.0	4.0	4.2	4.1
M3-2	3.2	3.0	3.3	3.2
M3-6	3.3	3.3	3.3	3.3
G9-1	3.1	2.9		3.0
G9-2	3.10	2.9		2.9
G9-3	3.1	3.0		3.1
G9-4	2.9	3.3		3.1

El valor medio de las ocho películas en la Tabla 1 es 3.30.4 μm. Si no se considera la película M2-6, el valor medio de las siete restantes en la Tabla 1 es 3.20.2 μm. Estos resultados indican la necesidad de medir el espesor de cada película obtenida utilizando "doctor blade" cuando el experimento realizado requiera dicho valor.

III.2. *Transmitancia óptica*

En la figura 1 se presenta la dependencia espectral del $\log(1/T)$ correspondiente a las diferentes muestras. Este disminuye más rápidamente en la región de fotones con mayor energía (menores longitudes de onda). Esta es la zona donde el TiO_2 absorbe, o sea, su borde de absorción; definido por el valor de su banda prohibida o gap, E_g (para la anatasa y rutilo, E_g = 3.2 eV (387 nm) y E_g = 3.0 eV (413 nm), respectivamente). Para las mayores longitudes de onda, donde el TiO_2 no absorbe, la disminución más lenta se puede explicar por la pérdida de la intensidad transmitida debida a la dispersión de la luz. Esto indica que la desagregación del polvo nanocristalino no fue óptima.

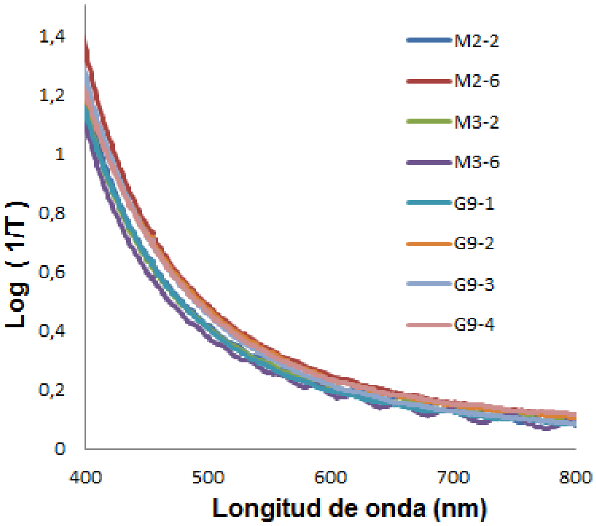

Figura 1. Dependencia espectral del $log(1/T)$.

Las variaciones de las curvas en la figura 1 muestran que, como es conocido, el fenómeno de absorción depende más fuertemente con la longitud de onda que el de dispersión.

III.3. *Dependencia espectral de la reflexión difusa*

En la figura 2 se observan los espectros de reflectividad difusa de las películas estudiadas.

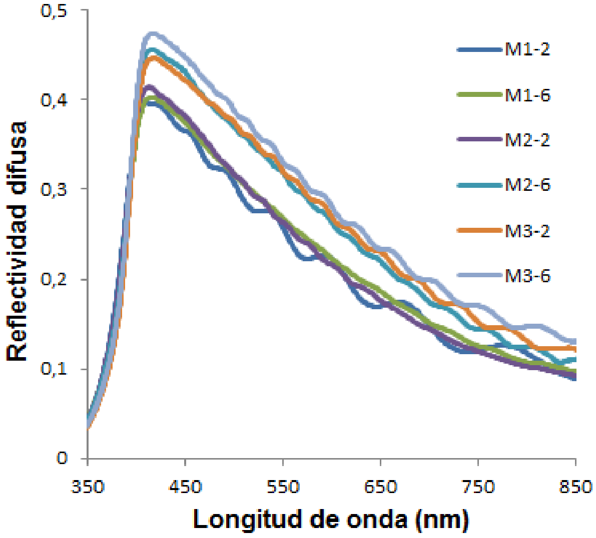

Figura 2. Dependencia espectral de la reflexión difusa.

En el rango de las menores longitudes de onda (mayores energías) la reflexión difusa disminuye con el aumento de la energía de los fotones. Es este el rango en que la variación de la transmitancia está determinada fundamentalmente por la absorción del TiO_2 como se vio en la figura 1.

En el rango de las mayores longitudes de onda, donde el TiO_2 no absorbe, la reflexión difusa está determinada por las reflexiones múltiples en los nanocristales y muestra la esperada tendencia decreciente con la longitud de onda. Se pueden observar máximos y mínimos de interferencia por ser la muestra una película delgada.

III.4. *Determinación del coeficiente de absorción efectivo*

La atenuación de una onda electromagnética en un medio es en general una función exponencial del coeficiente de absorción. Sin considerar la dispersión de la luz en la superficie y en el volumen, la intensidad de la onda a la distancia t de la superficie por donde incidió la radiación (espesor de la muestra cuando se mide transmitancia) está dada por la conocida expresión:

$$I(x) = I_0 e^{-\alpha t} \tag{1}$$

Donde I_0 es la intensidad de la luz incidente y α el coeficiente de absorción dependiente de la longitud de onda. De la expresión 1 se obtiene:

$$\alpha(\lambda) = \frac{1}{t}\left[\ln\left(\frac{I(\lambda)}{I_0(\lambda)}\right)\right] \tag{2}$$

Con la expresión 2, utilizando el espesor de las muestras en la Tabla 1 y el espectro de $\log(1/T)$, se determinó la dependencia espectral del coeficiente de absorción efectivo que se muestra en la figura 3. No es el coeficiente de absorción real porque está involucrado también el fenómeno de dispersión de la luz.

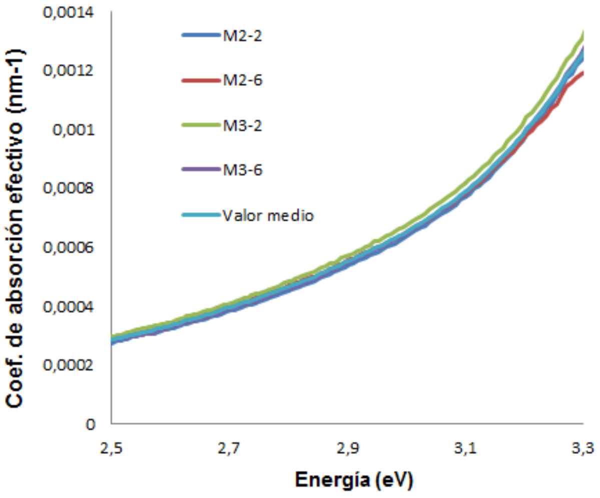

Figura 3. Coeficiente de absorción efectivo.

Se encontró coincidencia aceptable entre los coeficientes de absorción de cada muestra. Promediando los coeficientes de absorción para cada muestra, se determinó un coeficiente de absorción efectivo característico de las muestras de TiO_2 fabricadas según la técnica descrita en el rango espectral de 360 a 490 *nm*; donde predomina la absorción óptica (figura 3).

III.5. Obtención del índice de refracción de las muestras.

Los efectos de la interferencia se observan en materiales transparentes y también pueden ocurrir para zonas del espectro con poca absorción. La interferencia en películas delgadas, a partir de la cual se obtiene el patrón de máximos y mínimos de interferencia en el espectro de transmitancia de nuestras mediciones, es debida a la discontinuidad del índice de refracción en las dos fronteras: vidrio – película de TiO_2 y película de TiO_2 – aire. En la figura 1 se observan estos patrones en la mayoría de las muestras (M2-2, M3-3, G9-1, G9-4 y M3-6). Según el método de Swanepoel, el índice de refracción de la capa se puede obtener de estos máximos y mínimos en la zona donde no hay absorción o también, si esta es muy débil.

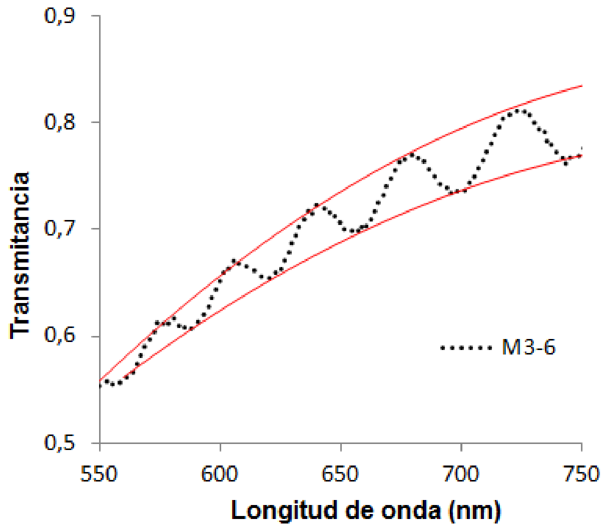

Figura 4. Espectro de transmitancia de la película M3-6 de TiO_2 ilustrando máximos y mínimos de interferencia. Se muestran las envolventes T_M y T_m de los máximos y mínimos de interferencia, respectivamente, [11].

La transmitancia T para el caso de la figura 4 es función de la longitud de onda; del índice de refracción del vidrio, s, del índice de refracción de la película porosa de TiO_2, n, y de su coeficiente de absorción, α [11].

Los extremos de las franjas de interferencia se pueden expresar mediante dos funciones T_M y T_m que son consideradas funciones continuas de λ y que corresponden a las envolventes de los máximos de interferencia (T_M) y de los mínimos (T_m) [11]. En la figura 4 se ilustran estas envolventes T_M y T_m. Swanepoel obtiene expresiones que permiten calcular el índice de refracción de las muestras en función de λ a partir de T_M y T_m [11]:

$$n = \sqrt{N + \sqrt{N^2 - s^2}}, \tag{3}$$

donde:

$$n = 2s\frac{T_M - T_m}{T_M T_m} + \frac{s^2 + 1}{1}. \tag{4}$$

Utilizando los espectros de transmitancia que presentan un patrón de interferencia en la figura 1 y considerando el valor del índice de refracción del vidrio soda lime, $s = 1.51$, se determinó el índice de refracción de las muestras en función de la longitud de onda. Se trabajó en el rango de 600 – 800nm utilizando la expresiones 3 y 4 donde las funciones $T_M(\lambda)$ y $T_m(\lambda)$ se obtuvieron a partir de un ajuste cuadrático de los valores de máximos y mínimos de interferencia respectivamente. La figura 5 muestra la dependencia, casi constante, del índice de refracción con la longitud de onda para cada muestra en el rango espectral de 600 – 800 nm. Las diferencias para las distintas muestras están dentro de las incertidumbres según el método seguido para hallar el índice de refracción. Se muestra además, la dependencia del valor medio hallada a partir de los valores de todas las muestras.

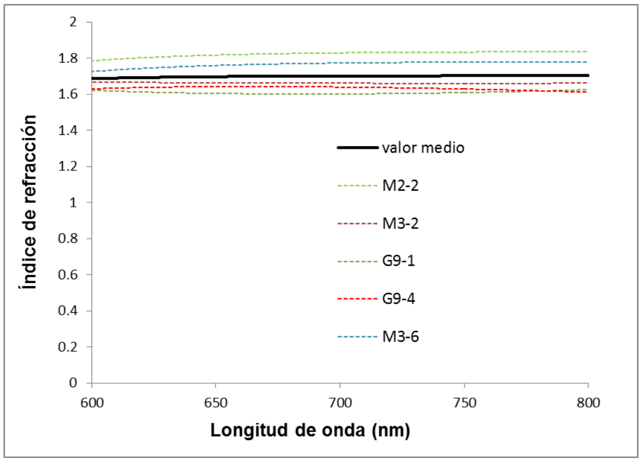

Figura 5. Índice de refracción en función de la longitud de onda de diferentes muestras de TiO_2 y su valor medio.

El valor medio resultante varía de 1.690.07 en 600 nm a 1.700.09 en 800 nm. El que este valor sea prácticamente constante en este rango espectral estrecho coincide con lo reportado por D. Bhattacharyya y colaboradores [7] y por El-Nahass y colaboradores [9]. El-Nahass y colaboradores [9] afirman que el valor constante del índice de refracción, $n = 1.66$, por ellos obtenido en el rango de 600-800 nm, es el menor valor reportado para TiO_2 mesoporoso.

III.6. Aplicaciones de las propiedades ópticas en el cálculo del espesor de las muestras.

El espesor de películas mesoporosas de TiO_2 obtenidas según la técnica de "doctor blade" descrita, se puede calcular utilizando el índice de refracción medio hallado. La variación muy lenta, prácticamente constante, de los valores de n dados en la figura 5 permite considerar constante el valor del índice de refracción para puntos extremos en el rango de 600 a 800 nm, $n = 1.70$. Con este es posible hallar el espesor de la película utilizando las expresiones:

$$nd = 2s\frac{m\lambda}{2} \tag{5}$$

$$nd = 2s\frac{(m+1)\lambda}{4} \tag{6}$$

Las cuales corresponden a las condiciones de máximos y mínimos de interferencia, respectivamente.

De estas expresiones, es posible hallar m dado que para los puntos extremos contiguos del mismo tipo la diferencia en m es de 1. Por ejemplo, en la expresión 5 el orden de interferencia m está dado por:

$$m = 2s\frac{\lambda_2}{\lambda_1 - \lambda_2} \tag{7}$$

donde λ_1 y λ_2 son longitudes de ondas de dos máximos adyacentes ($\lambda_1 > \lambda_2$). Con la técnica no invasiva propuesta para determinar el espesor de las capas mesoporosas obtenidas con la técnica de "doctor blade" que se emplea en el presente trabajo, con el valor $n = 1.7 \pm 0.1$ y una incertidumbre de 10 nm en la posición de los puntos extremos (incertidumbres ambas relativamente grandes), se obtendría un valor del espesor con una incertidumbre menor que el 8 %.

Cuando los espectros de transmitancia no muestran máximos y mínimos de interferencia en la zona donde el TiO_2 no absorbe la luz, esto puede deberse a la existencia de aglomerados de nanocristales que la dispersan. Por lo tanto, la aparición de los máximos y mínimos es deseable al indicar que fue efectiva la desagregación del polvo nanocristalino utilizado para hacer la suspensión coloidal. No obstante, si no aparecieran, es posible también estimar el espesor de la película utilizando el espectro del coeficiente de absorción efectivo $\alpha(\lambda)$ hallado (figura 3) y la siguiente expresión:

$$t = 2s\frac{1}{\alpha(\lambda)}\left[\ln\left(\frac{I_0}{I}\right)\right] \tag{8}$$

Esta se aplica en el borde de absorción, o sea, en el intervalo de 2.5 a 3.3 eV (380 a 500 nm), aproximadamente.

Se debe destacar que la medición del espectro de transmitancia, del cual es posible determinar el espesor de la película, es una medición no destructiva y simple, que puede ser introducida fácilmente como control de las películas fabricadas.

IV. CONCLUSIONES

Se han analizado las propiedades ópticas de las películas mesoporosas de TiO_2 que se obtienen utilizando el polvo Degussa P25 y la técnica de "doctor blade". A partir de los picos de interferencia en los espectros de transmitancia de diferentes muestras en el rango de 600 a 800 nm, utilizando el método de Swanapoel, se obtuvo el índice de refracción promedio de las películas. Este varía poco en este rango (1.69 ± 0.07 en 600 nm a 1.70 ± 0.09 en 800 nm). Se obtuvo un coeficiente de absorción espectral efectivo en el llamado borde de absorción que varía de 0.0003 nm^{-1} en 2.5 eV a 0.001 nm^{-1} en 3.3 eV. Tanto el índice de refracción como el coeficiente de absorción efectivo hallados pueden utilizarse para calcular los espesores de este tipo de muestra.

REFERENCES

[1] J. K Lee, M. Yang, Progress in light harvesting and charge injection of dye-sensitized solar cells, Materials Science and Engineering B 176,1142 (2011).

[2] T. Bak, J. Nowotny,M. Rekas, C.C. Sorrell, Photo-electrochemical properties of the TiO_2-Pt systemin aqueous solutions, International Journal of Hydrogen Energy 27, 19 (2002).

[3] G. P. Smestad, Education and solar conversion: Demonstrating electron transfer, Sol. Energy Mater. Sol. Cells 55, 157 (1998)

[4] H. M. Upadhyaya, S. Senthilarasu, M. H. HsuyD. K. Kumar, Recent progress and the status of dye-sensitised solar cell (DSSC) technology with state-of-the-art conversion efficiencies, Sol. Energy Mater. Sol. Cells 119, 291 (2013).

[5] N. G. Park, Perovskite solar cells: an emerging photovoltaic technology, Materials Today. 18, 65 (2015).

[6] A.Kasikov, J.Aarik, H. Mandar, M. Moppel, M. Pars y T.Uustare, Refractive index gradients in TiO_2 thin films grown by atomic layer deposition, J. Phys. D: Appl. Phys. 39, 54 (2006).

[7] D. Bhattacharyya, N.K. Sahoo, S. Thakur y N.C. Das, Spectroscopic ellipsometry of TiO_2 layers prepared by ion-assisted electron-beam evaporation, Thin Solid Films 360, 96 (2000).

[8] P. Sudhagar, R. Sathyamoorthy y S. Chandramohan, Influence of porous morphology on optical dispersion properties of template free mesoporous titanium dioxide (TiO_2) films, Appl. Surf. Sc. 254, 1919 (2008).

[9] M. M. El-Nahass, M. H. Ali y A. El-Denglawey, "Structural and optical properties of nano-spin coated sol–gel porous TiO2 films", Trans. Nonferrous Metals. 22, 3003 (2012).

[10] G.P. Smestad y M. Gratzel, Demonstrating Electron Transfer and Nanotechnology: A Natural Dye-Sensitized Nanocrystalline Energy Converter, J. Chem. Educ. 75, 752 (1998).

[11] R.Swanepoel., "Determination of the thickness and optical constants of amorphous silico", J. Phys. E: Sci. Instrum. 16, 1214 (1983).

EIGHT-CENTERED OVAL QUASI-EQUIVALENT TO KEPLER'S ELLIPSE OF PLANETS' TRAJECTORY

ÓVALO DE OCHO CENTROS QUASI-EQUIVALENTE A LA ELIPSE DE KEPLER DE LA TRAYECTORIA DE LOS PLANETAS

B. Herrera[a†] y A. Samper[b]

a) Departament d'Enginyeria Informàtica i Matemàtiques, Universitat Rovira i Virgili, Spain; blas.herrera@urv.net †
b) Unitat predepartamental d'Arquitectura, Universitat Rovira i Virgili, Spain.
† corresponding author

Recibido 9/5/2016; Aceptado 3/6/2016

This paper has academic nature, nevertheless it is an application from [9] that we think can be interesting to students and instructors of undergraduate level of physics. With low level of geometric and computational techniques the readers can reproduce the results of the present paper. The most important thing is that these results clearly show that it is not enough take numerical measures of the orbits of the bodies to decide which are the real equations and laws that govern them. We present an approximation of the Kepler's ellipse of the planets' trajectory by circular arcs, which is *quasi-equivalent*; that is: we present the approximation of the Kepler's ellipse $\mathcal{E}_b$ by the eight-centered oval $O_{\mathcal{E}_b}$ having the same center, axes, vertices, perimeter length and curvature at the vertices as $\mathcal{E}_b$, and also having practically negligible difference with respect to the surface area of $\mathcal{E}_b$, and also having barely distinguishable deformation error in relation to $\mathcal{E}_b$.

Este artículo, aunque tiene carácter académico en su naturaleza y presentación, consiste en una aplicación de las conclusiones geométricas de [9] la cual consideramos puede ser interesante para estudiantes y profesores en licenciaturas y grados de física. Con bajo nivel de geometría y técnicas computacionales, los lectores pueden reproducir los cálculos del presente trabajo. El aspecto más importante que se presenta aquí es que los resultados muestran que no es suficiente tomar medidas numéricas de las órbitas de cuerpos para poder determinar las ecuaciones y leyes reales que las gobiernan. Más concretamente, presentamos una aproximación, por arcos circulares, de la elipse de Kepler de las trayectorias de los planetas, la cual es *quasi-equivalente*. O sea, presentamos la aproximación de la elipse de Kepler $\mathcal{E}_b$ por el óvalo de ocho centros $O_{\mathcal{E}_b}$ el cual posee: mismo centro, ejes, vértices, perímetro, y curvatura en los vértices que $\mathcal{E}_b$, y además la diferencia entre las áreas de $\mathcal{E}_b$ y $O_{\mathcal{E}_b}$ es prácticamente nula y el error de deformación entre ambos es por añadidura prácticamente indistiguible.

PACS: 01.40.Fk Physics education, 01.50.H- Computers in education, 02.40.Dr Euclidean geometries, 95.10.Eg Orbit determination.

Approximating ellipses by circular arcs has been a classic subject of study by geometers. This has long been used for a wide range of applications, for instance in geometry, art, architecture. The reader can easily find a great deal of classical literature on these topics, in special for eight-centered ovals and four-centered ovals (also named *quadrarcs*). Moreover, because of its importance, this subject of study is continued in modern research papers as [1–7]. In astronomy this kind of approximation was classically considered, for example in [8].

This paper has academic nature, nevertheless it is an application from [9] that we think can be interesting to students and instructors of undergraduate level of physics. With low level of geometric and computational techniques the readers can reproduce the results of the present paper. The most important thing is that these results clearly show that it is not enough take numerical measures of the orbits of the bodies to decide which are the real equations and laws that govern them. Errors in measures, even if they are very small, can hide subtly the differences between different laws. Therefore in addition to taking measures, always depth studies of the physic which governs the motions of bodies are required. More specifically: here in this paper, we show the example of the planets' trajectory; because the geometric properties of two very different lines –ellipse and eight-centered oval– can be quasi-equivalent (having barely distinguishable differences), therefore computations of the orbits can hide the real physics laws. By contrast and as an added value, this paper also shows to students, and interested people, that they can change an ellipse by a quasi-equivalent eight-centered oval, if they consider that their negligible geometric differences are assumable in their concrete problems.

It is well known that Johannes Kepler, in the 17th century, made a search for a better description of planetary motion and, in *Astronomia Nova* [10] (1609), he provided arguments for elliptical trajectory of the planets around the Sun. However, in 1675, Giovanni Domenico Cassini did not agree with Kepler and he tried to prove that the planetary orbits were Cassini's ovals [11]. Recently, Sivardiere [12] explored this question and concluded that the difference between the Kepler's ellipse and Cassini's oval is as distinguishable as that between the Kepler's ellipse and the circular orbit; therefore, if we discard the circle in favour of the ellipse, then, we also should discard the oval with the same argument. In the work [13], Morgado and Soares analyzed this possibility and they show that it is difficult to decide in favour of one of the two curves. In fact, Morgado an Soares calculated the following:

Table 1. Calculations of Morgado and Soares [13].

	Mercury	Venus	Earth	Mars
ϵ	0.205600	0.006700	0.016700	0.093500
$E(\mathcal{O},\mathcal{E}_b)$	0.021364	0.000022	0.000139	0.004381
$E(\mathcal{E}_b,\mathcal{C}_b)$	0.021841	0.000022	0.000139	0.004400
$\frac{E(\mathcal{O},\mathcal{E}_b)}{b}$	0.021830	0.000022	0.000139	0.004400
$\frac{E(\mathcal{E}_b,\mathcal{C}_b)}{b}$	0.022318	0.000022	0.000139	0.004419
	Jupiter	Saturn	Uranus	Neptune
ϵ	0.048900	0.056500	0.045700	0.011300
$E(\mathcal{O},\mathcal{E}_b)$	0.001196	0.001597	0.001045	0.000064
$E(\mathcal{E}_b,\mathcal{C}_b)$	0.001198	0.001600	0.001046	0.000064
$\frac{E(\mathcal{O},\mathcal{E}_b)}{b}$	0.001198	0.001600	0.001046	0.000064
$\frac{E(\mathcal{E}_b,\mathcal{C}_b)}{b}$	0.001199	0.001603	0.001047	0.000064

Let $\mathcal{E}_b$ be the Kepler's ellipse of the orbit of a planet, let A, A', B, B', be the four vertices of the ellipse $\mathcal{E}_b$ and let a, b, ϵ, M be the mayor semi-axis, the minor semi-axis, the eccentricity and the center, respectively, of $\mathcal{E}_b$. We can assume that $a = 1$. Let $\mathcal{C}_b$ be the Cassini's oval with same center, foci points and mayor semi-axis of the ellipse $\mathcal{E}_b$. Let b_C the distance between M and the point $B_C \in \mathcal{C}_b$ such that $\frac{\pi}{2} = \measuredangle(A, M, B_C)$. Let $E(\mathcal{E}_b,\mathcal{C}_b) = b - b_C$, and let $E(\mathcal{O},\mathcal{E}_b) = 1 - b$ *i.e.* for small eccentricities $E(\mathcal{E}_b,\mathcal{C}_b)$ is the maximum difference between the positions given by the Kepler's ellipse and the Cassinian oval, and $E(\mathcal{O},\mathcal{E}_b)$ is the maximum difference between the positions given by the circular orbit $\mathcal{O}$ –of center M and radius 1– and the ellipse.

Morgado an Soares found, with $a = 1$, the results of Table1.

With Table 1, Morgado an Soares concluded in [13] that the maximum difference between the positions given by the circumference and the ellipse is of the same order of magnitude as that for the maximum difference between the positions given by the Cassinian oval and the ellipse. However, this difference is too small when compared with the values of the axis for all these curves to be observed with the naked eye, as was the case in Kepler's day. Kepler was probably unable to geometrically observe the difference between the ellipse and the circle unambiguously, and the difference between the ellipse and the Cassini's oval is also indistinguishable for the standards of his period. From the results of Morgado an Soares –in Table 1–, Kepler's ellipse and Cassini's oval are barely distinguishable when orbits with a small eccentricity are considered. This illustrates the ingenuity of Kepler in analyzing the observational data at his disposal. Finally, they call attention to Laplace's remark, found in his *Mécanique Céleste* [14], that only with Newton and his gravitation law will the ellipse be elected as the curve to better describe planetary motions, and all incompatibilities between theory and the real orbit are caused by the disturbance of another celestial body.

In this paper we look for an approximation of the trajectory of the planets, *i.e.* the Kepler's ellipse of the planets, by circular arcs which can qualify as being a *quasi-equivalent* approximation.

In order to attain a similarity of results in the planets' trajectory, an approximation which is equivalent to the Kepler' ellipse must have exactly coinciding geometric parameters. An eight-centered oval which is *equivalent* to an ellipse should have the same: center, axes, vertices, perimeter length, curvature at the vertices and surface area. Also, it should have little deformation in relation to the ellipse. Unfortunately, an eight-centered oval with all these exactly coinciding geometric parameters does not exist; it can not have all the same geometric parameters and also the same surface area.

There are different methods of approximating curves –least squares, minimax, orthogonal family of polynomials–. However, our approach is different; we look for the exact coincidence of single geometric parameters. Present exact analytical formulae for approximations Kepler's ellipse trajectories by eight-centered ovals with some geometric parameters which coincide exactly. Further, we want to show the precise numerical calculations of these approximations. And, as a conclusion, we want to present not the "equivalent" approximation because it does not exist, but the approximation of the Kepler' ellipse orbit $\mathcal{E}_b$ of the planets by an eight-centered oval $O_{\mathcal{E}_b}$ having the same center, axes, vertices, perimeter length, and curvature at the vertices as the ellipse, and also having practically negligible difference with respect to the surface area of $\mathcal{E}_b$ and showing barely distinguishable deformation in relation to $\mathcal{E}_b$. We call this 8-centered oval $O_{\mathcal{E}_b}$ "quasi-equivalent" to the Kepler's ellipse $\mathcal{E}_b$.

Of course, approximating ellipses by circular arcs with four-centered ovals (quadrarcs) also has been a classic subject of study by geometers, but in paper [9] it was proved that the approximation of the ellipses with four-centered ovals is geometrically and numerically poor –lack of geometric similarities and not negligible deformation error– to be qualified as *quasi-equivalent*. Therefore in this present paper we focus attention in the eight-centered ovals.

In short, this paper is inspired on the two previous works: [9] and [13]. The authors of [13] show that the deformation error between the Kepler's ellipse and a circumference, also between the Kepler's ellipse and a Cassini's oval, is small (Table 1). Here, we show that the deformation error between the Kepler's ellipse and an 8-centered oval is even smaller (Table 2). The authors of [9] obtained and showed, among other mathematical equations, the formulae that we have used here; but they used the equations only for geometric theoretical questions. Here, we show an application of the formulae; it is an application which has educational implications and we think can be interesting to students of physics.

An oval is a curve resembling a flattened circle but, unlike the ellipse, it doesn't have a specific mathematical definition. Therefore, right now we must lay down the definitions and notations of this paper.

I. DEFINITIONS AND NOTATIONS

Let A, A', B, B', be the four vertices of an ellipse $\mathcal{E}$, where A, A' are the focal vertices and B, B' are the transverse vertices. Without loss of generality, in the affine Euclidean plane $\mathbb{E}^2$, we can consider a Cartesian coordinate system $\mathcal{R}$ such that $A = (1,0)$, $A' = (-1,0)$, $B = (0,b)$, $B' = (0,-b)$, $1 > b > 0$. We discard the cases $b = 1$ ($\mathcal{E}$ is a circle) and $b = 0$ ($\mathcal{E}$ is a straight segment), because the problem trivializes. In order to highlight the parameter b, we call the ellipse $\mathcal{E}_b$. Therefore, the parameter b is the hypothesis parameter which determines the problem.

We consider the infinite quantity of ovals the vertices of which are also the points A, A', B, B'. Amongst them, we focus on the family of the *eight-centered ovals*, which we denote by $O_{8,b}$. And finally, we consider the family of the four-centered ovals (quadrarcs) $O_{4,b}$. The second family is a sub-family of the first one.

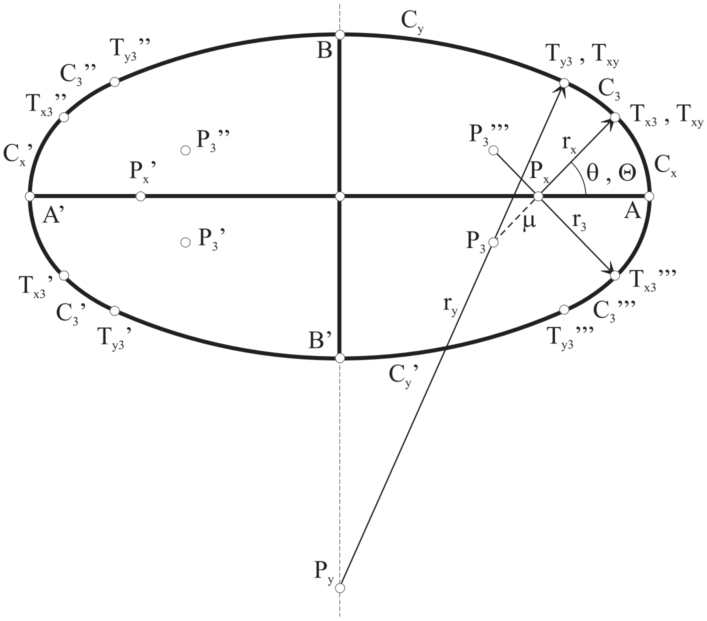

Figure 1. Elements of the 8-centered oval $O_{8,b}$ (quadrarc $O_{4,b}$ if $r_y = r_3$).

An oval $O_{8,b}$ is made up by 8 circle arcs which are tangent to each other such that, in the system $\mathcal{R}$, they have the following 8 centers (see Figure 1):

$$P_x = (x,0)\,, \quad 0 < x < 1, \quad \text{with} \quad 1 - x < b, \quad P'_x = (-x,0)\,,$$

$$P_y = (0,y)\,, \quad \text{with} \quad y \leq 0, \quad P'_y = (0,-y)\,,$$

$$P_3 = (x_3, y_3) \quad \text{with} \quad x_3 \geq 0, \; y_3 \leq 0,$$

$$P'_3 = (-x_3, y_3), \quad P''_3 = (-x_3, -y_3), \quad P'''_3 = (x_3, -y_3).$$

Moreover, the oval has radii r_x, r_y and r_3, where r_x is the radius of its arcs C_x, C'_x, with centers P_x, P'_x respectively; r_y is the radius of the arcs C_y, C'_y, with respective centers P_y, P'_y; and r_3 is the radius of the arcs C_3, C'_3, C''_3, and C'''_3 with respective centers P_3, P'_3, P''_3, and P'''_3. The curvatures of these arcs are inverse to their radii, $\frac{1}{r_x} = k_x$, $\frac{1}{r_y} = k_y$, $\frac{1}{r_3} = k_3$.

If $r_y = r_3$ then $P_y = P_3 = P'_3$ and $P'_y = P''_3 = P'''_3$. This special case of 8-centered oval $O_{8,b}$, noted as $O_{4,b}$, is called 4-centered oval. The segments AA', BB' are called major axis and minor axis of $O_{8,b}$, as well as at ellipse.

The oval $O_{8,b}$ has 8 contact points for its 8 arcs: point T_{x3} is the contact between C_x and C_3, point T_{y3} is the contact between C_y and C_3, points T'''_{x3}, T'''_{y3}, T''_{x3}, T''_{y3}, T'_{x3}, T'_{y3} are symmetrical to T_{x3}, T_{y3} with respect to the axes and center point and they are the contact between C'''_3, C''_3, C'_3 and the arcs having their centers on the x-axis and the y-axis, respectively (see Figure 1).

In the case of $O_{4,b}$, the 8 contact points are reduced to 4, then $T_{x3} = T_{y3}$ (we call it T_{xy}), and similarly: $T'''_{xy} = T'''_{x3} = T'''_{y3}$, $T''_{xy} = T''_{x3} = T''_{y3}$, $T'_{xy} = T'_{x3} = T'_{y3}$.

And we use the following notation: θ is the the angle $\angle(\overrightarrow{P_xA}, \overrightarrow{P_xT_{x3}})$ in the oval $O_{8,b}$, Θ is the angle $\angle(\overrightarrow{P_xA}, \overrightarrow{P_xT_{xy}})$ in the oval $O_{4,b}$, and μ is the distance $d(P_x, P_3)$ between P_x and P_3.

II. AN EIGHT-CENTERED OVAL WHICH IS QUASI-EQUIVALENT TO THE ELLIPSE

There is no oval $O_{4,b}$ having the same center, axes and vertices as $\mathcal{E}_b$, and also having the same curvature at the vertices; but in paper [9] it was shown that:

Theorem 7 *There is only one oval* $O^{c-l}_{8,b}$*sharing the vertices with* $\mathcal{E}_b$*, having the same curvature at the vertices, i.e., with* $E^c_b(O^{c-l}_{8,b}) = 0$ *in equation (5), and also the same perimeter length. For* $O^{c-l}_{8,b}$ *the analytical expressions for the circle centers* $P_x = (x,0)$*,* $P_y = (0,y)$*, and for circle center* P_3 $x = 1 - b^2$*,* $y = b - \frac{1}{b}$ *and* $P_3 = (x - \mu\cos\theta, -\mu\sin\theta)$ *with* μ *given in equation (6) and* θ *is the zero of the function* H^{c-l}_b *given in equation (1) with equations (2), (3) and (4).*

$$\mathbb{H}^{c-l}_b(\theta) = L - \pi\,(1+b) \sum_{n=0}^{n=\infty} \left(\frac{\sqrt{\pi}}{n!(1-2n)\Gamma\left(\frac{1}{2}-n\right)} \left(\frac{1-b}{1+b}\right)^n \right)^2, \tag{1}$$

$$L = 4b^2\theta + \frac{4}{b}\theta_y + 4\left(b^2 + \mu\right)\left(\frac{\pi}{2} - \theta - \theta_y\right), \tag{2}$$

$$\theta_y = \arctan\frac{\lambda\left(1-b^2-\mu\cos\theta\right)}{-\lambda y-\lambda\mu\sin\theta}, \tag{3}$$

$$\lambda = 1 + \frac{\mu+b^2}{\sqrt{y^2+\mu^2+(1-b^2)^2+2\mu\left(y\sin\theta-(1-b^2)\cos\theta\right)}}, \tag{4}$$

$$\Gamma(\alpha) = \int_0^\infty t^{\alpha-1}e^{-t}dt$$

The quadratic error $E^c_b(O_{8,b})$ between the curvatures $k_A(\mathcal{E}_b)$, $k_B(\mathcal{E}_b)$ of the ellipse $\mathcal{E}_b$ at the vertices A, B and the curvatures $k_A(O_{8,b})$, $k_B(O_{8,b})$ of an oval $O_{8,b}$ at the vertices A, B, is

$$E^c_b(O_{8,b}) = \left(k_A(\mathcal{E}_b) - k_A(O_{8,b})\right)^2 + \left(k_B(\mathcal{E}_b) - k_B(O_{8,b})\right)^2\,, \tag{5}$$

The oval $O_{8,b}^{c-l}$ has center point $P_3(\theta)$ with $P_3(\theta) = (x - \mu\cos\theta, -\mu\sin\theta)$,

$$\mu = \frac{1}{2}\frac{b(b-1)}{b^2\cos\theta - b^2 + b\sin\theta + b\cos\theta - b + \sin\theta - 1}. \qquad (6)$$

The oval $O_{8,b}^{c-l}$ has the following contact points, see Figure 1:

$$T_{x3} = \left(1 - b^2 + b^2\cos\theta, b^2\sin\theta\right), \qquad (7)$$

$$T_{y3} = \left(\lambda\left(1 - b^2 - \mu\cos\theta\right), y - \lambda y - \lambda\mu\sin\theta\right). \qquad (8)$$

Remark 9 of [9]. We point out that there is no 8-centered oval $O_{8,b}$ having the same vertices, the same surface area and the same perimeter length as the ellipse $\mathcal{E}_b$.

A rigorous definition of the deformation error between the ellipse and the oval is the following: For each point $p \in \mathcal{E}_b$ let $q_p \in O_{8,b}$ be the point, which is closest to p among all points of intersection between $O_{8,b}$ and the straight line perpendicular to the ellipse at p. The maximum value of the distance $d(p, q_p)$, when p moves along the ellipse $\mathcal{E}_b$, is called the *deformation error* $E(\mathcal{E}_b, O_{8,b})$ between the two curves.

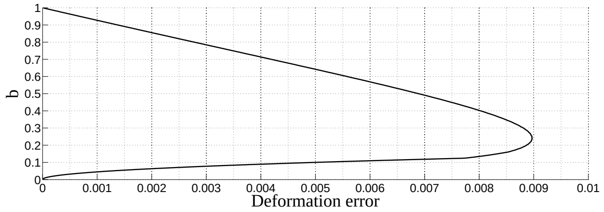

Figure 2. Graph of $\mathcal{A}(O_{\mathcal{E}_b}) - \mathcal{A}(\mathcal{E}_b) = \Delta\mathcal{A}_b$.

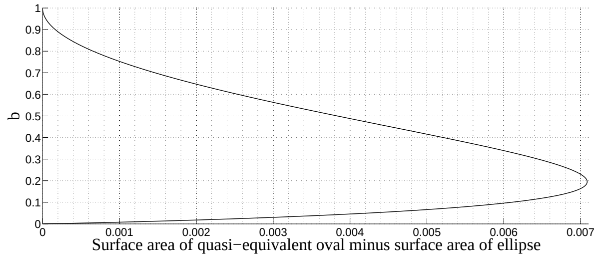

Figure 3. Graph of $\mathcal{A}(O_{\mathcal{E}_b}) - \mathcal{A}(\mathcal{E}_b) = \Delta\mathcal{A}_b$.

In [9] it was calculated, by making a software using the above equations (1) to (6), the deformation error $E(\mathcal{E}_b, O_{8,b}^{c-l}) = E_b$ for all values of parameter b, and we have shown it in the graph of Figure 2.

Furthermore, in [9] it was calculated the difference $\mathcal{A}(O_{8,b}^{c-l}) - \mathcal{A}(\mathcal{E}_b) = \Delta\mathcal{A}_b$ of their surface areas, and we have shown it, for all values of parameter b, in the graph of Figure 3. And it was proved that the eight-centered oval $O_{8,b}^{c-l}$ has not only the same vertices, perimeter length, curvature and curvature at the vertices as $\mathcal{E}_b$, but also only a small difference of the surface areas and a small deformation error. This qualifies to the oval $O_{8,b}^{c-l}$ "quasi-equivalent" to the ellipse $\mathcal{E}_b$, in short, we will call it $O_{\mathcal{E}_b}$.

III. EIGHT-CENTERED OVAL QUASI-EQUIVA- LENT TO THE KEPLER'S ELLIPSE OF PLANETS' TRAJECTORY

Applying the above formulae to the ellipse of the planets' trajectory, we have the following results:

Table 2. Calculations for $O_{\mathcal{E}_b}$ of planets' trajectory.

	Mercury	Venus	Earth	Mars
ϵ	0.205600	0.006700	0.016700	0.093500
b	0.978636	0.999978	0.999861	0.995619
θ	0.451296	0.445567	0.445597	0.446742
E_b	0.000290	0.000002	0.000002	0.000059
$\Delta\mathcal{A}_b$	0.000008	0.000000	0.000000	0.000001
	Jupiter	Saturn	Uranus	Neptune
ϵ	0.048900	0.056500	0.045700	0.011300
b	0.998804	0.998403	0.998955	0.999936
θ	0.445878	0.445984	0.445838	0.445579
E_b	0.000017	0.000021	0.000013	0.000002
$\Delta\mathcal{A}_b$	0.000000	0.000000	0.000000	0.000000

All the geometric elements of $O_{\mathcal{E}_b}$ are determined by eccentricity ϵ of Table 2 and the formulae of Section 3.

For example, for Mars we have:

$b \simeq 0.995619$, $\theta \simeq 0.446724$, $P_x \simeq (0.008742, 0)$,

$P_y \simeq (0, -0.008781)$, $P_3 \simeq (0.002833, -0.002\,831)$,

$T_{x3} \simeq (0.902\,725, 0.428\,237)$, $T_{y3} \simeq (0.431\,808, 0.898\,061)$.

The calculation steps for this example are as follows:

With equation of eccentricity

$\epsilon = 0.093500$ with $a = 1 \Rightarrow 1 \simeq b^2 + 0.093500^2 \Rightarrow$

$\Rightarrow b \simeq 0.995619$.

With Theorem 7 of [9] in Section 3 of this paper

$$P_x = \left(1 - b^2, 0\right) \simeq \left(1 - 0.995\,619^{\,2}, 0\right) \simeq (0.008\,742\,, 0),$$

$$P_y = \left(0, b - \tfrac{1}{b}\right) \simeq \left(0, 0.995\,619 - \tfrac{1}{0.995\,619}\right) \simeq$$

$$\simeq (0, -0.008\,781),\ y = -0.008\,781.$$

With equation (1)

$$\xi = \pi\,(1 + b)\sum_{n=0}^{n=\infty}\left(\frac{\sqrt{\pi}}{n!(1-2n)\Gamma\left(\frac{1}{2}-n\right)}\left(\frac{1-b}{1+b}\right)^n\right)^2 \simeq$$

$$\simeq \pi\,(1 + 0.995619)\sum_{n=0}^{n=\infty}\left(\frac{\sqrt{\pi}}{n!(1-2n)\Gamma\left(\frac{1}{2}-n\right)}\left(\frac{1-0.995619}{1+0.995619}\right)^n\right)^2,$$

then $\xi \simeq 6.269430$.

Now, using an iterative numerical method we calculate the implicit value θ such that:

with equation (6)

$$\mu = \frac{1}{2}\frac{b(b-1)}{b^2\cos\theta - b^2 + b\sin\theta + b\cos\theta - b + \sin\theta - 1};$$

and with equation (4)

$$\lambda = 1 + \frac{\mu + b^2}{\sqrt{y^2 + \mu^2 + (1-b^2)^2 + 2\mu\left(y\sin\theta - (1-b^2)\cos\theta\right)}};$$

and with equation (3)

$$\theta_y = \arctan \frac{\lambda\left(1-b^2-\mu\cos\theta\right)}{-\lambda y-\lambda\mu\sin\theta};$$

and with equation (2) we have that

$$L = 4b^2\theta + \tfrac{4}{b}\theta_y + 4\left(b^2+\mu\right)\left(\tfrac{\pi}{2}-\theta-\theta_y\right) \simeq 6.269430.$$

So, we find, with an iterative numerical method, that $\theta \simeq 0.446724$ and also $\mu \simeq 0.006552$, $\lambda \simeq 152.405404$, $\theta_y \simeq 0.444\,399$.

We think it could be a good exercise for physics undergraduate students to make a software of a numerical method to reproduce the calculations.

Finally, with Theorem 7 of [9] in Section 3 of this paper

$$P_3 = (x-\mu\cos\theta, -\mu\sin\theta) \simeq (0.002833\ -0.002\,831);$$

with equation (7)

$$T_{x3} = \left(1-b^2+b^2\cos\theta, b^2\sin\theta\right) \simeq (0.902\,725, 0.428\,237\,);$$

and with equation (8)

$$T_{y3} = \left(\lambda\left(1-b^2-\mu\cos\theta\right), y-\lambda y-\lambda\mu\sin\theta\right) \simeq$$

$$\simeq (0.431\,808\,0.898\,061\,).$$

Table 2 shows that the maximum difference –deformation error– $E(\mathcal{O},\mathcal{E}_b)$ between the positions given by the circumference $\mathcal{O}$ and the Kepler's ellipse $\mathcal{E}_b$ –Table 1– is greater than the maximum difference –deformation error– $E(\mathcal{E}_b, O_{\mathcal{E}_b})$ between the positions given by the quasi-equivalent oval $O_{\mathcal{E}_b}$ and the Kepler's ellipse $\mathcal{E}_b$. Also the deformation error $E(\mathcal{E}_b,\mathcal{C}_b)$ between the positions given by the Cassinian oval $\mathcal{C}_b$ and the Kepler's ellipse $\mathcal{E}_b$ –Table 1– is greater than the deformation error $E(\mathcal{E}_b, O_{\mathcal{E}_b})$. For Mercury and Mars, with greater eccentricity, this maximum difference –deformation error $E(\mathcal{E}_b, O_{\mathcal{E}_b})$– is two order of magnitude lower than in the case of circumference $\mathcal{O}$ and Cassinian oval $\mathcal{C}_b$; and for the rest of planets' deformation error $E(\mathcal{E}_b, O_{\mathcal{E}_b})$ is one or two order of magnitude lower.

Moreover Table 2 shows that difference $\mathcal{A}(O_{\mathcal{E}_b}) - \mathcal{A}(\mathcal{E}_b)$ of their surface areas: for Mercury and Mars are barely distinguishable; and for the rest of planets are practically negligible.

Table 1 -Morgado and Soares [13]- shows that, for Mars, Cassini's oval is barely distinguishable from Kepler's ellipse (deformation error 0.004400), but it is distinguishable near to the minor semi-axis for Mercury with high eccentricity (deformation error 0.021841). Figure 2 of [13] shows visually this deformation error for Mercury. However, Table 2 shows that, even for Mercury, a figure can not display visually the deformation error between Kepler's ellipse $\mathcal{E}_b$ and the quasi-equivalent oval $O_{\mathcal{E}_b}$ (deformation error for Mercury is 0.000290).

IV. CONCLUSION

With the results of this paper, we have an approximation of the Kepler's ellipse of the planets' trajectory by circular arcs, which is *quasi-equivalent*, that is: we have presented the approximation of the Kepler's ellipse $\mathcal{E}_b$ by the eight-centered oval $O_{\mathcal{E}_b}$ having the same center, axes, vertices, perimeter length and curvature at the vertices as $\mathcal{E}_b$, and also having practically negligible difference with respect to the surface area $\mathcal{E}_b$, and showing barely indistinguishable deformation error in relation to $\mathcal{E}_b$.

Then the oval $O_{\mathcal{E}_b}$ and the corresponding ellipse $\mathcal{E}_b$ are numerically barely distinguishable. Therefore, we think it could be a good exercise for undergraduate level physics to discuss these ovals as quasi-equivalent curves related to the Kepler's ellipse of planets' trajectory because the results show that it is not enough to consider only numerical measures to decide which are the actual laws governing the planetary movement. This paper discusses differences and similarities among ovals and ellipses by solving a set of algebraic equations, we think it could be a good exercise for physics undergraduate students to make a software of a numerical method to reproduce the calculations. We think this discussion could be interesting to the readers because it is well known that before to decide by the ellipse as the best curve to describe planet's orbit, Kepler tried to fit different ovals to the Tycho Brahe's astronomical data.

REFERENCES

[1] T. Banchoff, and P. Giblin, Am. Math. Mon. 101, 403 (1994).

[2] A. A. Mazzotti, Nexus Netw. J. 16, 389 (2014).

[3] A. A. Mazzotti, Nexus Netw. J. 16, 345 (2014).

[4] P. L. Rosin, Math. Intell. 23, 58 (2001).

[5] P. L. Rosin, Comput. Aided Geom. Des. 16, 269 (1999).

[6] P. L. Rosin, Graph. Mod. Im. Proc.60, 209(1998).

[7] P. L. Rosin, M. L. V. Pitteway, Math. Gazette. 85, 13 (2001).

[8] F. R. Honey, Pop. Astronomy. 16, 617 (1908).

[9] B. Herrera, and A. Samper, J. Geom. Graph. 19, 257 (2015).

[10] J. Kepler and translator W. H. Donahue, *The New Astronomy*, (Cambridge University Press, Cambridge, 1992).

[11] I. B. Cohen, J. Hist. Med. Allied Sci. 17, 72 (1962).

[12] J. Sivardiere, Eur. J. Phys. 15, 62 (1994).

[13] B. Morgado, and V. Soares, Eur. J. Phys. 35, 025009 (2004).

[14] P. S. M. de Laplace, *Mécanique Céleste, vol 1*, (Hilliard, Gray, Little and Wilkins, Boston, 1829).

ACTIVELY ROTATING GRANULAR PARTICLES MANUFACTURED BY RAPID PROTOTYPING

PARTÍCULAS GRANULARES QUE ROTAN ACTIVAMENTE FABRICADAS MEDIANTE PROTOTIPADO RÁPIDO

C. Scholz[†] y T. Pöschel

Institute for Multiscale Simulation, Nägelsbachstraße 49b, FAU Erlangen-Nürnberg, 91052 Erlangen, Germany
† autor para la correspondencia

Recibido 17/8/2015; Aceptado 17/9/2015

We study actively rotating granular particles manufactured by rapid prototyping. Such particles, as introduced in Ref. [1], convert vibrational motion into rotational motion via tilted elastic legs in a circular arrangement at the bottom of the particle. We extend the original design of the particles to make them suitable for mass-fabrication via rapid prototyping. The rotational velocity is measured in dependence of the driving frequency and amplitude. We find two different regimes of motion. For small amplitudes the particle performs a slow and stable rotation, while above a certain threshold the particle starts to perform a precission and consequently rotates significantly faster.

Estudiamos girando activamente partículas granulares fabricados por prototipado rápido . Tales partíıculas , como se introdujo en Ref. [1], convierten el movimiento de vibración en el movimiento de rotación a través de las piernas elásticos inclinados en una disposición circular en la parte inferior de la partícula. Extendemos el diseño original de las partículas para que sean adecuados para la fabricación en serie a través de prototipado rápido. La velocidad de rotación se mide en la dependencia de la frecuencia de excitación y la amplitud. Nos encontramos con dos regímenes diferentes de movimiento. Para las pequeñas amplitudes la partícula realiza una rotación lenta y estable, mientras que por encima de un cierto umbral la partícula comienza a realizar una precision y por consiguiente gira mucho más rápido.

PACS: 45.50.Dd Motion (classical mechanics), 87.19.lu Locomotion (motor systems), 81.05.Rm Granular materials, 81.05.Rm Granular materials fabrication

Particles that perform active motion store and convert energy in internal degrees of freedom to execute a locally directed motion. Examples for such objects are living organisms [2,3], robots [4] and artificial microswimmers [5].

In granular systems some strategies have been suggested to construct such particles. Cylinders [6] and disks [7] with asymmetric mass-distribution have been excited by vertical vibrations to perform a directed motion. Another possibility is to construct particles with asymmetric shape. Chiral S- and U-shaped particles have been shown to convert vibrational into rotational motion [8]. However the interaction of these particles is rather complicated due to their complex shape. In [1] a particle design, called Vibrot, has been suggested, where a ratchet configuration of tilted legs aligned in a circle has been used to achieve a conversion of vibration into rotation. Here the caps of the particles can be almost independently designed from the legs, so that a large variety of particle shapes can be realized. For investigations of the collective behavior of ensembles of such particles, we are faced with the problem to manufacture a sufficient number of particles with small statistical variance.

Here we present an analysis of Vibrot particles manufactured by rapid prototyping. The mean rotational velocity $\overline{\omega}$ of these particles depends on the excitation frequency f_D and amplitude A similar to the original Vibrots from [1]. However, due to the increased stiffness of the legs compared to the original design, we observe two types of motion. For small A we observe a slow rotation and for high A the particles perform a fast rotation overlapped by a precession, therefore, called tumbling regime. The transition from slow to fast rotation is rather sharp, however a transient regime, where tumbling and slow rotation of the particle can both occur is observed in between.

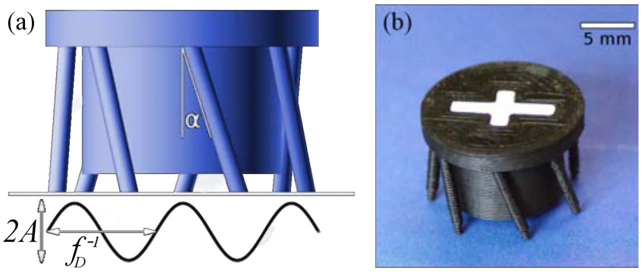

Figura 1. (a) Sketch of the Vibrot. The legs are tilted by $\alpha = 18°$. (b) Photography of a Vibrot manufactured by rapid prototyping. Particles are marked by a cross to simplify tracking of the particle motion.

The original design of the Vibrot contained three elastic legs made of rubber attached to a soft-drink cap. While this assembly is inexpensive and made from household materials such particles are not easily fabricated in large quantities. One possibility to do so, is by rapid prototyping. For this we employed the following changes to the design. The hollow soft-drink cap is replaced by a flat disk with a diameter of 15 *mm* and a height of 2 *mm*, to which a cylinder (height 6 *mm*, diameter 11 *mm*) is attached at the bottom, to lower to center-of mass and stabilize the motion. The total number of legs (length 8.5 *mm*, tilt angle $\alpha = 18°$) is increased to seven. This makes the particles more stable against toppling over, when hit from the side. Even numbers of legs are not suitable since in this case the contact points of the legs on a flat surface are symmetric and the particle typically wobbles around the symmetry axis. If the number of legs is too large, legs can join to the central cylinder or break off due to imperfections of the printing process. In systematic tests seven legs appeared to be the optimal number, that increases the stability of the particles, without decreasing the manufacturing throughput significantly.

Particles are printed using a fused filament fabrication (FFF) technique. As printing material acrylonitrile butadiene styrene (ABS) is used. The material has a bulk elastic modulus of 1.5 *GPa*, a density of 1.07 g/cm^3 and a Poisson's ratio of 0.35. Since during the manufacturing the material is deposited in layers, air can be trapped inside small imperfections, which typically reduces the effective density and increases the effective elastic modulus.

To investigate the dynamic properties of a single particle the Vibrot is placed on a polished PMMA (polymethyl methacrylate) plate that is mounted to a electromagnetic shaker and excited by vertical vibrations. Figure 2 shows the mean rotational velocity ϖ of the Vibrot in dependence of the excitation amplitude A at a driving frequency of $f_D = 50$ *Hz*. No motion is observed for $A < 0.1$ *mm*. For larger A the particles perform a slow rotation where ϖ increases monotonously with A. For amplitudes $A > 0.16$ *mm*, particles start to perform a fast rotation superimposed by a precession motion, therefore called tumbling regime.

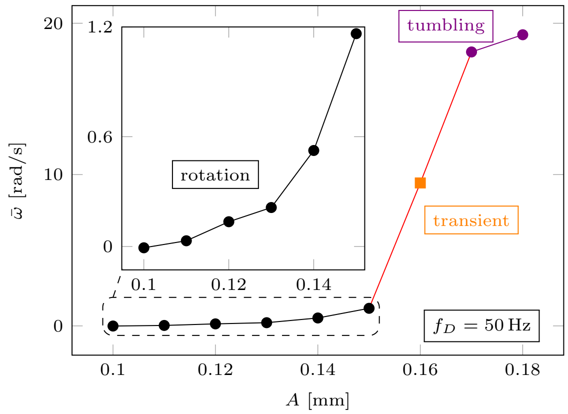

Figura 2. Mean rotational velocity ϖ of a Vibrot as a function of the excitation amplitude A at a constant frequency $f_D = 50$ *Hz*. Error bars are on the order of the marker size.

Additionally we also measure the instantaneous rotational velocity ω of a particle using a high-speed camera at up to 200 *fps* (see Fig. 3). We find a rather wide distribution, which indicates that ω varies due to the motion mechanism and surface inhomogeneities. In case of the mode of slow rotation, we observe a symmetric distribution around ϖ while in the tumbling regime the distribution is asymmetric. In the transient mode, we observe coexistence of both types of motion.

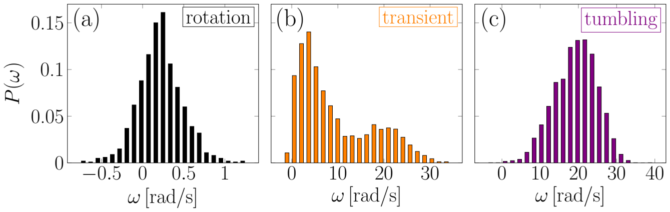

Figura 3. Distribution of instantaneous rotational velocity ω in the regimes of (a) slow, (b) transient and (c) tumbling motion.

Due to the occurrence and transition between different motion regimes the dependence of ϖ on the frequency is more complex, compared to the dependence on amplitude. Figure 4 shows ϖ *vs* f_D for two different values of the amplitude. For a low amplitude the particle performs slow rotation where f_D depends non-monotonously on the frequency characterized by a minimum at $f_D = 50$ *Hz*. For large amplitude, we observe slow rotation at low frequency and tumbling motion for $f_D \geq 30$ *Hz*, where the rotational velocity decreases with increasing f_D.

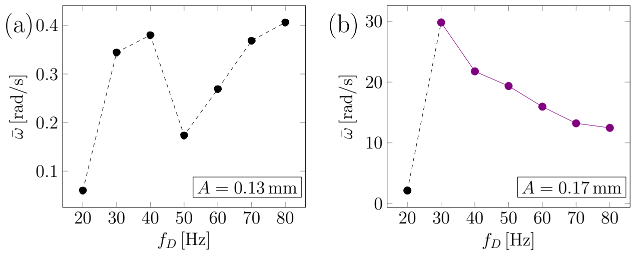

Figura 4. Mean rotational velocity ϖ of a Vibrot as a function of the excitation frequency f_D for (a) $A = 0.13$ *mm* and (b) $A = 0.17$ *mm*. Error bars are on the order of the marker size.

In summary, we manufactured actively rotating particles using rapid prototyping. The particle design allows the fabrication of particles in large quantities with well-defined rotational velocity, depending on the excitation parameters. The collective motion of such particles reveals a number of exciting effects to be reported elsewhere.

REFERENCES

[1] E. Altshuler, J. M. Pastor, A. Garcimartín, I. Zuriguel and D. Maza, PloS One 8, e67838 (2013).

[2] D. J. Pearce, A. M. Miller, G. Rowlands and M. S. Turner, Proc. Nat. Acad. Sci. 111, 10422 (2014).

[3] E. M. Purcell, Am. J. Phys. 45, 3 (1977).

[4] M. Rubenstein, A. Cornejo and R. Nagpal, Science 345, 795 (2014).

[5] I. Buttinoni, J. Bialké, F. Kümmel, H. Lowën, C. Bechinger and T. Speck, Phys. Rev. Lett. 110, 238301 (2013).

[6] A. Kudrolli, G. Lumay, D. Volfson and L. S. Tsimring, Phys. Rev. Lett. 100, 058001 (2008).

[7] J. Deseigne, O. Dauchot and H. Chaté, Phys. Rev. Lett. 105, 098001 (2010).

[8] J.-C. Tsai, F. Ye, J. Rodriguez, J. P. Gollub and T. Lubensky, Phys. Rev. Lett. 94, 214301 (2005).

Rev. Cub. Fis. **33**, 39 (2016) ARTÍCULOS ORIGINALES

THE NEWTONIAN MECHANICS OF A VIBROT

LA MECÁNICA NEWTONIANA DE UN VIBROT

H. Torres[a†], V. M. Freixas[a] y D. Pérez[b]

a) Facultad de Física, Universidad de La Habana, Cuba; htorres@física.cu[†]
b) Instituto Superior de Tecnologías y Ciencias Aplicadas, Cuba; adan@instec.cu
† corresponding author

Recibido 15/10/2015; Aceptado 16/2/2016

A mechanical model was developed to describe the behaviour of a device able to transform vibrations into rotations, named Vibrot. The theoretical model, developed in the newtonian formulation of mechanics, was able to reproduce qualitatively all the experimental results existing in the literature and quantitatively some of them.

Se desarrolló un modelo mecánico para describir el comportamiento de un dispositivo capaz de convertir energía cinética en forma de vibración en energía cinética rotacional, llamado Vibrot. El modelo teórico, desarrollado en la formulación newtoniana de la mecánica, corroboró cualitativamente todos los resultados experimentales existentes en la literatura y cuantitativamente algunos de ellos.

PACS: Newtonian mechanics, 45.20.D-; Dynamics and kinetics of rigid bodies, 45.40.-f; Classical mechanics of continuous media, 83.10Ff

I INTRODUCTION

Devices able to transform rotational energy into kinetic energy along the rotation axis have been very used for ages. Archimedes of Syracuse is credited with the invention of one of these devices, nowadays known as "Archimedes's screw", whose basic working principle is still used [1]. This kind of phenomenon have been well studied because of its direct implications in the industry, but what about the inverse phenomenon? The mysterious rotation of the statue of Neb-Senu, [2], attracted the attention of several believers who explained it by formulating fanciful hypothesis. Nevertheless, the physicist Brian Cox formulated a more realistic one, where the vibrations produced by the steps of the visitors induced a rotation on the statue, [2].

In order to unravel the working principle behind this phenomenon we will focus our attention in a simple device named Vibrot (*vib*ration to *rot*ation). A complete experimental description of a Vibrot as the one we aim to describe theoretically, may be found in [3].

II THE MODEL

A Vibrot as the one designed by Altshuler *et al.* in [3], is shown in Fig. 1a. We model a Vibrot as a head resting on three legs. The head consists in an homogeneous cylinder of radius $R = 15\ mm$ and height $h = 12\ mm$. Each of the legs is made by a spring of equilibrium length $l = 11\ mm$ and elastic constant $= 400\, N/m$. The upper side of the springs are attached to the Vibrot's body at a distance $r = 12$ mm from the center of the cylinder's bottom. A light rod freely slides inside each spring, and touches the ground through a disk. The three legs are axially symmetric relative to the bottom base, and are inclined $\alpha = 30^o$ relative to the vertical (see Fig. 1b).

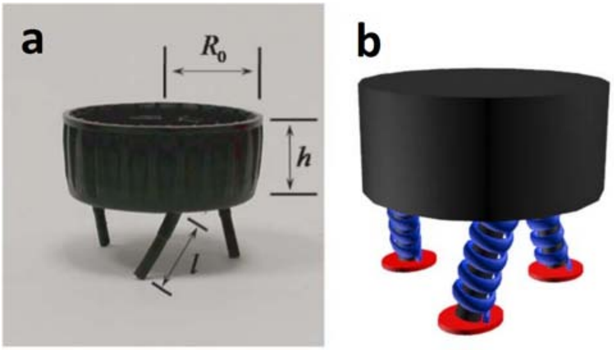

Figure 1. a) Photograph of a Vibrot taken from [3], and b) Sketch of our model Vibrot.

The vibrations of the platform used in [3], can be introduced by means of an acrylic surface that vibrates sinusoidally in the vertical direction (*i.e.* along the gravity), with a frequency f_v and amplitude A. Our reference system was taken on the vibrating surface, so it is an accelerated framework. In order to describe the temporal evolution of the Vibrot we use the following coordinates:

- $z(t)$: axis perpendicular to the base of the cylinder passing through its center.
- $\varphi(t)$: rotation angle of any point located in the cylinder's base.

We first describe the forces acting along the z-axis. The gravity force $F_g = mg$ points downwards, where m is the Vibrot's mass, and $g = 9.8\ m/s^2$ is the acceleration of the gravity. When the springs are compressed a length Δl, an elastic force $F_e = 3k\Delta l\cos()(\alpha)$ is applied upwards. That happens when the distance between the base of the cylinder and the ground is smaller than $l\cos(\alpha)$. Otherwise the Vibrot is in its "ying phase" and $F_e = 0$, while springs keep their equilibrium length. As a consequence of taking an accelerated reference system we also have an inertial force, $F_i = m\omega^2 A cos(\omega t) = mg\Gamma cos(\omega t)$, where $\Gamma = A\omega^2/g$ is the dimensionless acceleration and $\omega = 2\pi f_v$ the angular velocity.

It is important to take into account, that every time the Vibrot collides with the platform, part of its kinetic energy is dissipated as heat and, like there is not previous models of a Vibrot, we will assume it happens due to a viscous friction. Strictly, this viscous force regards also the interaction between the Vibrot and the surrounding air, but this contribution can be neglected (the change in the kinetic energy by "air-friction" is much less than by "platform-friction"), so we assume that the viscous friction only mimics the collision between the Vibrot and the acrylic surface. Then, in the z-axis there is also a viscous force $F_v = -b\dot{z}(t)$, where the parameter b will be determined from the experimental data.

If we define the variable $\xi(t) = z(t) - lcos(\alpha)$, the viscous and elastic forces can be written as

$$F_v = -b\dot{\xi}(t), \tag{1}$$

$$F_e = -k\xi(t). \tag{2}$$

As we mentioned before, the elastic force only acts when the Vibrot is touching the platform ($\xi < 0$). To introduce this information we can use the Heaviside function, $\Theta(x)$. Then, the elastic force is $Fe = -k\xi(t)\Theta(-\xi)$. Henceforth we will discuss the motion in the z-axis by means of the variable $\xi(t)$. We will also define $\omega_o = (2\pi f_r) = \sqrt{3k/m}$ where f_r is the rotation frequency. So, the differential equation describing the vertical motion of the Vibrot is

$$\ddot{\xi}(t) = g\Gamma\cos(\omega t) - g - \omega_o^2\xi(t)\Theta(-\xi) - \frac{1}{m}b\dot{\xi}(t). \tag{3}$$

In order to obtain the equation that describes the rotation of the Vibrot, we will pay attention to the momentum of the forces exerted on the cylinder. When the elastic force is acting, it has a component on the plane of the base of the cylinder, which has associated an absolute torque, T_e, given by

$$T_e = 3k|\Delta l|\sin(\alpha)r = 3k\xi(t)\tan(\alpha)r. \tag{4}$$

Both the torque and the elastic force are only different from zero when $\xi(t) < 0$. Furthermore, once the Vibrot touches the platform, a kinetic friction force begins to act, but quickly transforms itself into static. Modelling this force is also complicated, but we propose the following hypothesis: *once the Vibrot collides with the vibrating membrane, the torque mentioned before changes its sign, and remains this way until it reaches the minimum, where it comes back to be positive*. Moreover, as the static force cannot move the device backwards, we will assume the angular velocity to be non-negative. Also, we include a dynamic friction associated to the torque, T_{F_r}, given by Eq. 5, where was taken as average normal force the ones in the position of equilibrium of the springs.

$$T_{F_r} = -\mu mgr \tag{5}$$

The friction coefficient was taken as, $\mu = 0.5$, which is the very close to the materials used. In order to avoid that the legs of the Vibrot slide backwards, the relation $\mu_{static} > tan(\alpha)$, must be fulfilled all the time. Note that if the friction coefficient is null, wherewith the Vibrot could not rotate due to the external torque vanishes while the angular momentum conserves, then, the rotation frequency remains with the initial value, *i.e.* $f_r = 0$.

The differential equation that describes the temporal evolution of the rotation angle, $\varphi(t)$, is

$$\begin{aligned}\ddot{\varphi}(t) = &-\frac{2r}{R^2}\omega_o^2\xi(t)\tan(\alpha)\Theta(-\xi)\Theta(\dot{\varphi}(t))Sig(\dot{\varphi}(t)) - \\ &-\frac{2r}{R^2}\mu g\Theta(-\xi)\Theta(\dot{\varphi}(t))\end{aligned} \tag{6}$$

In this equation, $Sig(x)$ represents the sign function, and we used as the moment of inertia of the Vibrot, $I = 1/2mR^2$ (Moment of inertia of a cylinder). Equations 3 and 6 describe the temporal evolution of the device. We will solve them assuming that the Vibrot is at rest at $t = 0$, so the initial conditions are:

$$\varphi(0) = 0, \quad \dot{\varphi}(0) = 0, \quad \xi(0) = -\frac{g}{\omega^2}, \quad \dot{\xi}(0) = 0. \tag{7}$$

III RESULTS

Solving analytically the system of differential equations 3 and 6 is a little complicated in spite of having the first equation disengaged. So, we have to solve it numerically. However, we can reach some analytical results, as follows.

In our model, the Vibrot does not rotate if the legs are touching the ground. So, if $\xi(t)$ is negative, the Vibrot will not rotate, and it is possible to determine the threshold dimensionless acceleration Γ_{th}, below which there is no rotation. In order to do that, the equation 3 is solved for $\xi(t) < 0$, resulting the equation of a forced oscillator plus a constant. Then, if the solution for a long time ($t \gg 1/f_v$) is negative, the Vibrot will not rotate. For long times, the solution that prevails is:

$$\xi_p(t) = \frac{g\Gamma\sin(\omega t + \vartheta)}{\sqrt{(\omega^2 - \omega_o^2)^2 + (\frac{b}{m})^2\omega^2}} - \frac{g}{\omega_o^2}, \tag{8}$$

where

$$\vartheta = \arctan\left(\frac{\omega_o^2 - \omega^2}{\frac{b}{m}\omega}\right) \tag{9}$$

By imposing $\xi(t) = 0$ and $\sin(\omega t + \vartheta) = 1$ in Eq. 8, it is possible to obtain Γ_{th} as:

$$\Gamma_{th} = \frac{\sqrt{(\omega^2 - \omega_o^2)^2 + (\frac{b}{m})^2\omega^2}}{\omega_o^2} \tag{10}$$

Using in Eq. 10 the expression $\omega_o = \sqrt{3k/m}$, we obtain the dependency with the mass of Γ_{th}. Figure 2 shows the experimental result for Γ_{th} vs. m, reported in [3] as well as the one obtained here using Eq. 10.

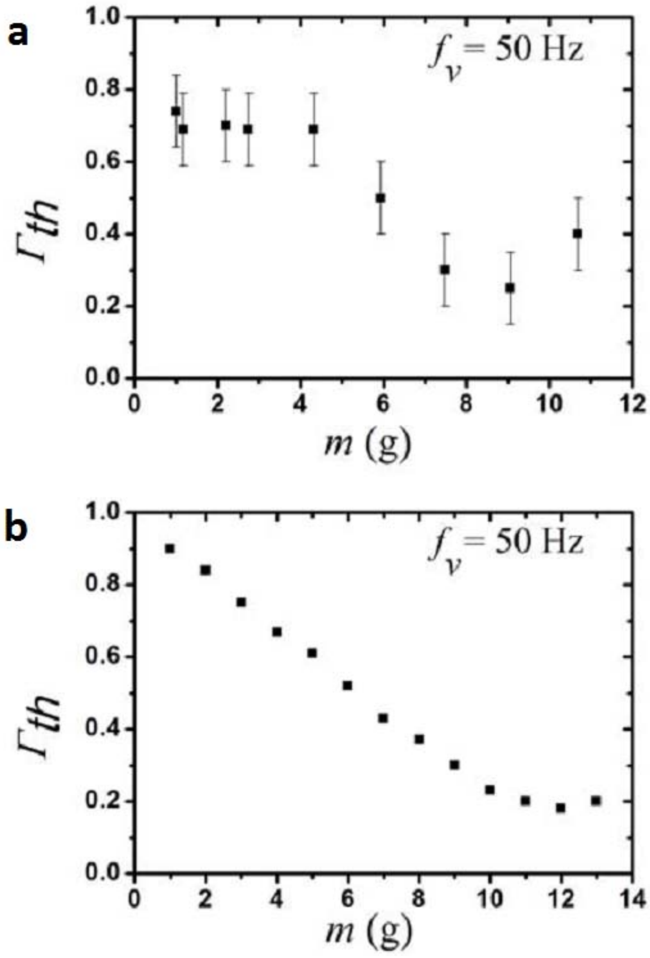

Figure 2. Comparison of the dependency of the threshold dimensionless acceleration, Γ_{th} , as a function of the Vibrot's mass, m, for a $50\,Hz$ vibration frequency, between a) Experimental results [3] and b) Theoretical results.

In Figure 2 we can see the resonance effect in both graphs. The model's results are slightly right-shifted in a value on the order of $3g$, a consequence of the choice of the parameters k and b. Here, it is important to remark the almost perfect coincidence between the numerical results and the ones obtained using Eq. 10.

We also obtained an approximation for the fly time, T_{fly}, using the following expression:

$$T_{fly} = \frac{2\dot{\xi}(t_n)}{g}, \tag{11}$$

where t_n is the n-th zero of $\xi(t)$, $(n \gg 1)$. We can see the fly time as a function of the normalized dimensionless acceleration (Γ/Γ_{th}) in Figure 3. This figure shows that both graphs have the same behaviour, although we may say that the model underestimates the fly time.

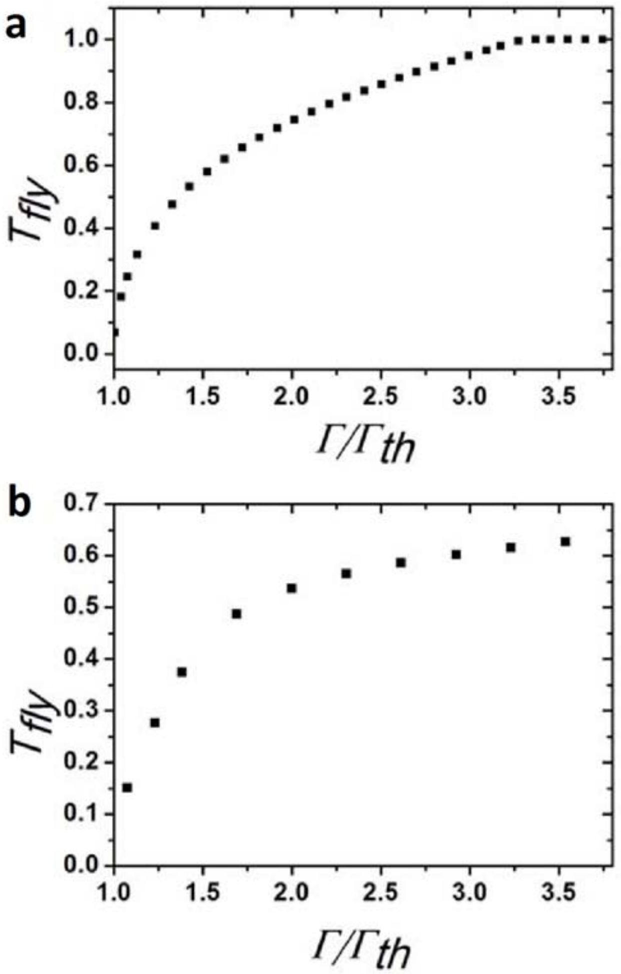

Figure 3. Comparison of the dependency of the fly time as a function of the dimensionless acceleration normalized to the threshold dimensionless acceleration, between a) Experimental results and b) Theoretical results.

Once solved numerically the system of differential equations, 3, 6 with boundary conditions given by 7, it is possible to obtain the behaviour of further magnitudes, like the rotation frequency as a function of other parameters. Experimentally, the rotation frequency is computed as the average value of the function: $\dot{\varphi}(t)/(2\pi)$, but inasmuch as this function is not constant, we calculated the rotation frequency f_r as:

$$f_r = \frac{1}{2\pi(t_2 - t_1)} \int_{t_1}^{t_2} \dot{\varphi}(t)dt = \frac{\varphi(t_2) - \varphi(t_1)}{2\pi(t_2 - t_1)}, \tag{12}$$

where the relations $t_1 > 0$, $t_2 > 0$ and $t_2 - t_1 \gg 1/f_v$, have to be satisfied. Figure 4 shows a comparison between the experimental and the model results for the Γ dependence of the rotation frequency, for a Vibrot with mass $m = 4$ g and a vibration frequency of $50\,Hz$. For the value of $\Gamma_{th} = 0.7$ the model accurately predicts the experimental results.

In Figure 5 we can see how the rotation frequency decreases as the vibration frequency increases, for a Vibrot with mass $m = 4$ g and a dimensionless acceleration, $\Gamma = 1.5$. Also, it shows a very good agreement between the experiments and the model. However, the latter predicts a "smoother" decay for high vibration frequencies.

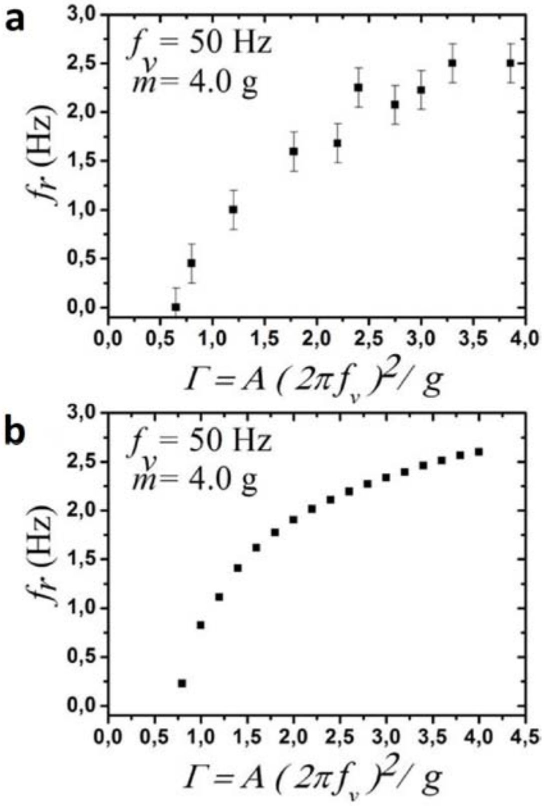

Figure 4. Comparison of the dependency of the rotation frequency as a function of the dimensionless acceleration, for a 4 g Vibrot under a 50 Hz vibration frequency, between a) Experimental results and b) Theoretical results.

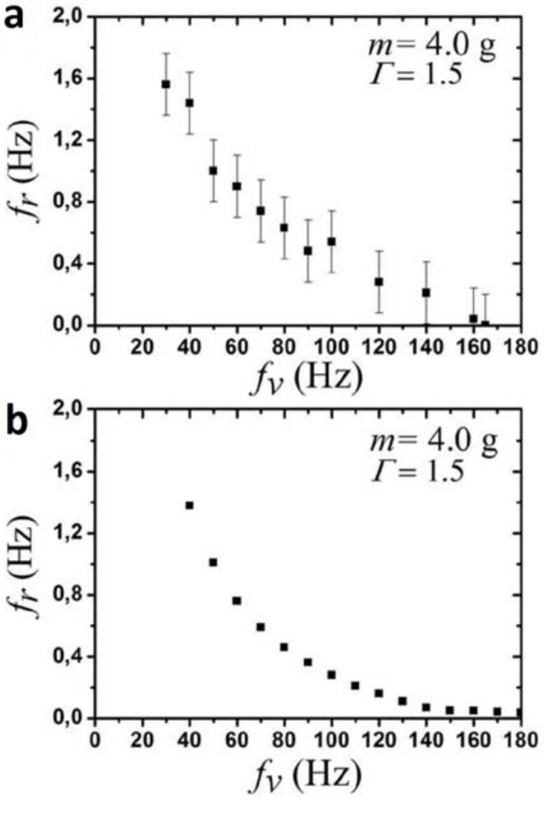

Figure 5. Comparison of the dependency of the rotation frequency as a function of the vibration frequency for a 4 g mass Vibrot under a dimensionless acceleration $\Gamma = 1.5$, between a) Experimental results and b) Theoretical results.

Our model also allows to obtain the mass-dependency of the rotation frequency, f_r. In Figure 6 we observe a very similar behaviour for small masses between the experiments and the model, but for higher masses the decrease of f_r is slower for the model. This may be due to the fact that the rubber legs of real Vibrots are mechanically deformed for high masses.

It is important to check the model's results for the case of a Vibrot with rigid legs ($k \to \infty$). In this particular case, it was experimentally proven that the device does not rotate. This was an expected result since it behaves as a rigid body. With our model, we can corroborate this result, by giving big values to k (bigger than $10^6\ N/m$). As the elastic constant increases, the rotation frequency decreases, eventually reaching values very close to zero. This fact can be explained taking into account that an increasing of k provokes an increasing in the resistance of the springs to the external force (vibrating platform), which implies a smaller amplitude, and bigger velocity and fly time, resulting in a smaller rotation frequency.

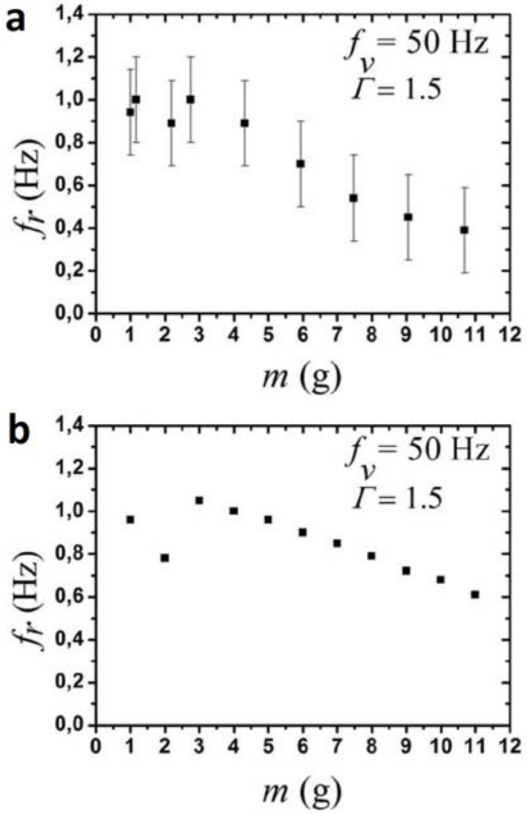

Figure 6. Comparison of the dependency of the rotation frequency as a function of the mass of the Vibrot, under a vibration frequency, $f_v = 50\,Hz$ and dimensionless acceleration, $\Gamma = 1.5$, between a) Experimental results and b) Theoretical results.

IV CONCLUSIONS

We have developed a mechanical model of a Vibrot: a device that, when put on a vibrating platform, is able to rotate due to the presence of inclined elastic legs that interacts frictionally with the vibrating platform. In order to construct the system of differential equations of the model, the reference system was taken on the vibrating platform and the rubbery legs of the experimental Vibrot [3] was modeled as linear springs inclined a certain angle relative to the normal of the base of the cylinder, which represents its body. The loss of energy mechanism was proposed as a viscous force in the vertical axis and a kinetic friction force in the angular direction. All the values to construct the model were taken from [5], except the coefficient of the viscous force, which was determined by fitting the experimental data and the friction coefficient, which was taken from the literature.

In spite of the relative simplicity of our model -entirely based in Newtonian mechanics- we have been able to reproduce semi-quantitatively or quantitatively most experimental observations on the Vibrots reported in [3]. The few discrepancies with experimental data are only quantitative, an dare probably due to the fact that we did not model the mechanical deformations of the shape of the legs (especially bending) due to the weight of the Vibrot body.

V ACKNOWLEDGMENT

We thank to Diego Maza for providing experimental data, as well as Ernesto Altshuler for launching the contest *ThinkVibrot*, which was the father of all the ideas reported in this letter.

REFERENCES

[1] Ch. Rorres, J. Hydraulic Engng., 126, 72 (2000).

[2] La estatua egipcia que se mueve por sí misma, http://mitosytimos.blogspot.com/2013/06 (2015).

[3] E. Altshuler, J.M. Pastor, A. Garcimartín, I. Zuriguel, D. Maza “Vibrot, a Simple Device for the Conversion of Vibration into Rotation Mediated by Friction: Preliminary Evaluation”,PLoS ONE 8(8): e67838. (2013)

Rev. Cub. Fis. **33**, 44 (2016) ARTÍCULOS ORIGINALES

FLUX-DENSITY TRAFFIC DIAGRAMS OF FORAGING ANTS SUGGEST ABSENCE OF JAMMING EVEN UNDER EXTERNAL PERTURBATIONS

LOS DIAGRAMAS DE TRÁFICO FLUJO-DENSIDAD PARA LAS HORMIGAS QUE FORRAJEAN SUGIEREN AUSENCIA DE "JAMMING" INCLUSO ANTE PERTURBACIONES

A. Reyes, F. Tejera y E. Altshuler†

Group of Complex Systems and Statistical Physics, Physics Faculty, University of Havana, Havana 10400, Cuba; ealtshuler@fisica.uh.cu†
† autor para la correspondencia

Recibido 17/11/2015; Aceptado 17/12/2015

A traffic flux-density diagram consists in a graph were the flux of moving particles (like cars or pedestrians) is plotted as a function of the particle density. In conventional traffic, the presence of a decreasing branch in such diagram means jamming (i.e., particles are crowded so they cannot move anymore or move very slowly). We have measured and constructed a flux-density diagram for trails of foraging ants of the species *Atta insularis*. Our diagrams do not show a decreasing branch, indicating that ants do not reach the jammed state during foraging. Moreover, the jamming-free scenario persists even when the foraging trail is perturbed by abducting ants.

Los diagramas de flujo-densidad consisten en gráficos donde se plotea el flujo vs. la densidad en partículas móviles (como autos of caminantes). En el caso del tráfico convencional, la presencia de una rama decreciente en el diagrama flujo-densidad implica "jamming" (o sea, las partículas están tan aglomeradas, que son incapaces de moverse, o se mueven muy lentamente). En este trabajo, hemos medido y construido diagramas flujo-densidad para filas de forrajeo en hormigas de la especie *Atta insularis*. Nuestros diagramas indican que las hormigas nunca alcanzan el estado de "jamming" durante el forrajeo. Adicionalmente, hemos comprobado que el escenario libre de "jamming" persiste incluso cuando la fila se perturba abduciendo individuos.

PACS: 87.23.-n, 05.45.-a, 05.65.+b

One of the most amazing features of many species of ants are foraging lines that span hundreds of meters from the nest to the feeding sources [1]. Their traffic can be characterized quantitatively by measuring the flow-density diagrams –a tool imported from the field of traffic engineering [2]. In the case of ants, differently from the case of vehicular traffic, the diagram does not show a decreasing branch [3,4], which indicates that jamming does not take place in the former system. In this paper, we offer a preliminary quantification of the traffic in foraging lanes of the Cuban leaf-cutter ants *Atta insularis* [5] by using flow-density diagrams. We perform experiments on natural nests, controlling the ant density by abducting individuals at a fixed point of the foraging lane.

Experiments were conducted on two colonies of the Cuban leaf-cutting ant *Atta insularis*, within the period January - April and September 2014. The nest was located under the pavement of the parking lot at the Institute of Materials Science and Technology (IMRE), University of Havana, and ants foraged every night on a garden located some 100 meters from the nest, partially behind a building. Most of the trajectory of the foraging trail occurred on the surface of the parking lot, especially near curbs and other edges. The experiments were performed between the 22:00 and the 23:00 hours, corresponding to the peak of activity of the colony. That guaranteed the study of the steady state, in which the number of ants coming in and out of the nest per unit time are equal and constant [6,7].

Figure 1 shows our experimental setup: the nest's door is to the left of the photograph, and the foraging trail extends to the right. Two video cameras were used: Camera 1 was near the door, immediately to its right. Camera 2 was 3 meters to the right of the door.

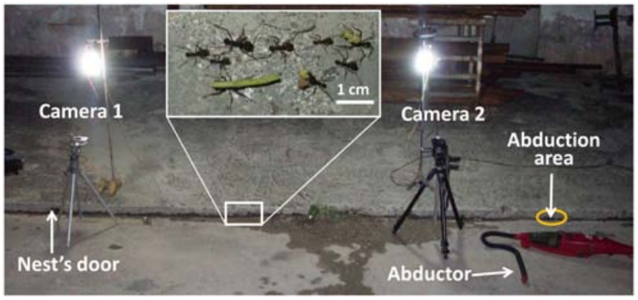

Figura 1. Experimental setup. Camera 1 is near the nest's door, Camera 2 is 3 m to the right of Camera 1, and the abduction zone is 1 m to the right of Camera 2. The Abductor (a standard vacuum cleaner) rests on the ground to the right of camera 2. The inset shows a zoom of the foraging line, where out-bound ants move from left to right, and nest-bound ants (carrying vegetal material) move from right to left.

During our experiments, two interwoven lanes of ants were established: an *out-bound* one of ants moving from the nest to the foraging area (from left to right in Fig. 1), and another of *nest-bound* ants returning from the foraging area to the nest (from right to left in Fig. 1). Our experimental protocol can be described as follows. First, the unperturbed ant trail was filmed by the two cameras for 25 minutes. This serves as baseline for the experiment, where ants showed stationary activity. Then we abducted ants using the vacuum cleaner in an area of 50 cm^2 located one meter to the right of camera 2 (see Figure 1) for either 25 or 30 minutes. Approximately 50 % ants moving in both directions were abducted. The out-bound ants coming from the left that managed to escape the predator, simply returned to the nest. After the time of the abduction, we filmed the activity for another 20 minutes. Under these conditions, two repetitions of the experiment were performed.

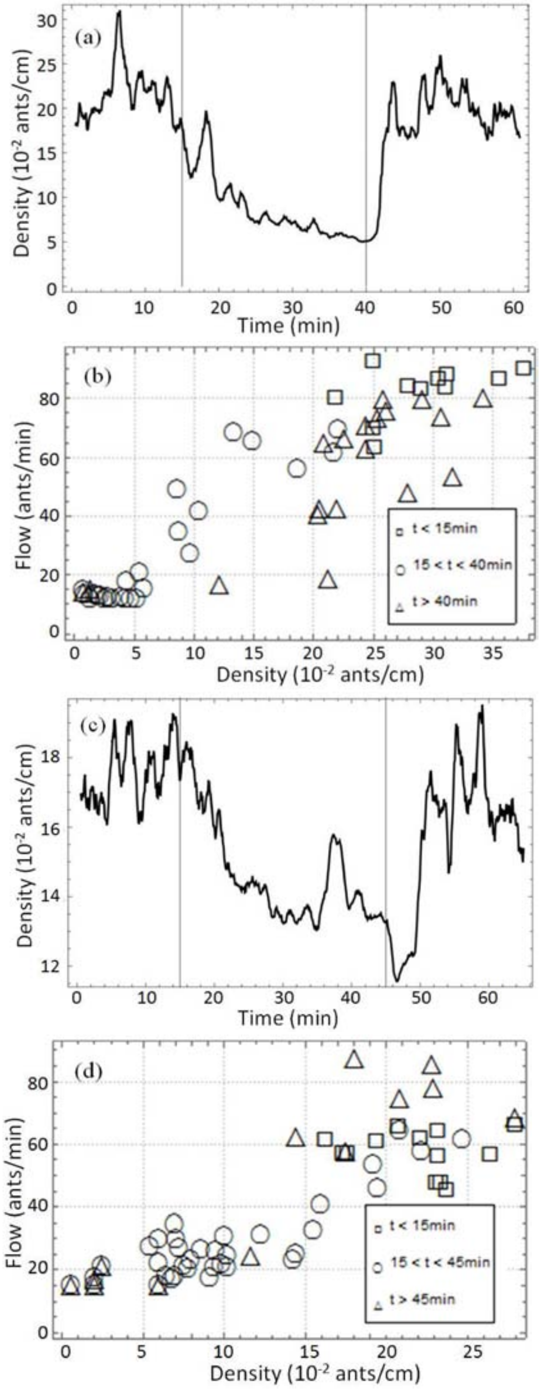

Figura 2. Evolution of the density and flow-density diagrams for ant traffic. (a) and (c) Linear density vs time for abduction periods of 25 and 30 minutes, respectively). (b) and (d) Flow vs. density traffic diagrams corresponding to abductions of 25 and 30 minutes, respectively. The data shown was acquired using camera 2, but the results using camera 1 are qualitatively analogous.

The flow of ants per minute, was determined by taking the time derivative of the cumulative number of ants determined experimentally from Camera 2 (data from Camera 1 gave similar results). To estimate the density of ants in the trail each picture from the video was binarized using an appropriate threshold. Each video frame was converted to gray scale. We chose a threshold intensity to convert all ants into black pixels and the rest into white pixels. The sequence of binarized image was used to relate the amount of black pixels in each frame with the actual amount of ants. This allowed us to construct a calibration curve to estimate the density of ants (in ants per unit length of the trail) from the number of black pixels found in each frame of video (notice that we have included here ants moving either from and to the nest). Figure 2 (a) and (c) show the evolution of the density of ants in time for abduction times of 25 and 30 minutes, respectively. With the flow and the density of ants, we constructed the fundamental diagram of traffic, shown in Figure 2 (b).

We have used different symbols for the point falling before, during and after the abduction period. Before the abduction (circles), ant flow is roughly constant, which is consistent with the fact that it is the optimal foraging flow "collectively tuned" by the colony. During the abduction period (squares) the flow decreases more of less linearly with the ant density, as previously observed *in the absence of abduction* in foraging ants [3,4]. During abduction, we have observed that roughly 50 % of the ants that reached the abduction zone (see figure 1) detected the danger, made a "U" turn, and returned to the nest. Based on our intuition from human behavior, one might expect the occurrence of jamming when those returning ants (presumably "in panic") encounter outbound nestmates moving towards the abduction area. But that was not the case: as mentioned previously, there is not a decrease branch in the flux-density diagram during abduction, which means that there is no jamming even in "panic" conditions. This is consistent with a cellular automata model where ants escaping from the abduction area do not communicate any danger information during their head-head encounters with nestmates moving towards the danger area [8]. Finally, we can see in figure 2 that, after the abduction lapse (diamonds) the flow recovers its "optimal" level as the density increases to its pre-abduction value.

In conclusion, foraging ants submitted to a controlled perturbation always follow a positive slope branch in the flow-density diagram, demonstrating the absence of jamming even in "panic" conditions –at least far enough from the disturbance area. This is consistent with earlier experiments where ants are forced to escape from a cell through thin exits: the evacuation may slow down due to the collective decision to use one of the exits; but jamming does not take place at either exit [5].

I REFERENCES

[1] B. Hölldobler and E. Wilson, The Ants (Cambridge, Belknap, 1990).

[2] D. Helbing, Rev. Mod. Phys. **73**, 1067 (2001).

[3] K. Johnson, L. F. Rossi, J. Theor. Biol. **241**, 360 (2006).
[4] A. John, A. Schadschneider, D. Chowdhury and K. Nishinari, Phys. Rev. Lett. **102**, 108001 (2009).
[5] E. Altshuler, O Ramos, Y Núñez, J Fernández, A J Batista-Leyva, and C Noda, Am. Nat. **166**, 643 (2005)
[6] S. C. Nicolis, J Fernández, C. Pérez-Penichet, F. Tejera, O. Ramos, D. J. T. Sumpter and E. Altshuler, Phys. Rev. Lett. **110**, 268104 (2013).
[7] C. Noda, J. Fernández, C. Pérez-Penichet and E. Altshuler, Rev. Sci. Inst. **77**, 126102 (2006).
[8] F. Tejera and E. Altshuler, Rev. Cubana Fis. **32**, 49 (2015).

Rev. Cub. Fis. **33**, 47 (2016) ARTÍCULOS ORIGINALES

ELECTRIC STRESS–INDUCED SLIP LINES IN JAMMED PARTICLE MONOLAYERS

LÍNEAS DE DESLIZAMIENTO INDUCIDAS POR STRESS ELÉCTRICO EN MONOCAPAS DE PARTÍCULAS EN ESTADO DE “JAMMING”

A. Mikkelsen[a†], P. Dommersnes[a] y J. O. Fossum[a]

Department of Physics, Norwegian University of Science and Technology, Trondheim, Norway; alexander.mikkelsen@ntnu.no[†]
† corresponding author

Recibido 4/1/2016; Aceptado 16/2/2016

Drops fully covered by particles, so called Pickering emulsion drops, are used to stabilize emulsions and are ideal templates for producing particles and advanced capsules. Recent studies show how electrohydrodynamic circulation flows in drops can structure free particles on their surfaces. In this article, we study the structure of Pickering drops subjected to DC E-fields. Due to its effects, we observe plastic (irreversible) deformation of the two-dimensional granuar solid covering the droplet, including particle reorganisation similar to the “grain layer gliding” and “block gliding” typical of jammed granular matter.

Las gotas cubiertas por partículas, llamadas gotas en emulsión de Pickering, se usan para estabilizar emulsiones, y son ideales para producir partículas y cápsulas avanzadas. Estudios recientes muestran que los flujos electro-hidrodinámicos circulantes en gotas pueden estructurar partículas libres sobre la superficie de las mismas. En este trabajo, estudiamos la estructura de gotas Pickering sometidas a un campo eléctrico de DC. Debido al mismo, observamos deformación plástica (irreversible) en el sólido granular bi-dimensional que cubre a la gota, incluyendo reorganizaciones de las partículas similares al “grain layer gliding” y el “block gliding” típico de la materia granular en estado de jamming.

PACS: Liquid drops, 47.55.D-, plasticity, 62.20.fq, granular flow - complex fluids, 47.57.Gc

Drops covered by capillary bound particles, known as armoured drops or Pickering emulsion drops, are ideal templates for producing particles and advanced capsules [1–3] and can be adsorbed efficiently at fluid–fluid interfaces to stabilise emulsions, thus preventing drops from coalescing [4]. Beyond their technological importance, Pickering drops are good model systems for understanding ordering and dynamics in two dimensions [5]. When the interfacial particle concentration exceeds the maximum packing fraction, jamming prevents relaxation to spherical geometry and allows for the existence of nonminimal surfaces [1, 6, 7]. The stability of Pickering drops and their properties in flow, rheology and adhesion are mainly affected by their mechanical properties such as their Young moduli, bending stiffness and Poisson ratios [8]. Pickering drops have been found to be mechanically robust and able to recover from large deformations without disintegration [9].

In response to external stress, armoured drops and bubbles have demonstrated both plastic and elastic behaviour [6–8], as well as crumpling instabilities (*i.e.*, out-of-plane deformation) [10, 11]. Similar to granular flow, grain-layer mechanisms [12], grain boundaries and scars in colloidal crystals [5], plastic capsule deformation occurs when the particle monolayer at a capsule's interface flows, giving particles space to move relative to one another. The particles rearrange to accommodate shear deformation as a new irreversible shape is formed [6].

Pickering drops respond to mechanical forces [6, 9, 13] and shear flows [14, 15]. This also includes the behaviour of clay laden Pickering drops in electric fields (E-fields) [16–19] An understanding of the mechanical response of particle-covered drops in E-fields is important for controlling Pickering emulsions and microcapsules. In this work, we have applied uniaxial stress to Pickering drops through the use of DC E-fields and have investigated the plastic deformation of Pickering drops. In particular, we have studied particle rearrangements at the drop interface at the start of plastic deformation.

The Pickering drops studied in our experiments were made of 50 cSt silicone oil (Dow Corning 200/50 cSt, electric conductivity $\sigma_{in} \sim 0.3\, pSm^{-1}$, relative permittivity $\varepsilon_{in} = 2.8$, and density $\rho_{in} = 0.961\, gcm^{-3}$) and polyethylene (PE) particles (purchased from Cospheric LLC with electric conductivity $\sigma_{pe} < 10^{-20}\, Sm^{-1}$, relative permittivity $\varepsilon_{pe} \sim 2.1$, and density $\rho_{pe} = 1.0\, gcm^{-3}$) with diameters ranging between 45 and 53 μm. The amounts of silicone oil and PE particles were measured by weight, stirred together, shaken and ultrasonicated to minimise particle aggregation.

Castor oil (Sigma-Aldrich 83912, specific density $\rho_{ex} = 0.961\, gcm^{-3}$, electric conductivity $\sigma_{ex} \sim 56\, pSm^{-1}$, relative permittivity $\varepsilon_{ex} = 4.7$, and viscosity $\mu_{ex} \sim 750 cSt$) was poured into a sample cell ($15 \times 15 \times 30\, mm$) consisting of glass and two indium tin oxide (ITO) walls acting as electrodes.

The experimental set-up is displayed in Figure 1. A silicone oil drop with PE particles is made and immersed in castor oil using a regular plastic pipette. We use particle sedimentation to bring particles to the drop interfaces where they adsorb to the oil-oil interface as a result of capillary binding forces [4]. With particles confined to the drop interface, the application of a DC E-field across the sample cell induce electro-hydrodynamic (EHD) liquid flows [20] inside and outside the drop, which are used to structure the particles at the interface. Extensive details of the method can be found in previous work [16, 21].

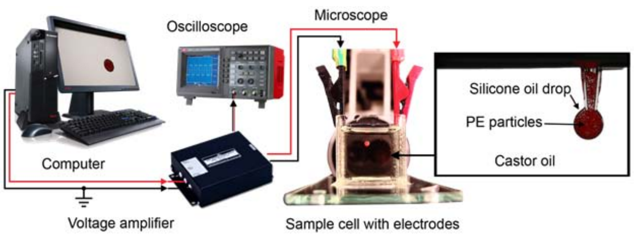

Figure 1. The experimental set-up consists of a sample cell placed on a mechanical stage, a microscope connected to a camera, a voltage amplifier, an oscilloscope to monitor signal amplitude, and a computer to control the applied voltage and record images. The sample cell is made of glass (15 × 15 × 30 mm), and two of the walls are coated with a conductive ITO layer. A drop containing colloidal particles is formed using a regular plastic pipette.

Videos and pictures were recorded using a digital camera mounted on a stereoscope, and the observation view was always in the perpendicular direction of the E-field, which was horizontal, as illustrated in all figures below.

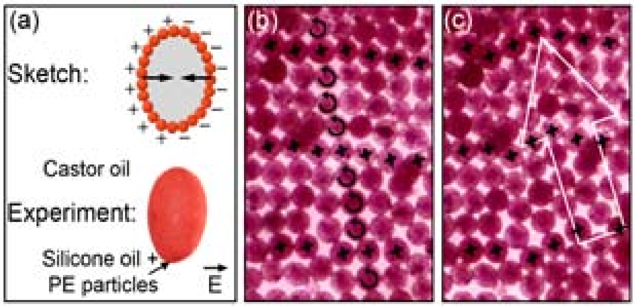

Figure 2. (**a**) A sketch and experimental images demonstrating the drop deformation process. (**b**) The Pickering drop surface in the beginning and (**c**) 3 seconds after plastic deformation. Some of the particles are marked with crosses and small arrows to illustrate how particles move and rotate relative to one another. The large white arrow illustrates how particles move collectively in a slip plane. The drop size is 1 mm, and the particle size is around 50 μm.

Figure 2**a** shows a sketch and experimental images of the silicone oil and PE Pickering drop suspended in castor oil. The application of a DC electric field was used to exert uniaxial electric stress along the Pickering drop's major axis. Since the Pickering drop and surrounding fluids have finite electric conductivities, charges accumulate at the Pickering drop interface, creating interfacial electrical shear stress [20]. The polarity of any induced surface charge depends on the conductivity of the given Pickering drop compared to the external fluid [20]. In our case, the surrounding castor oil conduct better than the Pickering drop, so the drop dipole is oriented antiparallel to the E-field direction and the electric stresses exert a compressive force on the Pickering drop. The induced electric stress is balanced by capillary stress (surface tension), which works to reduce the energy of the system and make the Pickering drop spherical. Particle jamming at the interface keep the Pickering drop non-spherical [1] and also allows for crumpled shapes [10, 11]. The particle packing at the Pickering drop surface was hexagonal, though with many irregularities at least partly due to the polydispersity of our PE particles. The structure of the particle layer may be regarded as a two dimensional granular solid. Turning off the E-field does not bring back the initial Pickering drop shape, so the deformation is plastic (irreversible).

Shortly before and during the Pickering drop collapse, we observed particle rearrangements at the Pickering drop surface (Figure 2(**b**,**c**) and Figure 3). In response to compressive electric stress, the surface particles started to move relative to one another. At low particle concentrations or when subjected to strong shear flow, particle monolayers are observed to flow with strings of particles slipping past one another, while at higher concentrations or at weak shear flow, particle domains stretch and rotate. During the plastic deformation of Pickering drops, we do not observe rotation of particles' domains or flow [22], but we do observe particle reorganisation similar to the 'grain-layer gliding' and 'block gliding' mechanisms of slow granular flow as described by Drake [12]. As particle domains widen and compress to accommodate global shear deformation, particles within domains roll onto their nearest neighbours as particle rows slide on top of one another (Figure 3). Subramaniam *et. al.* observed similar dynamics of colloidal particle monolayers rearranging in shear bands (localised sliding) in mechanically and plastically deformed bubbles covered by colloidal particles [7]. For a short moment, the particle layer displays fluid-like behaviour as the particles rearrange, and several slip lines appear at the interface.

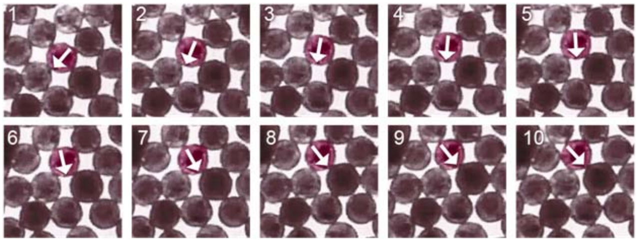

Figure 3. (1-10) A close up of particle rearrangements at the drop interface during plastic deformation. The time between each image is 2/25 seconds and the particle size is around 50 μm. The white arrows illustrate the rotation of one of the particles in the gliding plane.

These results may provide new insights regarding the mechanical strength of Pickering drops and their response to inhomogeneous stress, in particular regarding the role of slip line dynamics in jammed particle monolayers.

REFERENCES

[1] Z. Rozynek, A. Mikkelsen, P. Dommersnes and J. O. Fossum, Nature Communications 5 (2014).

[2] A. D. Dinsmore, M. F. Hsu, M. G. Nikolaides, M. Marquez, A. R. Bausch and D. A. Weitz, Science 298, 1006 (2002).

[3] A. B. Subramaniam, M. Abkarian and H. A. Stone, Nat. Mater. 4, 553 (2005).

[4] R. Aveyard, B. P. Binks, and J. H. Clint, Advances in Colloid and Interface Science 100, 503 (2003).

[5] C. Negri, A. L. Sellerio, S. Zapperi and M. C. Miguel, Proceedings of the National Academy of Sciences 112, 14545 (2015).

[6] A. B. Subramaniam, M. Abkarian, L. Mahadevan and H. A. Stone, Nature 438, 930 (2005).

[7] A. B. Subramaniam, M. Abkarian, L. Mahadevan and H. A. Stone, Langmuir 22, 10204 (2006).

[8] A. Fery and R. Weinkamer, Polymer 48, 7221 (2007).

[9] S.-Y. Tan, R. F. Tabor, L. Ong, G. W. Stevens and R. R. Dagastine, Soft Matter 8, 3112 (2012).

[10] H. Xu, S. Melle, K. Golemanov and G. Fuller, Langmuir 21, 10016 (2005).

[11] C. Monteux, J. Kirkwood, H. Xu, E. Jung, and G. G. Fuller, Physical Chemistry Chemical Physics 9, 6344 (2007).

[12] T. G. Drake, Journal of Geophysical Research: Solid Earth (1978–2012) 95, 8681 (1990).

[13] J. K. Ferri, P. Carl, N. Gorevski, T. P. Russell, Q. Wang, A. Boker and A. Fery, Soft Matter 4, 2259 (2008).

[14] I. Buttinoni, Z. A. Zell, T. M. Squires and L. Isa, Soft matter 11, 8313 (2015).

[15] S. Frijters, F. Gunther and J. Harting, Soft Matter 8, 6542 (2012).

[16] Z. Rozynek, P. Dommersnes, A. Mikkelsen, L. Michels and J. O. Fossum, Eur. Phys. J. Special Topics 223, 1859 (2014).

[17] R. B. Karyappa, S. D. Deshmukh and R. M. Thaokar, Physics of Fluids (1994-present) 26, 122108 (2014).

[18] M. Ouriemi and P. M. Vlahovska, Langmuir 31, 6298 (2015).

[19] J. W. Ha and S. M. Yang, Phys Fluids 12, 1671 (2000).

[20] G. Taylor, Proceedings of the Royal Society A: Mathematical, Physical and Engineering Sciences 291, 159 (1966).

[21] P. Dommersnes, Z. Rozynek, A. Mikkelsen, R. Castberg, K. Kjerstad, K. Hersvik and J. O. Fossum, Nature Communications 4, 2066 (2013).

[22] E. J. Stancik, G. T. Gavranovic, M. J. Widenbrant, A. T. Laschitsch, J. Vermant and G. G. Fuller, Faraday discussions 123, 145 (2003).

Rev. Cub. Fis. **33**, 50 (2016) ARTÍCULOS ORIGINALES

CHAOTIC DYNAMICS IN A SLOWLY ROTATING DRUM

DINÁMICA CAÓTICA EN UN TAMBOR GIRATORIO LENTO

H. Maghsoodi[a] and E. Luijten[a,b†]

a) Graduate Program in Applied Physics, Northwestern University, Evanston, Illinois 60208, U.S.A.
b) Departments of Materials Science & Engineering, Applied Mathematics and Physics & Astronomy, Northwestern University, Evanston, Illinois 60208, U.S.A; luijten@northwestern.edu[†]
† corresponding author

Recibido 19/3/2016; Aceptado 19/4/2016

Recent computational work (Banigan *et al.*, Nat. Phys. 9, 288 (2013)) has demonstrated that jamming and unjamming in a shear cell can be described in terms of chaotic dynamics. Experimental work (Wang *et al.*, Sci. Rep. 5, 8128 (2015)) found that avalanches in a rotating drum behave consistently with this description. We employ computer simulations to examine the chaotic dynamics accompanying granular avalanches in the rotating-drum system. These simulations directly evolve imposed perturbations and provide access to the largest short-time Lyapunov exponent. We find that the local chaotic properties of the system and its dynamics are indeed coupled; the system becomes chaotic as avalanches develop, and returns to a non-chaotic state as avalanches decay. Interestingly, the transition between chaotic and non-chaotic regimes lags behind the change in avalanche state. This contrasts with prior work on the shear cell, where the same force model yielded dynamics that becomes chaotic *leading up to*, rather than lagging behind, local reorganizations of disks.

Trabajo computacional reciente (Banigan y *col.*, Nat. Phys. 9, 288 (2013)) ha demostrado que el “jamming” y “unjamming” en una celda de cizalladura puede ser descrito en términos de dinámica caótica. Se ha encontrado experimentalmente (Wang y *col.*,Sci. Rep. 5, 8128 (2015)) que las avalanchas en un tabor rotatorio se comportan consistentemente con esta descripción. Utilizamos simulaciones computacionales para examinar la dinámica caótica que acompaña a las avalanchas granulares en el sistema de tambor rotatorio. Estas simulaciones involucran directamente perturbaciones impuestas, y permiten acceder al exponente más grande de Lyapunov de corto tiempo. Encontramos que las propiedades caóticas locales del sistema y su dinámica están, de hecho, acopladas; el sistema se vuelve caótico cuando se desarrollan las avalanchas, y retorna al estado no-caótico cuando éstas disminuyen. Resulta interesante que la transición entre los regímenes caótico y no-caótico va detrás del cambio del régimen de avalanchas. Esto contrasta con trabajos previos en la celda de cizalladura, donde el mismo modelo de fuerza resulta en una dinámica caótica que conduce, en vez de ser el resultado, a reorganizaciones locales de los discos.

PACS: 05.45.Pq Numerical simulations of chaotic systems, 45.70.Ht Avalanches, 45.70.Mg Granular flow: mixing, segregation and stratification, 05.45.-a Nonlinear dynamics and chaos

I INTRODUCTION

The ubiquity of granular materials—from pharmaceutical [1, 2] and semiconductor [1] industries to geology and astrophysics—has fueled over a century of research, mainly in industry-related communities [3,4]. Motivated by a desire to understand the physics of this complex class of materials, a wider theoretical perspective has emerged in the past few decades [5–9]. Of particular interest is the *jamming transition*, wherein a minute increase in the packing density drives a system from a liquid-like to a rigid state. This transition plays a central role in many promising new fields, including soft robotics and nanomanufacturing [10–12]. It also provides an ideal context for studying dissipative, non-equilibrium processes consequential to the understanding of life [13] and for fundamental research into non-equilibrium statistical mechanics [14, 15]. Yet, despite a flurry of research in the late 1990s and early 2000s following seminal work by Liu and Nagel [16], the jamming transition continues to elude a concrete, general explanation. In fact, studies have uncovered a splattering of different jamming regimes within a very narrow window of packing densities, including jammed [16], marginally jammed [17], shear-jammed [18], and fragile states [19] among others. This complexity makes a general, unifying perspective all the more desirable.

Recent computational work [20] has suggested that jamming may be understood more generally from an unexpected perspective. For a system of frictional disks in a two-dimensional (2D) shear cell a transition was observed from a chaotic to a non-chaotic state upon increase of the packing fraction. In the thermodynamic limit this transition, as characterized by a sign change of the largest global Lyapunov exponent, was found to coincide with the widely studied jamming transition of frictionless 2D disks [21]. Moreover, the largest *local* Lyapunov exponent $\lambda(t)$ was found to provide interesting information on the short-time dynamics of this system, temporarily becoming positive during the local reorganizations of disks. A corollary of this observation is that $\lambda(t)$ and its associated Lyapunov vector may be used as a predictive tool for such events [13,20], with potentially important applications ranging from geology to materials design [11].

This new perspective on the jamming transition, while promising both as a characterization tool and as a source of insight, must be explored for systems other than the 2D shear cell. Here, we aim to extend the methods of Ref. [20] to avalanches in a 2D rotating drum. Slip events in a shear cell are analogous to the onset of avalanches in the rotating drum. Experimental quantification of chaotic properties during the jamming transition has proven to be particularly challenging for this system [22]. Thus, our work offers the additional benefit of guiding future experimental studies. By employing the same interaction model as Ref. [20] we test to which extent the connection between dynamic behavior and chaotic properties carries over to systems other than the 2D shear cell. We find that the observations for the shear cell indeed apply to a larger class of granular systems, but also observe remarkable differences.

II MODEL AND METHODS

II.1 Physical Model

We perform quasi-2D molecular dynamics (MD) simulations of a 1:1 bidisperse collection of cylindrical disks inside a rotating drum and subject to a gravitational field $\mathbf{g}$, following an experimental study [22]. Although physical disks will deform under the stress of contacts, for computational efficiency we treat our disks as rigid cylinders and employ a linear spring–dashpot model (Fig. 1) [23–25]. For two contacting disks i and j with respective diameters d_i and d_j, the force $\mathbf{f}_{ij}$ on disk i by disk j contains both tangential and normal components and is described by

$$\mathbf{f}_{ij} = \begin{cases} \mathbf{f}^{\rm n}_{ij} + \mathbf{f}^{\rm t}_{ij} = \left(-k_{\rm n}\delta\hat{\mathbf{r}}_{ij} - \gamma_{\rm n}\mathbf{v}^{\rm n}_{ij}\right) - \min\left(\gamma_{\rm t} v^{\rm t}_{ij}, \mu f^{\rm n}_{ij}\right)\hat{\mathbf{v}}^{\rm t}_{ij} & \delta \le 0 \\ 0 & \delta > 0 \end{cases} \tag{1}$$

where $k_{\rm n}$ is an elastic constant, $\gamma_{\rm n}$ and $\gamma_{\rm t}$ are normal and tangential viscous coefficients, $\mathbf{r}_{ij} \equiv r_{ij}\hat{\mathbf{r}}_{ij} = \mathbf{r}_i - \mathbf{r}_j$ is the vector from disk j to disk i, $\delta = r_{ij} - \frac{1}{2}\left(d_i + d_j\right)$ is the (negative) overlap distance, and $\mathbf{v}_{ij}$ is the relative velocity with normal component $\mathbf{v}^{\rm n}_{ij} = \mathbf{v}_{ij} \cdot \hat{\mathbf{r}}_{ij}$ and tangential component $\mathbf{v}^{\rm t}_{ij} \equiv v^{\rm t}_{ij}\hat{\mathbf{v}}^{\rm t}_{ij} = \mathbf{v}_{ij} - \mathbf{v}^{\rm n}_{ij}$. The simplest choice for the tangential frictional term would be Coulomb friction, $\mathbf{f}^{\rm t}_{ij} = -\mu f^{\rm n}_{ij}\hat{\mathbf{v}}^{\rm t}_{ij}$, but this results in an ill-defined force at $v^{\rm t}_{ij} = 0$ [26]. To circumvent the discontinuity of this force model, we introduce a dissipative frictional force which crosses over to Coulomb friction above a threshold value of $v^{\rm t}_{ij}$ determined by μ [23–26].

Since Eq. (1) is a contact force (*i.e.*, non-zero only when $\delta \le 0$), the net force on a disk i is $m_i\mathbf{g} + \sum_j \mathbf{f}_{ij}$, where the sum runs over all contacting disks j. We note that the parameters $k_{\rm n}$, $\gamma_{\rm n}$, and $\gamma_{\rm t}$ are material-dependent. Specifically, $k_{\rm n}$ and $\gamma_{\rm n}$ determine the stiffness of the material and its coefficient of restitution. However, $\gamma_{\rm t}$ is not derivable from material properties and must be chosen empirically [25]. The mass m_i of the disks is given by their effective height h. Table 1 summarizes the parameters used in our simulations to model a system of photoelastic disks [22–24].

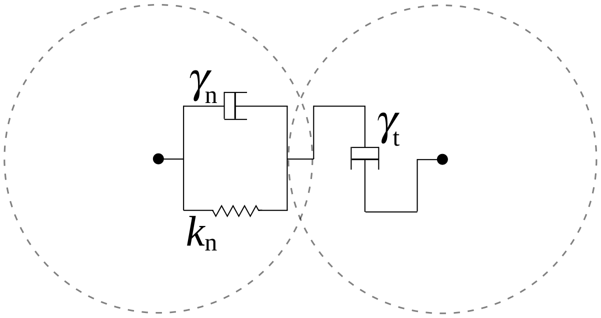

Figure 1. Linear spring–dashpot model for granular interactions. Two disks in contact experience a normal force that contains both elastic and dissipative contributions. The tangential (frictional) force is purely dissipative at small velocities and crosses over to Coulomb friction at larger velocities. See Eq. (1) of the main text.

Table 1. Physical parameters of the model in SI and reduced units. Reduced units are obtained by choosing the diameter and mass of a small disk as the unit length and mass, respectively, and adopting as energy unit the gain in potential energy of moving a small disk against gravity by a distance equal to its diameter.

Parameter	Symbol	SI units	Reduced units
Small disk diameter	$d_{\rm s}$	$1.2000{\times}10^{-2}$ m	1
Large disk diameter	$d_{\rm l}$	$1.4000{\times}10^{-2}$ m	1.1667
Wall disk diameter	$d_{\rm w}$	$1.6615{\times}10^{-2}$ m	1.3846
Disk height	h	$6.3500{\times}10^{-3}$ m	0.52917
Drum diameter	$d_{\rm drum}$	$7.9339{\times}10^{-1}$ m	66.115
Mass density	ρ	1060.0 kg/m^3	2.4061
Normal elastic coeff.	$k_{\rm n}$	352.1 N/m	565.97
Normal viscous coeff.	$\gamma_{\rm n}$	0.19 kg/s	8.7308
Tang. viscous coeff.	$\gamma_{\rm t}$	0.15 kg/s	6.8927
Coeff. of friction	μ	0.44	-
Number of wall disks	n	150	-
Number of other disks	N	736	-

II.2 Simulation Method

We use the velocity-Verlet algorithm [27] to integrate our equations of motion. For computational efficiency, we construct pairwise Verlet neighbor lists [27] and take advantage of Newton's Third Law in computing the interparticle forces. To ensure that the step size Δt is sufficiently small, we choose Δt such that $\Delta t \le \tau/40$, where τ is the characteristic contact time between two disks [23]. Since $\mathbf{f}^{\rm n}_{ij}$ describes a damped harmonic oscillator with frequency $\omega = \sqrt{k_{\rm n}/m_{ij} - \gamma_{\rm n}^2/(4m_{ij}^2)}$, where $m_{ij} = m_i m_j/\left(m_i + m_j\right)$ is the effective mass, the contact time follows as $\tau = \pi/\omega$. The smallest value of τ occurs for contact between two small disks, and our choice $\Delta t = 4 \times 10^{-5}$ s yields $\Delta t \approx \tau/82$ for such contacts.

The drum is created by placing n wall disks on the vertices of a regular n-gon with side length $d_{\rm w}$ and is set into rotation with a fixed period $T = 900$ s. We place the N non-wall disks randomly inside the drum and allow them to fall to the bottom due to the background gravitational field (Fig. 2(a)). Due to the drum's slow rotation rate and the lack of static friction in Eq. (1), we do not observe the build-up of large angles of inclination of the granular pile. Rather, once an avalanche begins, it advances continuously as long as the drum rotates. To study both onset and decay of avalanches, we simulate these two regimes separately and for each we obtain averages over many runs. We compute the system's global speed $V(t) = \sqrt{\sum_i |\mathbf{v}_i(t)|^2}$ (where the sum runs over all disks and $\mathbf{v}_i(t)$ is the velocity of disk i at time t) at each time step to determine when an avalanche occurs. To study the avalanche *onset* (Fig. 2(b)), we begin collecting data after a brief equilibration period, corresponding to one degree of rotation, so before the avalanche has started. The onset is then defined as the point where $V(t)$ begins to increase (cf. Fig. 3 below). To simulate avalanche *decay* we first allow the drum to rotate long enough to ensure the production of a continuous avalanche. We then begin collecting data for 5 seconds before abruptly stopping the drum, triggering a decay in $V(t)$ (cf. Fig. 4). By our definition, this decay in $V(t)$ also marks the beginning of the avalanche decay.

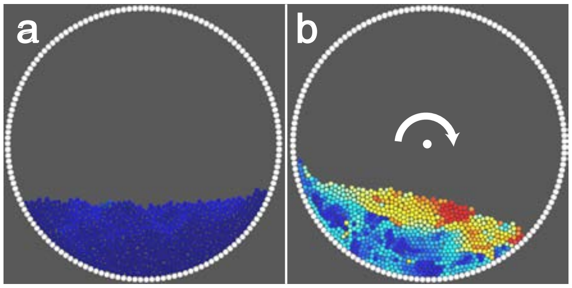

Figure 2. Snapshots from a simulation showing (a) the initial state of the system before the onset of an avalanche and (b) an avalanche resulting from the clockwise rotation of the drum. Disks are color-coded according to their speed, from blue (slow) to red (fast).

II.3 Quantifying Chaotic Dynamics

The chaoticity of a d-dimensional dynamical system may be quantified by a set of d Lyapunov vectors—which comprise an orthogonal set in phase space—and their corresponding exponents [28, 29]. Sorted by decreasing value, these exponents describe the exponential growth rates of perturbations along the directions in phase space described by the corresponding Lyapunov vectors. In this paper, we quantify the *locally* (*i.e.*, in the short term) most chaotic mode of our system via the first local Lyapunov vector $\mathbf{y}(t)$ and its corresponding local Lyapunov exponent $\lambda(t)$. We emphasize that these quantities are dynamics and describe only the short-time chaoticity of the system. The most unstable direction in phase space at one time is not necessarily so at future times, and $\lambda(t)$ is likewise subject to change [28, 29]. For a 2D system with N disks, we define a $4N$-dimensional perturbation vector $\boldsymbol{\delta}\mathbf{u}(t) \equiv (\{\boldsymbol{\delta}\mathbf{r}_i(t)\}, \{\boldsymbol{\delta}\mathbf{v}_i(t)\})$, which consists of two components describing positional perturbations δx_i and δy_i and two components describing velocity perturbations $\delta v_{x,i}$ and $\delta v_{y,i}$ for each disk i. From our equations of motion we derive a set of linearized tangent-space equations governing the evolution of the perturbation $\boldsymbol{\delta}\mathbf{u}(t)$. During the MD simulation, we integrate these equations in conjunction with the standard equations of motion for the disks, and thus simultaneously compute the real-space dynamics of the system and its chaotic properties. A detailed account of the numerical methods—as well as details of the analysis of *global* chaotic properties of granular systems—is provided in Ref. [30].

In general, a random initial perturbation quickly aligns with $\mathbf{y}(t)$, which also ensures that its growth rate converges to that of $\mathbf{y}(t)$ [28, 29]. We evolve $\boldsymbol{\delta}\mathbf{u}(t)$ and compute its exponential rate of growth (or decay) between successive time steps as $\lambda(t) = (1/\Delta t)\ln(|\boldsymbol{\delta}\mathbf{u}(t)|/|\boldsymbol{\delta}\mathbf{u}(t-\Delta t)|)$. The first (global) Lyapunov exponent would be obtained by taking the limit $\Delta t \to \infty$ [28]. By definition [28, 29], chaotic systems possess at least one positive Lyapunov exponent, whereas non-chaotic systems have only negative exponents.

We are interested in quantifying the *local*, rather than the global, chaoticity of our system, and we do so by computing $\lambda(t)$ during the evolution of an avalanche. For each run, we evolve a single perturbation vector, which is initialized by setting, on average, 10 percent of its components to non-zero values. Both the components and their values are chosen from a uniform random distribution. We compute the exponential growth rate of the perturbation vector at each time step. To focus on the chaotic properties of the disks that make up the contact network, at each time step we identify "rattler" disks with only zero or one contacts and exclude the corresponding components of the perturbation vector from growth-rate calculations during that step [30]. To achieve good statistics, we average over more than 70,000 pairs of avalanche onsets and decays, started from different random initial configurations.

III RESULTS AND DISCUSSION

We begin by investigating the evolution of $\lambda(t)$ during the onset of an avalanche. Even after averaging over many thousands of runs, $\lambda(t)$ exhibits a high level of noise (Fig. 3, blue points). This is to be expected since the dynamics near and along a chaotic attractor often varies quickly and dramatically [28, 29]. By taking the moving average

$$\overline{\lambda}(t) = \frac{1}{2q+1}\sum_{k=-q}^{q} \lambda(t + k\Delta t)\ , \tag{2}$$

with a narrow window $[t - q\Delta t, t + q\Delta t]$, we find that the data converge to a smoothly varying average behavior (Fig. 3, light blue dashed line). We choose a moving average width $(2q + 1)\Delta t = 0.5$ s, but even a window five times narrower does not change the results appreciably. We also filter the original data using a low-pass filter (keeping only the lowest 0.008 percent of frequencies) and find that the resulting low-frequency modes of the data closely trace the moving-average behavior. The moving average $\overline{\lambda}(t)$ reveals a sign change as the avalanche progresses, in qualitative agreement with the observations in Ref. [20], where the non-avalanching regime is associated with a negative local Lyapunov exponent that crosses over to a positive value after the avalanche begins.

For a more quantitative analysis, we must determine the onset of the avalanche as well as the time at which $\overline{\lambda}(t)$

changes sign. Assuming a linear fit (Fig. 3, orange line segment) to $\lambda(t)$ for $10\,s < t < 20\,s$, we locate the sign change of the local Lyapunov exponent at $t = 14.5 \pm 0.2 s$. We note that this fit agrees both with $\overline{\lambda}(t)$ and with the low-pass filtered data of $\lambda(t)$ within the error of the fit. The global speed $V(t)$ exhibits non-monotonic behavior immediately after $t = 0$ s, due to decay of "start-up" effects of the rotation of the drum, followed by the onset of the avalanche. Fitting a quadratic time dependence to $V(t)$ for $1\,s < t < 4\,s$, we determine the minimum as the beginning of the avalanche, taking place at $t = 2.628 \pm 0.002\,s$. Thus, there is a significant time lag between the avalanche onset and the change in sign of $\overline{\lambda}(t)$.

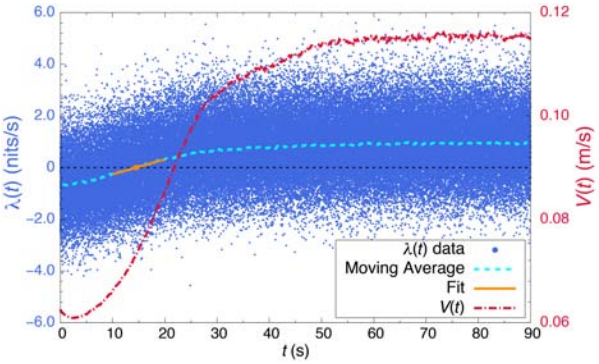

Figure 3. Chaotic behavior at avalanche onset. Scattered points represent the local Lyapunov exponent $\lambda(t)$ averaged over 70,000 independent runs. Even those data exhibit significant noise, which disappears in the moving average $\overline{\lambda}(t)$ (cf. main text). The latter exhibits a clear sign change (orange line segment) as the avalanche progresses, signaling the crossover from non-chaotic to chaotic behavior. To correlate this behavior with the dynamics of the system, the global speed $V(t)$ of all disks is shown as well (red dash–dotted line).

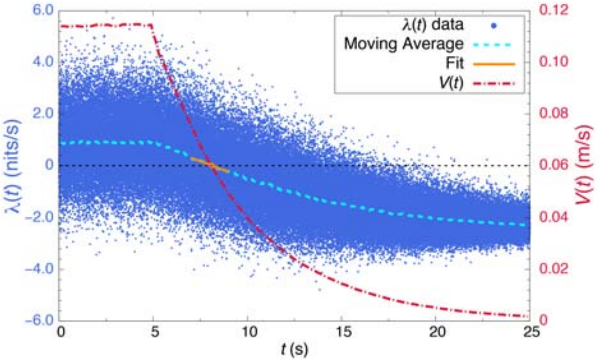

Figure 4. Dynamics at avalanche decay. Symbols are as described in Fig. 3. Following a continuous avalanche, avalanche decay starts at $t = 5\,s$, when the global speed $V(t)$ starts to decrease. This is accompanied by an immediate decrease in the moving average $\overline{\lambda}(t)$ of the first Lyapunov exponent, but a sign change in this exponent occurs only near $t = 8.13\,s$.

It is then natural to expect that the decay of the avalanche is accompanied by a second sign reversal of the local Lyapunov exponent. This is confirmed by the moving average $\overline{\lambda}(t)$ in Fig. 4. Adopting again a linear fit to $\lambda(t)$, now for $7\,s < t < 9\,s$, we determine the sign change at $t = 8.13 \pm 0.04\,s$. Since the decay of the avalanche is initiated exactly at $t = 5\,s$, we observe that the sign change of $\overline{\lambda}(t)$ again trails the change in state of the avalanche, although the lag is smaller than for the onset of the avalanche.

The time lag between the change in avalanche state and the change in sign of $\overline{\lambda}(t)$, both during avalanche onset and during avalanche decay, implies interesting conclusions regarding the dynamics of the rotating-drum system and its chaotic properties. On the one hand, it is noteworthy that even after the avalanche has started, the local dynamics of the system remain non-chaotic for some time. Conversely, even after the avalanche has started to decay, the local dynamics remain chaotic for a brief period. This is in contrast with the 2D shear cell [20], where the build-up of stress prior to an avalanche is accompanied by a gradual increase in the local exponent, which becomes positive well *before* the avalanche. On the other hand, despite the lag in the sign change, $\overline{\lambda}(t)$ shows an immediate response even for the rotating-drum system, starting to increase as soon as the avalanche is initiated (and likewise starting to decrease as soon as the avalanche decay begins). We remark that higher rotation speeds were found to decrease the time lag during avalanche onset [30]. Lastly, we note that the lack of static friction in our force model precludes direct comparison with an experimental study of the 2D rotating drum [22], where an immediate change in sign of $\lambda(t)$ was observed upon changes in the state of the avalanche. Due to experimental constraints, however, the authors in that study adopted different definitions of the Lyapunov vector for each avalanche regime, and we aim to overcome this drawback in future computational studies where we incorporate static friction.

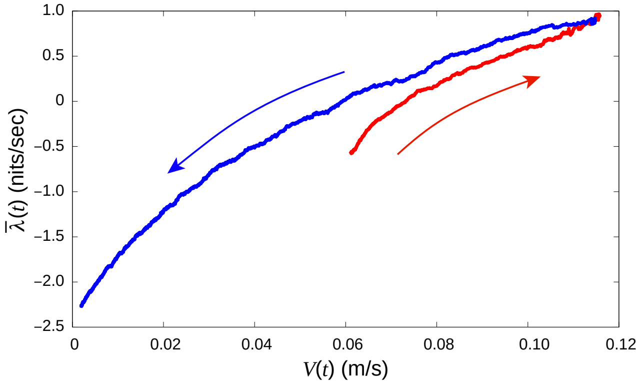

Figure 5. Correlation between the global speed $V(t)$ and the moving average $\overline{\lambda}(t)$ of the largest local Lyapunov exponent during avalanche onset (red) and decay (blue). Arrows indicate the direction of time evolution.

To elucidate the connection between the dynamics and chaotic properties of this system, we examine the global speed $V(t)$. Specifically, Fig. 5 shows how $\overline{\lambda}(t)$ has a monotonic dependence on $V(t)$ during both avalanche onset and decay. This is consistent with the strong spatiotemporal correlation between the velocity of each disk and the magnitude of the corresponding components of the Lyapunov vector in the 2D shear cell [20]. Here, we present a plausibility argument for this correlation by considering the dynamics of the individual particles in an avalanche. Indeed, it is known that the dynamics of a mobile disk bounded by a non-smooth (e.g., studded) cell is highly chaotic [31]. Similarly, we can think of each disk in the pile in Fig. 2(b) as bounded by a non-smooth cell comprised of its nearest neighbors. If the majority of such cells are tight enough to effectively trap the contained disk in a near-stationary state, then there will be a lack of chaotic collisions and the overall dynamics of the system will be non-chaotic, consistent with the observation of negative Lyapunov exponents above the jamming transition [20]. On the other hand, if the system is in a state with many rattler disks that are frequently reflected by the "walls" of their respective cells, then we can expect more chaotic dynamics. In addition, the shifting and changing of the cells themselves would also contribute to increasingly divergent behavior [9]. In an avalanche, both conditions—rattler disks and shifting cells—are present. Particularly for a frictional system, the onset of an avalanche results in Reynolds dilatancy [32], leading to enlarged cells and more chaotic rattlers. Additionally, the mixing of the system during an avalanche leads to shifting and changing cells. This provides a heuristic basis for the close coupling of the system's global speed and its local Lyapunov exponent in both of the avalanche regimes.

IV SUMMARY AND CONCLUSION

We have examined chaotic dynamics near jamming and unjamming events of cylindrical disks in a rotating drum, motivated by recent experiments on a corresponding system and by computational work on disks in a 2D shear cell. Although we find that our system—unlike the shear cell—does not exhibit a positive local Lyapunov exponent prior to an unjamming event, we do confirm the strong correlation between global dynamics and chaotic properties. The largest local Lyapunov exponent shows an immediate response upon the onset or decay of an avalanche, and indeed becomes positive during an avalanche. We further confirm this correlation by demonstrating that this exponent has a monotonic dependence on the global speed of the disks and provide a plausibility argument for this observation.

We are currently extending these results to systematically examine the observed time lag between the onset of an avalanche and the sign change of the largest Lyapunov exponent, as a function of drum rotation speed. Moreover, in this future work we will incorporate static friction, which will make it possible to compare our findings to experimental studies of this system using photoelastic disks [22].

V ACKNOWLEDGMENTS

This research was supported by the U.S. National Science Foundation through Grant Nos. DMR-1121262 at the Materials Research Center of Northwestern University and DMR-1310211. We thank the Quest high-performance computing facility at Northwestern University for computational resources.

REFERENCES

[1] G. Metcalfe, T. Shinbrot, J. J. McCarthy and J. M. Ottino, Nature 374, 39 (1995).

[2] S. L. Conway, A. Lekhal, J. G. Khinast and B. J. Glasser, Chem. Eng. Sci. 60, 7091 (2005).

[3] D. E. Moran, J. Frankl. Inst. 199, 493 (1925).

[4] C. V. Givan, Eos, Trans. Am. Geophys. U. 15, 572 (1934).

[5] G. Baumann, I. M. Jánosi and D. E. Wolf, Phys. Rev. E 51, 1879 (1995).

[6] H. M. Jaeger, S. R. Nagel and R. P. Behringer, Rev. Mod. Phys. 68, 1259 (1996).

[7] A. Daerr and S. Douady, Nature 399, 241 (1999).

[8] I. S. Aranson and L. S. Tsimring, Rev. Mod. Phys. 78, 641 (2006).

[9] S. E. Cisar, J. M. Ottino and R. M. Lueptow, AIChE J 53, 1151 (2007).

[10] P. Richard, M. Nicodemi, R. Delannay, P. Ribière and D. Bideau, Nature Mater. 4, 121 (2005).

[11] H. M. Jaeger, Soft. Matt. 11, 12 (2015).

[12] S. C. Warren, O. Guney-Altay and B. A. Grzybowski, J. Phys. Chem. Lett. 3, 2103 (2012).

[13] T. Shinbrot, Nature Phys. 9, 263 (2013).

[14] S. Torquato, T. M. Truskett and P. G. Debenedetti, Phys. Rev. Lett. 84, 2064 (2000).

[15] A. Haji-Akbari, M. Engel, A. S. Keys, X. Zheng, R. G. Petschek, P. Palffy-Muhoray and S. C. Glotzer, Nature 462, 773 (2009).

[16] A. J. Liu and S. R. Nagel, Nature 396, 21 (1998).

[17] A. J. Liu and S. R. Nagel, Ann. Rev. Condens. Matt. Phys. 1, 347 (2010).

[18] D. Bi, J. Zhang, B. Chakraborty and R. P. Behringer, Nature 480, 355 (2011).

[19] M. E. Cates, J. P. Wittmer, J.-P. Bouchaud and P. Claudin, Phys. Rev. Lett. 81, 1841 (1998).

[20] E. J. Banigan, M. K. Illich, D. J. Stace-Naughton and D. A. Egolf, Nature Phys. 9, 288 (2013).

[21] C. S. O'Hern, S. A. Langer, A. J. Liu and S. R. Nagel, Phys. Rev. Lett. 88, 075507 (2002).

[22] Z. Wang and J. Zhang, Sci. Rep. 5, 8128 (2015).

[23] S. Schöllmann, Phys. Rev. E 59, 889 (1999).

[24] M. Lätzel, S. Luding and H. J. Herrmann, Gran. Matt. 2, 123 (2000).

[25] T. Pöschel and T. Schwager, *Computational Granular Dynamics: Models and Algorithms* (Springer, Berlin, 2005).

[26] J. Schäfer, S. Dippel and D. E. Wolf, J Phys I (France) 6, 5 (1996).

[27] M. P. Allen and D. J. Tildesley, *Computer Simulation of Liquids* (Clarendon, Oxford, 1987).

[28] A. H. Nayfeh and B. Balachandran, *Applied Nonlinear Dynamics: Analytical, Computational and Experimental Methods* (John Wiley, New York, 1995).

[29] E. Ott, *Chaos in Dynamical Systems* 2^{nd} edition (Cambridge University Press, Cambridge, 2002).

[30] H. Maghsoodi and E. Luijten (2016). In preparation.

[31] J. M. Haile, *Molecular Dynamics Simulation: Elementary Methods* (Wiley, New York, 1992).

[32] O. Pouliquen and N. Renaut, J Phys II (France) 6, 923 (1996).

Rev. Cub. Fis. **33**, 55 (2016) ARTÍCULOS ORIGINALES

A GRANULAR EXPERIMENT APPROACH TO EARTHQUAKES

TERREMOTOS A TRAVÉS DE UN EXPERIMENTO CON GRANOS

S. Lherminier[a†], R. Planet[a], G. Simon[a], K.J. Måløy[b], L. Vanel[a], O. Ramos[a]

a) Institut Lumière Matière, UMR5306 Université Lyon 1-CNRS, Université de Lyon, 69622 Villeurbanne, France; sebastien.lherminier@univ-lyon1.fr†
b) Department of Physics, University of Oslo, P. O. Box 1048, 0316 Oslo, Norway
† corresponding author

Recibido 19/3/2015; Aceptado 19/4/2016

Although earthquakes have been scientifically studied for more than a century, essential questions as the possibility of predicting catastrophic events remain still open. Here we introduce an original experimental setup that mimics the behavior of a tectonic fault. By continuously shearing a granular layer under confined pressure, we are able to obtain a dynamics ruled by scale-invariant avalanches. We monitor the sizes of these avalanches by two methods and both show a power-law distribution (similar to the Gutenberg-Richter law). There is also a strong resemblance between waiting times distribution in our experiment and other studies with real earthquakes data.

Aunque los terremotos han sido estudiados científicamente durante más de un siglo, preguntas esenciales como la posibilidad de predecir eventos catastróficos permanecen todavía por resolver. Aquí introducimos un sistema experimental original que imita el comportamiento de una falla tectónica. Mediante el cizalle continuo de una capa granular sometida a una presión de confinamiento, somos capaces de obtener una dinámica de avalanchas invariantes de escala. Supervisamos los tamaños de estas avalanchas por dos métodos y ambos muestran una distribución en ley de potencia (similar a la ley de Gutenberg-Richter). Hay también una gran similitud entre la distribución de tiempos que espera entre eventos obtenidos en nuestro experimento y otros estudios con datos de terremotos reales.

PACS: Granular systems, 45.70.-n; avalanches, 45.70.Ht; earthquakes, 91.30.Px

I. INTRODUCTION

Most earthquakes occur at fault zones, where friction between two tectonic plates colliding or sliding against each other causes a stick-slip-like movement. During stick states, energy is stored as deformations in the rocks around the fault zone. Once the accumulated stress is enough to break through the asperities of the plates [1], the stored energy is released by unlocking of the fault: during a brief moment, the relative velocity of the plates is very high, until it locks again, generating an earthquake. In the case of large earthquakes, the consequences on human society can be catastrophic [2].

Earthquakes are classified by their size, using the well-known magnitude M, linked to the energy E of the earthquake by the relation $M = 2/3\ \log(E) + K$, where K is a constant. The probability distribution of a series of earthquakes sorted by their energy is given by a power-law $P(E) \sim E^{-b}$ with an exponent $b = 5/3 = 1.66$, known as the Gutenberg-Richter (GR) law [3, 4]. This kind of behavior where sudden events have sizes distributed following a power law is called scale-invariance avalanches, and is rather common in nature. Scale-invariance avalanches have been reported in phenomena as diverse as snow avalanches [5], granular piles [6–10], solar flares [11, 12], superconducting vortices [13], sub-critical fracture [14, 15], evolution of species [16] and even stock market crashes [17, 18].

Even if considerable work has been done to understand the earthquakes dynamics — mainly from the Geophysical community but also from the general perspective of scale-invariant avalanches [19–23] — many issues remain as open questions, and the essential fact about the possibility of predicting catastrophic quakes is still a subject of debate [22, 24].

In order to bring some answers to different open questions about earthquakes and scale-invariant phenomena in general, we present an original experimental setup that reproduces the behavior of a tectonic fault.

A fault is a planar fracture at the frontier between two plates, defining the direction of motion. The material physically separating the two plates is called the fault gouge and is composed of crushed rocks from the friction and wear between the two plates. The typical way of modeling the gouge is by using disks or spheres [25, 26], as a mean to reduce complexity.

As of today, the best attempts to reproduce the dynamics of earthquakes comes from friction or fracture experiments. Overcoming the static friction between two solid blocks under a controlled load [27, 28] is maybe the simplest example. In this case the study generally focuses on one single event. Other experiments have sheared a granular layer, trying to simulate the behavior of a tectonic fault. However, it has been difficult to obtain a distribution of events that resembles the Gutenberg-Richer law [3]. Sometimes because the intrinsic response of the system is a regular stick-slip with all "earthquakes" having approximately the same size [29] and sometimes because insufficient statistical sets of data [30, 31]: most of the recent shear experiments have a linear geometry. Consequently, the relative motion between the two sliders is limited to a fraction of the length of the system, which is responsible for the insufficient data collection. In the case of fracture, analogous to both the GR and Omori law have been observed in subcritical fracture experiments [15,32]. However, fracture is by nature a non-stationary process and the characteristics of the system change as it accelerates towards total failure.

To go beyond these current limitations, an original setup has been built. It uses a 2D granular material to model the fault gouge, mainly responsible for the dynamics of a fault. The gouge is sheared between two rough surfaces at a constant and very low speed. Thanks to periodic boundary conditions, we have access to rich statistics and have been able to produce scale-invariant avalanches. This paper presents a few preliminary results of this laboratory "earthquake machine".

II. EXPERIMENTAL SETUP

The experimental setup consists of two fixed, transparent, and concentric cylinders, with a gap between them, so that a monolayer of disks can be introduced into the gap (see Fig. 1). The disks have 4 *mm* thickness and 6.4 *mm* and 7.0 *mm* diameter (in equal proportion) to avoid crystallization.

They are made of Durus White 430 and have been generated in a Objet30 3D printer.

The translucent and photoelastic character of the grains allows the visualization of the stress inside the disks when placing the experimental setup between two circular polarizers (close-up in Fig. 1).

The Young's modulus of Durus material is $E \simeq 100$ *MPa*, which contrasts with the classical experiments using photoelastic disks with a Young's modulus $E = 4$ *MPa* [30, 31, 33–37]. Our grains can hold a much larger stress without a considerable deformation, which favors both the acoustic propagation and image analysis [38].

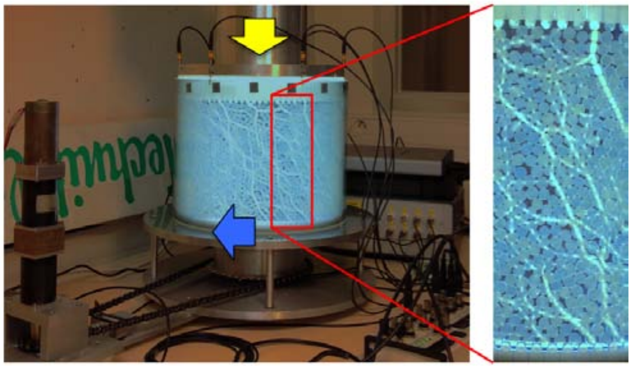

Figure 1. Experimental setup. The yellow and blue arrows represent the confining force and the shear direction respectively. (close-up) The birefringent nature of the material of the disks allows visualization of the internal force chains in the granular material

Two rings containing "fixed grains" constrain the pack from upper and bottom boundaries. The yellow arrow in Fig. 1 indicate the force between the plates, fixed by a dead load of 35 *kg*. As the rings rotate in relation to each other (blue arrow in Fig. 1) at a constant and very low speed (7.6 *μm/s*, so 1 complete rotation every 36.7 hours), shear stresses build up on the packed beads.

The release of these stresses happens with sudden avalanches (*i.e.* reorganizations of the packing), and is also associated with acoustic emissions. In order to characterize the mechanical response of the sheared material we extract the resisting torque of the system using a steel lever and a force sensor Interface SML-900N (of range 900 *N*) sampled at 10 *Hz*. Acoustic measurements are performed using piezoelectric pinducers (VP-1.5 from CTS Valpey Corporation, sampled at 100 kHz) inserted in adjusted holes in the upper ring.

In this article we focus on the analysis of the resisting torque and the acoustic emissions.

III. RESULTS

The global mechanical response of the system shows a clear stick-slip-like behavior, since the measure of the resisting torque shows a continuous loading with intermittent drops of largely distributed sizes (see Fig. 2a). These drops are the signature of sudden global reorganizations of the pile, *i.e.* avalanches.

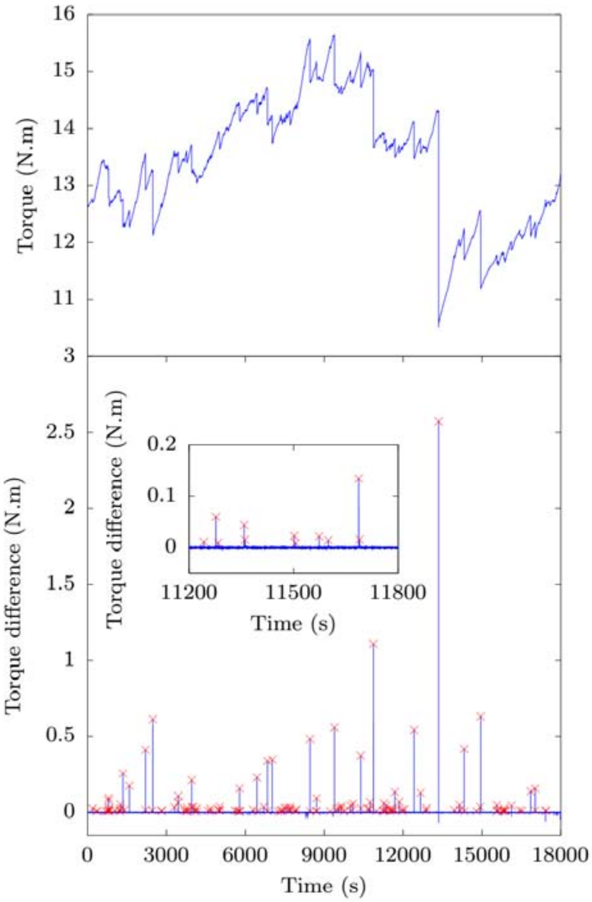

Figure 2. **(a)** Typical torque signal on a 5 hours time window. **(b)** Difference between two consecutive torque measurements shown in (a). Red crosses represent the detected events. The small events appear clearly when zooming (see the inset), even if they seemed invisible due to the large distribution of sizes.

The reorganization will begin with one grain exceeding its frictional threshold, moving, and thus releasing stress over its neighbors. The phenomenon will propagate along neighbors until all the grains are friction-locked, hence the name avalanche.

This stress release will manifest itself by a very brief decrease of the applied torque on the top boundary.

Since the mechanical response is regularly sampled, the size of the avalanche can be extracted from the difference of the torque signal between two consecutive time steps (see Fig. 2b).

Avalanches will appear as peaks high over of the noise. Since the amplitudes of the peaks are largely distributed (over a few decades), it is necessary to zoom in on a portion of the signal to distinguish the smallest peaks. Since the velocity of the moving ring is very small (in average one event every 200 seconds), it is necessary to wait for long times to acquire enough statistics (typically a few days long).

We can then extract the probability distribution of the events' sizes, shown on Fig. 3. The distribution follows a power-law for small sizes and reaches a cutoff at large ones (over 10 $N.m$). The cutoff regime has low statistics (around 2 % of the total), so a precise behavior is hard to obtain. The power-law regime is characterized by an exponent 1.67 ± 0.04 computed from maximum likelyhood method [39]. We here find a first similarity with real earthquakes by comparing this power-law regime with the GR law. However, we notice that here the exponent is computed for torque drops, where the GR law deals with energies of the earthquakes.

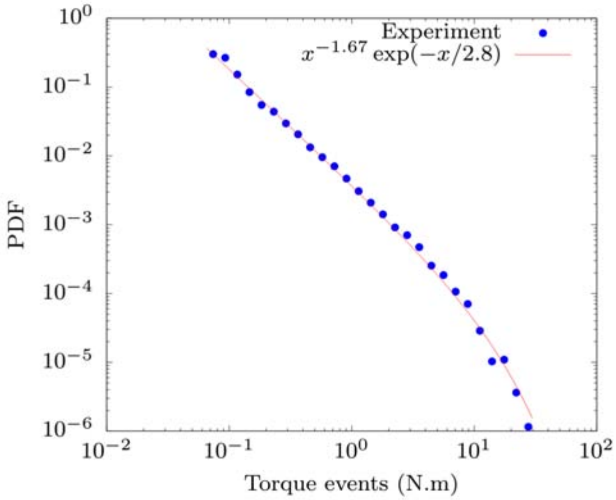

Figure 3. Avalanches size distribution from an 14 days experiment, representing ~ 10,000 events. We show the maximum likelyhood fit with an exponentially-truncated power-law.

From acoustic measurements we are able to extract the energy of acoustic emissions, computed as the spectral energy (sum of spectral amplitudes in the bandwidth from 0.5 to 15 kHz, which include all the frequencies that have been observed during acoustic events) of the signal on the detected duration of the event. We observe again that the energy probability distribution scales as a power-law (see Fig. 4) with an exponent 1.72 ± 0.04, again computed by maximum likelihood method. We are currently analyzing the relation between both measurements (torque and acoustics), as well as the influence of the frequency of measurement, which may be a cause of the different exponent values obtained in the experiment [15].

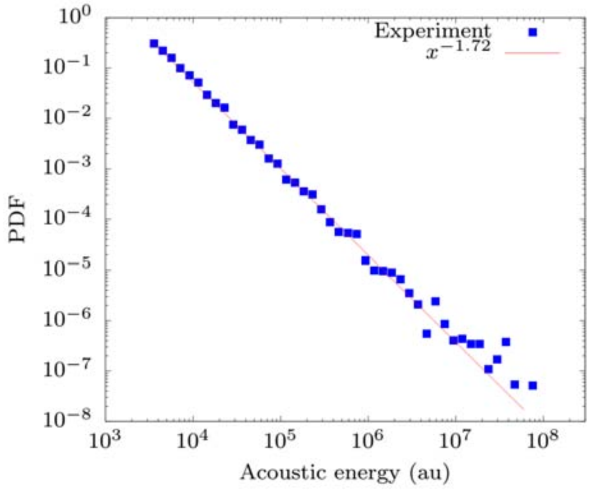

Figure 4. Acoustic energy distribution from a 1 day experiment, representing ~ 6,000 events. The maximum likelyhood fit with a power-law is also shown.

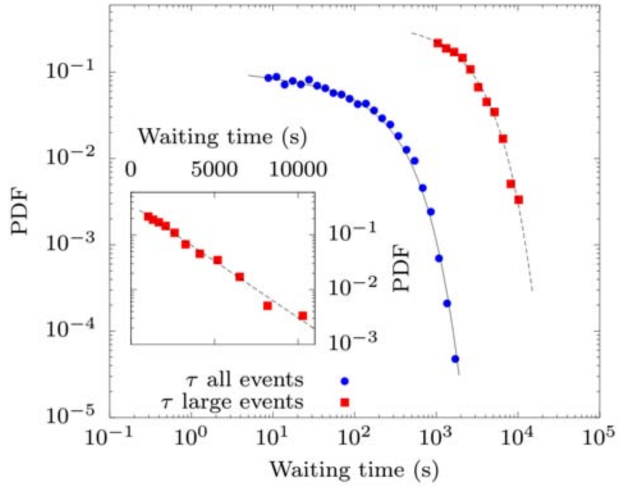

Figure 5. Waiting times probability distribution for the whole set of avalanches (●) with PDF shown in Fig. 3. The solid line (—) is a fit to the data of a generalized gamma distribution. The represented gamma distribution has the form $\tau^{-0.1}\exp(-\tau/256)$. The figure also shows the probability distribution (■) of waiting times for only large events (sizes greater than a tenth of the maximum event detected, representing ~ 5 % of the events). The dashed line (- -) is a fit to the data representing an exponential distribution characterized by $\exp(-\tau/2100)$. The inset shows the data for large events in semilog scale to highlight the exponential dependency.

A second characteristic of earthquakes is the distribution of waiting times between two events. We are able to compute these waiting times as well (see Fig. 5), both for the whole set of events and for only large ones (a large event has a size greater than a tenth of the maximum size, here 3 N.m). The behavior for the whole set of events is compatible with a generalized gamma function as found in [40]: the scaling extracted is of the form $\tau^{-\gamma}\exp(-\tau/\tau_0)$ with $\gamma = 0.10 \pm 0.02$ and $\tau_0 = 256 \pm 4$. If only the large events are taken into account, then an exponential behavior is obtained $\exp(-\tau/\tau_l)$ with $\tau_l = 2100 \pm 50$, which means we have a Poisson process with independent large events, which is also the case in real earthquakes.

IV. CONCLUSIONS

In this paper we have presented a laboratory "earthquake machine" that generates scale-invariant avalanches with similar behavior than real earthquakes, by modeling the dynamics of a fault zone with a sheared 2D granular medium. Both the global mechanical response and acoustic emissions are monitored and both show scale-invariant avalanches. The probability distribution of events' sizes are consistent with the Gutenberg-Richter law observed for real earthquakes. A study of waiting times between events is also consistent with behaviors observed by previous studies on real earthquakes.

We acknowledge financial support from AXA Research Fund.

REFERENCES

[1] M. Ohnaka, *The Physics of Rock Failure and Earthquakes* (Cambridge University Press, 1993).

[2] B. Bolt, *Earthquakes: Revised and Expanded* (W.H. Freeman and Company, New York, 1993).

[3] B. Gutenberg and C. F. Richter, Annali di Geofisica 9, 1 (1956).

[4] T. C. Hanks and H. Kanamori, Journal of Geophysical Research: Solid Earth 84, 2348 (1979).

[5] K. W. Birkeland and C. C. Landry, Geophysical Research Letters 29, 49 (2002).

[6] G. A. Held, D. H. Solina, H. Solina, D. T. Keane, W. J. Haag, P. M. Horn and G. Grinstein, Phys Rev Lett 65, 1120 (1990).

[7] V. Frette, K. Christensen, A. Malthe-Sørenssen, J. Feders, T. Jøssang and P. Meakin, Nature 379, 49 (1996).

[8] E. Altshuler, O. Ramos, C. Mart ́ ınez, L. E. Flores and C. Noda, Phys Rev Lett 86, 5490 (2001).

[9] C. M. Aegerter, K. A. L ̋ orincz, M. S. Welling and R. J. Wijngaarden, Phys Rev Lett 92, 058702 (2004).

[10] O. Ramos, E. Altshuler and K. J. Måløy, Phys Rev Lett 102, 078701 (2009).

[11] B. R. Dennis, Solar Physics 100, 465 (1985).

[12] D. Hamon, M. Nicodemi and H. J. Jensen, Astronomy and Astrophysics 387, 326 (2002).

[13] E. Altshuler and T. H. Johansen, Rev Mod Phys 76, 471 (2004).

[14] S. Santucci, L. Vanel and S. Ciliberto, Phys. Rev. Lett. 93, 095505 (2004).

[15] M. Stojanova, S. Santucci, L. Vanel and O. Ramos, Phys. Rev. Lett. 112, 115502 (2014).

[16] K. Sneppen, P. Bak, H. Flyvbjerg and M. H. Jensen, Proceedings of the National Academy of Sciences 92, 5209 (1995).

[17] Y. Lee, L. A. Nunes Amaral, D. Canning, M. Meyer and H. E. Stanley, Phys. Rev. Lett. 81, 3275 (1998).

[18] X. Gabaix, P. Gopikrishnan, V. Plerou and H. E. Stanley, Nature 423, 267 (2003).

[19] P. Bak, C. Tang and K. Wiesenfeld, Phys. Rev. Lett. 59, 381 (1987).

[20] P. Bak, *How Nature works-The Science of Self-organized Criticality* (Oxford Univ. Press, Oxford, (1997).

[21] H. J. Jensen, *Self-organized Criticality, Emergent Complex Behavior in Physical and Biological Systems* (Cambridge Univ. Press, Cambridge, 1998).

[22] I. Main, Nature (1999).

[23] O. Ramos, B. Veress and J. Szigethy, eds., Horizons in Earth Science Research. Vol. 3 (Nova Science Publishers, 2011).

[24] R. J. Geller, D. D. Jackson, Y. Y. Kagan and F. Mulargia, Science 275, 1616 (1997).

[25] F. Alonso-Marroqu ́ ın, I. Vardoulakis, H. J. Herrmann, D. Weatherley and P. Mora, Phys. Rev. E 74, 031306 (2006).

[26] S. Abe, S. Latham and P. Mora, Pure and applied geophysics 163, 1881 (2006), ISSN 0033-4553.

[27] O. Ben-David, G. Cohen and J. Fineberg, Science 330, 211 (2010).

[28] S. M. Rubinstein, G. Cohen and J. Fineberg, Phys. Rev. Lett. 98, 226103 (2007).

[29] P. A. Johnson, H. Savage, M. Knuth, J. Gombeg and C. Marone, Nature 451, 57 (2008).

[30] K. E. Daniels and N. W. Hayman, Journal of Geophysical Research: Solid Earth 113, 2156 (2008).

[31] D. M. Walker, A. Tordesillas, M. Small, R. P. Behringer and C. K. Tse, Chaos: An Interdisciplinary Journal of Nonlinear Science 24, 013132 (2014).

[32] J. Bar ́ o, A. Corral, X. Illa, A. Planes, E. K. H. Salje, W. Schranz, D. E. Soto-Parra and E. Vives, Phys. Rev. Lett. 110, 088702 (2013).

[33] B. Miller, C. O'Hern and R. P. Behringer, Phys. Rev. Lett. 77, 3110 (1996).

[34] D. Howell, R. P. Behringer and C. Veje, Phys. Rev. Lett. 82, 5241 (1999).

[35] T. S. Majmudar, M. Sperl, S. Luding and R. P. Behringer, Phys. Rev. Lett. 98, 058001 (2007).

[36] J. Zhang, T. S. Majmudar, M. Sperl and R. P. Behringer, Soft Matter 6, 2982 (2010).

[37] E. T. Owens and K. E. Daniels, Europhysics Letters 94, 54005 (2011).

[38] S. Lherminier, R. Planet, G. Simon, L. Vanel and O. Ramos, Phys. Rev. Lett. 113, 098001 (2014).

[39] A. Clauset, C. R. Shalizi and M. E. Newman, SIAM review 51, 661 (2009).

[40] A. Corral, Phys. Rev. Lett. 92, 108501 (2004).

Rev. Cub. Fis. **33**, 59 (2016) COMUNICACIONES ORIGINALES

SISTEMA EXPERIMENTAL PARA EL ESTUDIO DE LA HISTÉRESIS FERROELÉCTRICA EN CAPAS DELGADAS

EXPERIMENTAL SYSTEM FOR FERROELECTRIC HYSTERESIS ANALYSIS ON THIN FILMS

C. E. Moreno-Crespo, A. Pélaiz-Barranco†, Y. Méndez-González, A. Santana-Gil, F. Calderón-Piñar, Y. González-Abreu

Facultad de Física-Instituto de Ciencia y Tecnología de Materiales, Universidad de La Habana. San Lázaro y L, Vedado. La Habana 10400, Cuba; pelaiz@fisica.uh.cu†
† autor para la correspondencia

Recibido 9/12/2015; Aceptado 8/6/2016

PACS: Data acquisition: hardware and software 07.05.Hd, Computer interfaces 07.05.Wr, Hysteresis in ferroelectricity 77.80.Dj, Circuits electronic 07.50.Ek.

El estudio de las diferentes propiedades en los materiales ferroeléctricos presenta un gran interés en múltiples ramas científicas y de la industria [1,2]. Una de estas propiedades es la que los distingue del resto de los dieléctricos, ya que la dependencia de su polarización (P) con el campo eléctrico externo aplicado (E) se da en forma de un lazo, denominado "Lazo de Histéresis" (Figura 1), debido a la reversibilidad de la polarización [1]. Además, cada material ferroeléctrico posee un lazo de histéresis diferente, similar a lo que sucede con las huellas dactilares [3]. Por otra parte, el uso de capas delgadas ferroeléctricas ha atraído gran atención por su potencial aplicación en memorias ferroeléctricas no volátiles [4]. Estos sistemas ofrecen ventajas en comparación con los sistemas cerámicos en masivo para la producción de dispositivos para la microelectrónica [4].

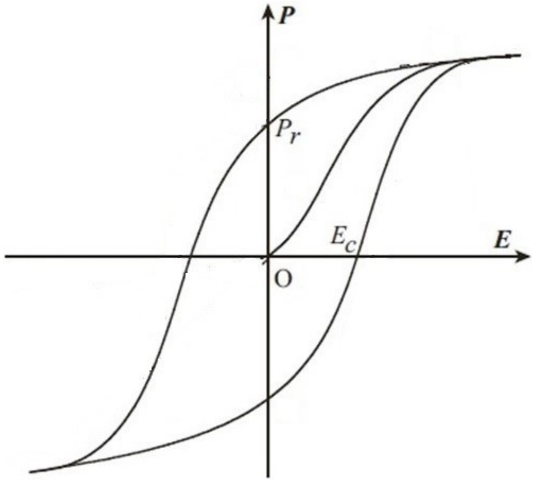

Figura 1. Lazo de histéresis para los materiales ferroeléctricos. Se indican los parámetros fundamentales P_r y E_C.

La forma más utilizada para la obtención de dichos lazos es mediante un montaje experimental conocido como: "Circuito Sawyer-Tower" [4]. A partir de este comportamiento se obtienen parámetros que caracterizan al material en cuestión, como la polarización remanente (P_r), que es la polarización que permanece en el material una vez retirado el campo eléctrico externo, y el campo coercitivo (E_C), que es el campo eléctrico necesario para invertir el sentido de la polarización en el material. Estos parámetros son los que definen el tipo de aplicación que se le dará a cada material en particular, por lo que su conocimiento es de gran importancia desde el punto de vista de las aplicaciones [5]. Por ejemplo, materiales con altos valores de P_r y bajos valores de E_C son requeridos principalmente en dispositivos de memoria [6]. Además, para capas delgadas ferroeléctricas los altos campos que deben ser aplicados para cambiar el estado de polarización, pueden ser obtenidas con bajos voltajes, haciendo a estas útiles para aplicaciones electrónicas.

En este trabajo tenemos como objetivo desarrollar un sistema que nos permita obtener lazos de histéresis en capas delgadas ferroeléctricas, con el fin de extraer sus parámetros fundamentales. Para ello contamos con una computadora con el programa *LabVIEW*, un osciloscopio de memoria *Tektronix*, una fuente de corriente alterna y los componentes electrónicos necesarios para construir un circuito Sawyer-Tower.

La Figura 2 muestra el llamado "Circuito Sawyer-Tower", utilizado frecuentemente para obtener el lazo de histéresis. La dependencia $P-E$ se obtiene de la siguiente manera. Por el canal 1 del osciloscopio se mide V_{FE} (diferencia de voltaje que hay entre las caras de la muestra ferroeléctrica en cuestión), la cual es proporcional al campo eléctrico aplicado sobre ella según la ecuación 1:

$$E = \frac{V_{FE}}{d}, \tag{1}$$

donde d es el espesor de la muestra.

Por el canal 2 del osciloscopio medimos V_C (diferencia de voltaje que hay entre las placas del capacitor de referencia), la cual es proporcional al desplazamiento del campo eléctrico (D) de la muestra según:

$$D = \frac{Q}{S} = \frac{D_{ref} V_C}{S}, \tag{2}$$

donde Q y C_{ref} son la carga y la capacidad, respectivamente, del capacitor patrón y S es el área de la sección transversal de la muestra. La muestra está conectada en serie con el capacitor de referencia, por lo que las cargas en cada uno de los elementos mencionados anteriormente se igualan, cumpliéndose:

$$Q = C_{ref}V_C = C_{FE}V_{FE}, \tag{3}$$

donde C_FE es la capacidad de la muestra.

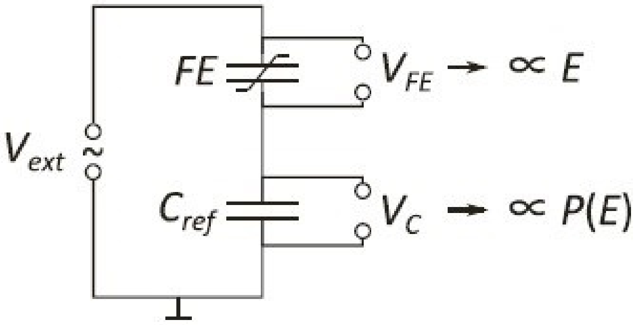

Figura 2. Esquema del circuito "Sawyer-Tower clásico", donde V_{ext} es el voltaje proporcionado por la fuente.

Se conoce que $D = \epsilon_o E + P$, siendo ϵ_o la permitividad dieléctrica del vacío. A partir de la igualdad anterior se puede hacer la aproximación $P \approx D$ para los sistemas ferroeléctricos, dado que por ejemplo: para un valor pequeño de $D = 10\ \mu C/cm^2$ y un valor grande de $E = 1\ MV/cm$, se obtiene un valor de $\epsilon_o E = 0.1\ \mu C/cm^2$ [4]. Por lo que se puede decir que:

$$P = \frac{C_{ref}V_C}{S}, \tag{4}$$

con un error del 1%.

Conocida la forma en que se pueden obtener los valores del campo eléctrico y la polarización, se procede a la transmisión de dichos valores desde el osciloscopio hacia una computadora.

Para la construcción del sistema experimental utilizamos una fuente de voltaje de $V_{max} = 24V$ ($60Hz$), además de un capacitor de referencia de 1 μF. Por otra parte, para la obtención de los datos a través de una computadora, se utilizó el programa *LabVIEW*. La Figura 3 muestra la interface que se diseñó para el manejo del usuario durante la adquisición de los datos.

En la Figura 4 se puede ver un esquema simplificado que muestra cómo funciona nuestro programa. Este se elaboró usando el estilo de programación conocido como "máquina de estados", ya que permite añadir estados y programar los códigos en la medida que se desarrolla el programa. Además, posibilita un control total sobre el flujo de la ejecución y garantiza un mínimo de operaciones a la vez.

Los datos de la medición son enviados por el osciloscopio luego que este recibe los comandos previamente programados, y son recogidos por cada canal de forma independiente, por lo que se logra con relativa facilidad guardar la medición en un documento de texto con dos columnas, una con los valores del campo eléctrico y la otra con los de polarización. Además, el nombre y la ubicación de este archivo pueden ser elegidas por el usuario.

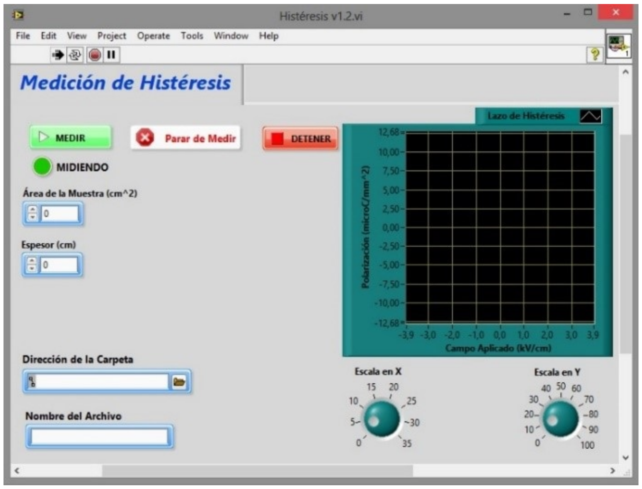

Área de la Muestra (cm^2) 0

Espesor (cm) 0

Figura 3. Panel frontal del programa elaborado en LabVIEW para la obtención y el graficado de los datos de histéresis.

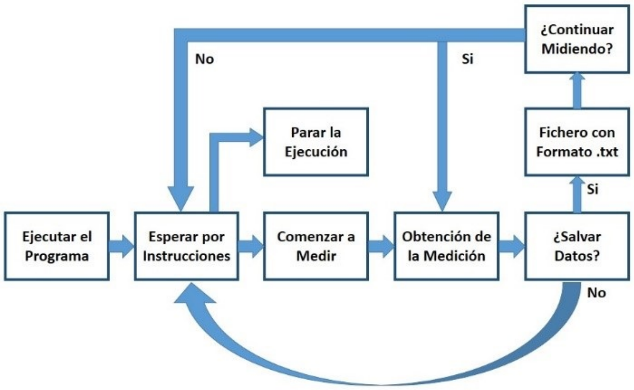

Figura 4. Diagrama de flujo que muestra el principio de funcionamiento del programa creado.

Este sistema permite realizar estudios en capas, en general, de cualquier espesor (desde los nm hasta las μm) y pueden medirse capas con pérdidas dieléctricas pequeñas. Para los parámetros finales, polarización y campo eléctrico, las incertidumbres son 1 $\mu C/cm^2$ y 10 kV/cm, respectivamente.

Finalmente se realizaron mediciones de lazos de histéresis en capas delgadas ferroeléctricas de la familia Aurivillius con vistas a validar el sistema experimental. La Figura 5 muestra una de las mediciones, como ejemplo. Los resultados para la polarización remanente y el campo coercitivo fueron, respectivamente, $P_r = 5\ \mu C/cm^2$ y $E_c = 180\ kV/cm$, para un campo máximo aplicado de aproximadamente 400 kV/cm. Reportes previos en capas del tipo $SrBi_2Ta_2O_9$ han mostrado polarizaciones remanentes de igual orden, para campos máximos aplicados de 600 kV/cm [7, 8], superiores a los que hemos aplicado a la capa estudiada con el sistema desarrollado.

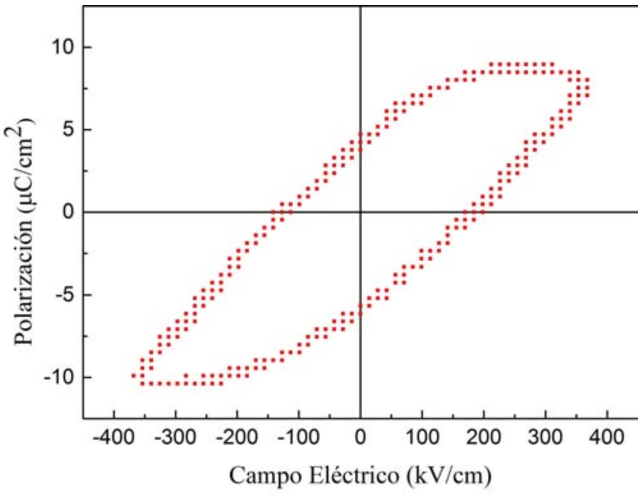

Figura 5. Lazo de histéresis en una capa delgada de la familia Aurivillius, correspondiente al sistema $Sr_{0.7}Ba_{0.3}Bi_2Nb_2O_9$.

En este trabajo se realizó el montaje de un sistema experimental que permite la medición de lazos de histéresis en capas delgadas ferroeléctricas, utilizando como elementos centrales un circuito "Sawyer-Tower" y un programa computacional acoplado a este. Se efectuaron mediciones en varias capas delgadas de la familia Aurivillius, mostrándose buenos resultados.

REFERENCES

[1] Y. Xu, *Ferroelectric Materials and Their Applications* (Elsevier Science Publishers B.V., The Netherlands, 1991).

[2] G. H. Haertling, J. Am. Ceram. Soc., 82 [4] 797-818 (1999).

[3] Li Jin, Fei Li, and Shujun Zhang, J. Am. Ceram. Soc., 97 [1] 1–27 (2014).

[4] T. Schenk, E. Yurchuk, S. Mueller, U. Schroeder, S. Starschich, U. Böttger, and T. Mikolajick, Appl. Phys. Rev.1, 041103 (2014).

[5] Xuefeng Chen, Xianlin Dong, Fei Cao, Junxia Wang, and Genshui Wang, J. Am. Ceram. Soc., 97 [1] 213-219 (2014).

[6] Daniela Cristina Manfroi Rodrigues, "Síntesis de capas delgadas del sistema PMN-PT por el método de precursores óxidos". Tesis de Maestría. Departamento de Física y Química, Universidad Estadual Paulista, Brasil, 2009.

[7] G. Yuan, J. Liu, Y. Wang, D. Wu, S. Zhang, Q. Shao, and Z. Liu, Appl. Phys. Lett., 84, 3352-3354 (2004).

[8] S. T. Zhang, W. J. Ji, L. Wang, L. Y. Ding, Y. F. Chen, and Z. G. Liu, Sol. Sta. Comm. 149, 434-437 (2009).

PHYTOPLANKTON PHOTOSYNTHETIC POTENTIAL IN COASTAL ZONES AROUND THE WORLD

POTENCIAL FOTOSINTÉTICO DEL FITOPLANCTON EN LA ZONA COSTERA MUNDIAL

D. Avila-Alonso[a], R. Cardenas[a†], L. Rodríguez[a] y J. Álvarez-Salgueiro[b]

a) Faculty of Mathematics, Physics and Computing Science, Universidad Central Marta Abreu de Las Villas, Cuba; rcardenas@uclv.edu.cu†
b) Faculty of Electromechanics, Universidad de Camagüey Ignacio Agramonte y Loynás, Cuba; jessica.alvarez@reduc.edu.cu
† corresponding author

Recibido 3/9/2015; Aceptado 8/1/2016

PACS: Coastal oceanography, 92.10.Sx; General theory of biological physics, 87.10.-e; Photosynthesis in oceanography, 92.20.Cm, *92.20.ch; Ultraviolet radiation effects on biological systems, 87.50.W-

I. INTRODUCTION

Solar electromagnetic radiation is the fundamental source of energy that drives Earth's climate and sustains life. Primary biological production of the biosphere depends on photosynthesis, which uses solar energy to transform water and carbon dioxide into organic compounds that store chemical energy. This process in aquatic ecosystems is mostly carried out by phytoplankton, unicellular organisms that move passively in the water column, and which play a pivotal role in global biogeochemical cycles and food web dynamics [1]. Solar electromagnetic radiation in the wavelength range 400–700 nm is responsible for the bulk of photosynthesis, and it is called photosynthetically active radiation (PAR). Ultraviolet radiation (UVR, 280−399 nm) is generally considered an inhibitor of the process. These energetic wavelengths affect cellular DNA, impair photosynthesis, enzyme activity and nitrogen incorporation, bleach cellular pigments and inhibit motility and orientation [2].

Climate change can alter the exposure of aquatic ecosystems to UVR by influencing the Earth system processes that affect ozone depletion as well as changes in aquatic UVR absorbing substances such as colored dissolved organic matter (CDOM). This one controls the penetration of UVR into water bodies, but it is photodegraded by solar UVR [3].

Given their global importance, coastal marine environments are a major focus of concern regarding the potential impacts of anthropogenic climate change [4]. Coastal zones vary tremendously in their optical properties and have a lower transparency than open ocean waters due to the runoff of silt and dissolved organic carbon from shores. On the other hand, there have been fewer studies of temperate and tropical coastal seas specifically, perhaps because the assumption has been made that ozone depletion is only a problem for polar seas, and that the ozone hole is an Antarctic problem [5].

The aim of this work is to do a quantitative assessment of the phytoplankton photosynthetic potential in coastal zones around the world, using a (generic) optical classification of coastal waters, and considering the UVR inhibition.

We quantified the phytoplankton photosynthetic potential for the illuminated layers of coastal areas (50 m) taking into account the global average depth of this zone [6]. We consider three representative latitudes proxies for equatorial (0^o), tropical (30^o) and subarctic (60^o) regions. The annual average solar spectral irradiances at these latitudes for PAR and UVR were used. In all cases cloudless skies were assumed. It was used Jerlov's optical coastal water classification [7], selecting types C1 (clearest) and C9 (darkest).

To compute the photosynthesis rates P at depth z (normalised to saturation rates P_s), we use a model for photosynthesis, typically employed with phytoplankton assemblages with good repair capabilities of UVR induced damages [8]:

$$\frac{P(z)}{P_s} = \frac{1 - \exp(-E_{PAR}(z)/E_s)}{1 + E^*_{UV}(z)}, \qquad (1)$$

where $E_{PAR}(z)$ and $E^*_{UV}(z)$ are the irradiances of PAR and UVR at depth z calculated following the procedure of [9].

The parameter E_s accounts for the efficiency with which the species uses PAR: the smaller its value, the greater the efficiency. We checked the two extremes, highest ($E_s = 2$ W/m^2) and lowest ($E_s = 100$ W/m^2) efficiency, such as in [9].

To consider more accurately the inhibitory effect of UVR on photosynthesis we used two biological weighting functions (BWF): one for temperate [10] and other for Antarctic phytoplankton [11]. These BWF account for both DNA damage and photosystem inhibition, resulting in whole-cell phytoplankton photosynthesis inhibition. The first BWF was used to calculate photosynthetic potential in equatorial and tropical zones, while the last one was used for subarctic zones.

This study has shown that coastal phytoplankton assemblages can be sensitive to high levels of UVB (280−319 nm) and UVA (320−399 nm) radiations in the first five meters of the water column approximately, where the photosynthetic potential can be depressed, but without total photoinhibition ($P/P_s = 0$).

UVR effects in aquatic ecosystems are distinguished by strong vertical gradients, so that most effects occur near the surface. This radiation is quite rapidly attenuated in the first meters of the water column and therefore can not penetrate to deeper water. On the other hand, PAR attenuation in deeper water has an important factor in the fall of photosynthetic potential. Considering these two restrictions, the highest photosynthetic potential will be reached at some intermediate depth, where the optimal balance UVR–PAR is achieved.

The exact depth of maximum photosynthetic potential depends on radiation intensity (latitude), optical water properties and sensitivity of the species to both UVR and PAR (Table 1). The highest photosynthetic potential is 100 % and it is reached by highly efficient species ($E_s = 2\ W/m^2$) in clearest coastal waters (C1) at both equatorial (0^o) and tropical (30^o) regions.

Table 1. Highest photosynthetic potentials reached at corresponding depths (m) between parentheses for generic coastal water columns of 50 m depth with different optical properties.

Latitude	$E_s = 2\ W/m^2$		$E_s = 2\ W/m^2$	
	C1	C9	C1	C9
0^o	100 (10-15)	99.6	78.6 (5)	41.5
30^o	100 (10-15)	99.0	72.3 (5)	45.8
60^o	99.9 (10)	90.8	47.2 (5)	27.1

Latitude determines the average annual irradiance at sea level, which diminish as one move from the Equator towards poles. However, our calculations showed similar potential for photosynthesis in equatorial and tropical regions (Figs. 1a and 1b). This can be explained by the fact that there is more PAR in the Equator, but also more (inhibitory) UVR, and some sort of compensation exists. For subarctic zones smaller photosynthesis potential was obtained (Fig. 1c). Actually, the sea waters of the 60^o latitude are usually rich in nutrients, yet, except in isolated regions, phytoplankton normally are scarce. Annual primary productivity is extremely low and it has frequently been suggested that it is limited by light, rather than by nutrients [12].

Table 2. Highest photosynthetic potentials reached at corresponding depths (m) between parentheses for generic coastal water columns of 50 m depth with different optical properties.

Latitude	$E_s = 2\ W/m^2$		$E_s = 2\ W/m^2$	
	C1	C9	C1	C9
0^o	67.7	14.7	21.9	4.7
30^o	65.8	14.8	20.2	5.0
60^o	55.7	11.9	11	2.9

As expected, in all scenarios the most efficient species assimilating PAR showed the highest photosynthetic potential, while the less efficient ones got minor potential (Fig. 1). Most efficient species show a relatively better adaptation to light scarcity in subarctic regions (their potentials are smaller in around 20 %); while for less efficient organisms rates are smaller in 40 – 50 % (Table 2).

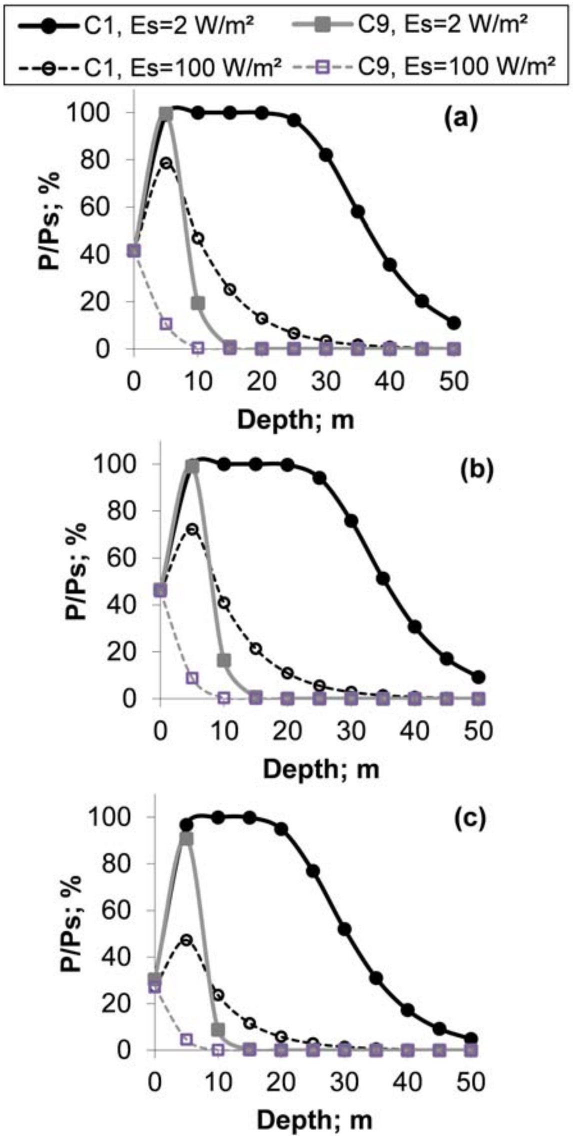

Figure 1. Photosynthetic potential for (a) 0^o, (b) 30^o and (c) 60^o latitude in different coastal optical water types.

In conclusions, UVR can stress photosynthetic process in the first five meters of the water column without total photoinhibition. In all scenarios the potential for clearest waters was around five times greater than for the darkest waters. Also, and interesting enough, for the same water type photosynthetic potentials in equatorial and tropical regions were approximately equal. Subarctic regions showed smaller potentials, being the less efficient organisms more affected.

We point out that this work is from the point of view of Ocean Optics. Further modeling would imply the inclusion of nutrients and probably other environmental variables to obtain a more accurate picture.

REFERENCES

[1] P. Falkowski, G.R. Barber and V. Smetacek, Science 281, 200 (1998).

[2] D.P. Häder, Plant Ecol. 128, 5 (1997).

[3] D.P. Häder, H.D Kumar, R.C. Smith and R.C. Worrest, Photochem. Photobiol. Sci. 6, 267–285, (2007).

[4] G.A. Hyndes, I. Nagelkerken, R.J. McLeod, R.M. Connolly, P.S. Lavery and M.A. Vanderklift, Biol. Rev. 89 (1), 232 (2014).

[5] I. Joint and M.B. Jordan, J. Plankton Res. 30 (2), 199 (2008).

[6] T.J. Agardy *et al.* In: In: R. Hassan, R. Scholes and N. Ash (Eds) Ecosystems and human well-being: current state and trends, Vol.1. Inland Press, Washington DC (2005) pp. 513-549.

[7] N.G. Jerlov, *Marine Optics*. (Elsevier Scientific Publishing Company, Amsterdam, 1976), pp. 232.

[8] J.J. Cullen, P.J. Neale, M.P. Lesser, Science 258, 646 (1992).

[9] L. Rodríguez, R. Cardenas and D. Avila-Alonso, Rev. Cub. Fis. 31, 15-17 (2014).

[10] P.J. Neale, private communication.

[11] J.J. Cullen and P.J. Neale, In: D.P. Häder (Ed) The Effects of Ozone Depletion on Aquatic Ecosystems, Landes, Austin (1997) pp. 97–118.

[12] M. M. Tilzer, W. W. Gieskes, R. Heusel and N. Fenton, Polar Biol. 14, 127 (1994).

DÍA INTERNACIONAL DE LA FÍSICA MÉDICA EN "EL CORTIJO"

Con una Jornada Científica realizada en el salón "El Cortijo" del Hotel Vedado fue celebrado el Día Internacional de la Física Médica el 7 de noviembre de 2015. La Jornada Conmemorativa "Física médica realidades y perspectivas" fue organizada por la Sociedad de Física Médica (sección de física médica de la Sociedad Cubana de Física), apoyado por la Organización Panamericana de la Salud (OPS), el Hospital Clínico Quirúrgico "Hermanos Ameijeiras" y Tema Sinergie. Contó con la presencia de 41 especialistas nacionales que expusieron los resultados de los trabajos científicos presentados este año en eventos nacionales e internacionales a propósito de las nuevas tecnologías, y la importancia de la física médica en su desarrollo.

Celebrando el Día Internacional de la Física Médica. Foto de grupo de los participantes en la celebración, el 7 de noviembre de 2015, a la salida del "El Cortijo" (Hotel Vedado, La Habana).

También estuvo presente una representación de la Sección Independiente para el Control de Cáncer y la Agencia de Energía Nuclear y Tecnologías de Avanzadas. Un rasgo distintivo de esta Jornada fue la amplia participación de los estudiantes de especialidades vinculadas con la temática, lo que demuestra el trabajo que realizan desde la etapa de pregrado, garantizando el relevo del recurso humano con un alto nivel de preparación.

Durante la jornada se expresó la preocupación por la necesidad de incrementar el número de físicos médicos en nuestros hospitales y la demanda creciente que existe de estos profesionales por la alta tecnología que se implementa en el país, así como el reto que posee la física médica al enfrentar estas nuevas tecnologías y la necesidad de efectuar cambios en la formación teórico práctica de la especialidad; aspecto éste en el que los proyectos de cooperación con el OIEA han venido jugando un papel importante. Para el próximo ciclo se desarrollaran 2 nuevos proyecto muy vinculados a la temática el CUB 6025 "Mejorar el diagnóstico y tratamiento de calidad para los pacientes de cáncer mediante la introducción de tecnologías avanzadas en Radioterapia y Medicina Nuclear" y el RLA 6077 "Acciones estratégicas destinadas a fortalecer las capacidades para el diagnóstico y el tratamiento del cáncer en forma integral en América Latina y el Caribe", en los marcos de los programas nacional y regional respectivamente y dirigidos a fortalecer las capacidades nacionales en esta especialidad.

Durante la clausura, la Dra. Teresa Romero (Jefa de la Sección Integral de Control del Cáncer), realizó un reconocimiento a la Sociedad Cubana de Física por el importante papel de estos eventos de actualización y debate científico, para el desarrollo de una cultura de seguridad y a favor de la integración multidisciplinaria que garantiza la calidad de la atención medica moderna. Reafirmó el compromiso de su sección de promover el reconocimiento del físico medico dentro del personal de salud con identidad propia, como un paso imprescindible para garantizar la sostenibilidad y uso óptimo de las nuevas tecnologías radiantes.

Tomado del sitio web de la
Agencia de Energía Nuclear y Tecnologías de Avanzada
http://www.aenta.cu/7-de-noviembredia-internacional-de-la-fisica-medica/

ALTO BRILLO EN EL HOTEL NACIONAL

Como parte de una serie de talleres sobre la "Física y las Aplicaciones de Haces de Alto Brillo", se celebró en el Hotel Nacional de Cuba la última edición del evento, del 28 de marzo al 1 de abril de 2016.

Con el objetivo de contribuir a los intereses nacionales en el campo de las aplicaciones biomédicas de la Física Nuclear, el evento hizo énfasis en este tema, e incluso sirvió como marco para el posible comienzo de una iniciativa de cooperación pan-Caribeña asociada a lo que los organizadores bautizaron con la Fuente de Luz Cubana. Se aprovechó el marco del evento para celebrar los logros científicos del profesor emérito de la Universidad de California en Los Ángeles (USA) Claudio Pellegrini –creador del Láser de Electrones Libres de Rayos X (X-ray FEL), que ha cambiando los paradigmas instrumentales en su campo.

El evento fue co-presidido por J. Rosenzweig (UCLA, USA) y M. Ferrario (INFN-LNF, Italia), mientras que F. Castro-Smirnov (INSTEC) fungió como organizador local. Contó con la participación de más de una treintena de participantes cubanos, y números similares de estadounidenses, y de europeos. Entre los participantes cubanos, destacó la asistencia de muchos jóvenes estudiantes de postgrado y de pregrado.

E. Altshuler

ENTREGADOS PREMIOS DEL CONCURSO *CIENCIARTE* 2015

El martes 2 de febrero de 2016 se dieron a conocer los resultados del concurso de fotografía científica *CienciArte* 2015 en el lobby de la facultad de Artes y Letras de la Universidad de la Habana. El concurso convocado por la Sociedad Cubana de Física, la Facultad de Física y el Instituto de Ciencia de Materiales (IMRE), de la Universidad de la Habana, tenía como objetivo divulgar la ciencia y la tecnología a través de imágenes artísticas con contenido científico. El jurado estuvo integrado por el fotógrafo Ricardo Miguel Hernández, el Dr. José Antonio Baujín Pérez, director de la Editorial UH, y el Máster en Ciencias Físicas Arturo Abelenda García.

Las obras y autores premiados, fueron:

I Categoría *Distinguiendo el micromundo*

Primer lugar:

Título: *El arte de los colibríes.*

Autores: Omar Concepción Díaz, Facultad de Física, Universidad de La Habana y Odín Vázquez Robaina, IMRE, Universidad de la Habana.

Segundo lugar:

Título: *Variaciones sobre un ramillete de nanohilos alado.*

Autores: Osvaldo de Melo y Patricia Gutiérrez, Facultad de Física, Universidad de la Habana.

Tercer lugar:

Título: *Los Fantasmas del Alma.*

Autor: Lázaro Pérez Acosta, Universidad de Camagüey.

Mención:

Título: *Nano pacman.*

Autor: Javier Martínez Pons, Odín Vázquez Robaina, Abel Fundora, Oscar Nápoles y Mayra Hernández Sánchez, IMRE, Universidad de La Habana.

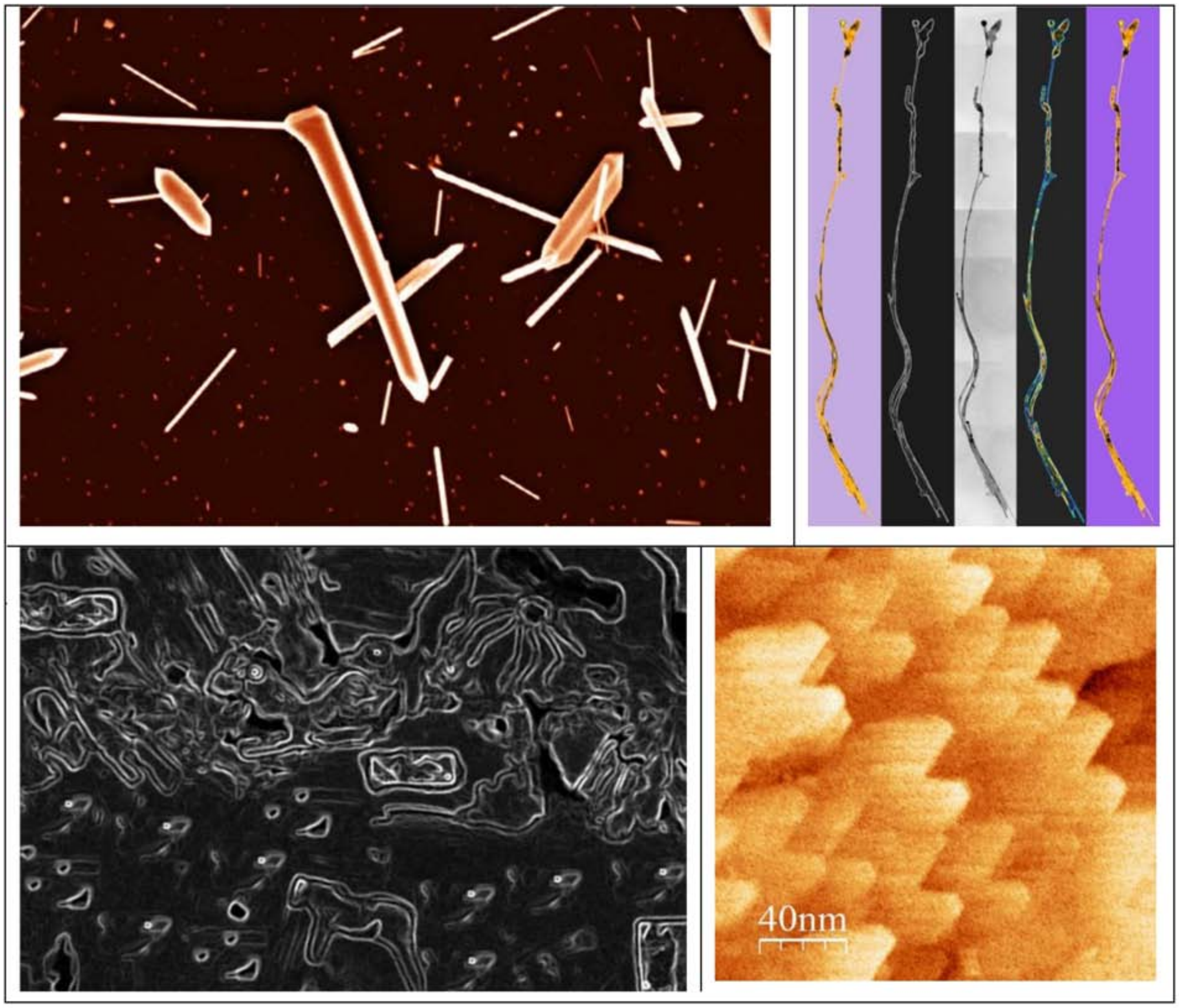

Distinguiendo el micromundo. A la izquierda, arriba: *El arte de los colibríes* (primer lugar). A la derecha, arriba: *Variaciones sobre un ramillete de nanohilos alado* (segundo lugar). A la izquierda, abajo: *Los fantasmas del alma* (tercer lugar). A la derecha, abajo: *NanoPacman* (Mención).

II Categoría *Vislumbrando el entorno visual y natural*

Primer lugar

Título: *El principio.*

Autor: Karla Betancourt Rodríguez, Instituto Superior de Arte.

Segundo lugar

Título: *Luz sobre las tres fases.*

Autores: L. Domínguez Rubio, E. Martínez y E. Altshuler, Facultad de Física, Universidad de la Habana.

Tercer lugar

Título: *Anverso y reverso.*

Autor: Karla Betancourt Rodríguez, Instituto Superior de Arte.

Vislumbrando el entorno visual y natural. A la izquierda: *El principio* (primer lugar). A la derecha, arriba: *Luz sobre las tres fases* (segundo lugar). A la derecha, abajo: *Anverso y Reverso* (tercer lugar).

DÍA DE LA FÍSICA EN LA UNIVERSIDAD CENTRAL DE LAS VILLAS

El viernes 18 de diciembre de 2015 se celebró el Día de la Física en la Universidad Central "Marta Abreu" de Las Villas (UCLV). Esta conmemoración es tradicionalmente realizada en el entorno del 14 de diciembre de cada año, en honor a la presentación de Max Planck de su interpretación cuántica de la radiación electromagnética ante la Sociedad Alemana de Física. Esto sucedió el 14 de diciembre de 1900, fecha que muchos consideran como la del nacimiento de la Física Cuántica.

En esta ocasión en gran medida se pretendió estimular a trabajadores, estudiantes y colaboradores del Dpto. Física-UCLV por su aporte a dos retadores procesos enfrentados este año, la acreditación de la carrera de Física durante la segunda semana de noviembre y la evaluación institucional durante la última semana del mismo mes.

La actividad comenzó con las palabras de la Dra. C. Kenia Herrera Lemus, Jefe del Departamento de Física, quien hizo un balance de los principales logros del Dpto. en el año 2015.

Posteriormente se presentó una propuesta extensionista en la que el Dpto. está involucrado: la declaración de un Sitio Geológico en el Parque Natural Capiro, lo cual pretende proteger el estratotipo allí descubierto hace pocos años, que marca la transición entre los períodos Cretácico y Paleógeno. Esta transición fue determinada por el impacto del asteroide de Chicxulub hace 65 millones de años, huellas de lo cual se aprecian en el mencionado parque. Se señaló que en estos momentos varias circunstancias pueden coadyuvar a que se realice este proyecto, tales como la reciente aprobación en la UCLV de un grupo afiliado a la Sociedad Geológica de Cuba y la existencia de una Cátedra UNESCO en la mencionada universidad.

A continuación se otorgó la Distinción "Físico por Excelencia" a Rafael Quintana Puchol, Profesor Titular de la UCLV, Doctor en Ciencias, Doctor en Ciencias Técnicas Geológicas y Licenciado en Química. Esta distinción tradicionalmente se otorga en el Dpto. a profesionales que no trabajan en este, pero que se considera han aportado al desarrollo de la Física en la UCLV.

Posteriormente la sección sindical informó de los trabajadores más destacados del año y se entregaron los correspondientes diplomas. Además se planteó que la sección sindical fue seleccionada vanguardia en el año.

La Decana de la Facultad, Dra. C. Yanet Rodríguez Sarabia, felicitó al Dpto. por los logros del año.

Finalmente los miembros del Dpto. se incorporaron a las actividades desarrolladas en la UCLV por el Día del Educador.

Departamento de Física,
Universidad Central de Las Villas

FÍSICA PARA EL 2021

El martes 24 de mayo de 2016 la Sección de Enseñanza de la Física de la Sociedad Cubana de Física convocó a una reunión para discutir sobre los nuevos programas de Física a nivel de Secundaria Básica y Preuniversitario que están siendo elaborados, y que deben entrar en vigencia en el país en el año 2021. Presidida por el profesor Carlos Sifredo, en la reunión participaron dos decenas de profesores y metodólogos del Ministerio de Educación, a los que se sumó una pequeña representación del Ministerio de Educación Superior. Los jóvenes profesores Maikel Ortiz (de Sancti Spíritus) y Arturo Gómez (de Camagüey) expusieron el consistente trabajo realizado hasta el momento para conformar el nuevo plan de estudios.

Conformando la enseñanza de la Física a partir del 2021. El profesor espirituano Maikel Ortiz explica el trabajo que, en conjunto con el camagüeyano Arturo Gómez y otros colegas, se está realizando para renovar los programas de enseñanza de la Física en Cuba desde 8^{vo} hasta 12^{mo} grados. La escena tuvo lugar en el Instituto Superior de Diseño, el 24 de mayo de 2016 (Foto: E. Altshuler).

Entre otros muchos temas, se hizo énfasis en la importancia de la Física Experimental consistente en problemas experimentales no-reproductivos, como un pilar fundamental en la nota final de los estudiantes. En la discusión posterior a la presentación, resultó haber consenso en el hecho de que la principal dificultad en el futuro de la enseñanza de la Física en Cuba no es la falta de recursos económicos en forma de equipamiento de laboratorio, sino en la falta de personal calificado para llevar adelante los nuevos programas a lo largo y ancho de la isla. Próximamente se realizarán ensayos pilotos de los nuevos programas de Física, en un conjunto de escuelas en todo el país.

E. Altshuler

LA OLIMPIADA UNIVERSITARIA DE FÍSICA SE EXPANDE POR LATINOAMÉRICA

Organizada por la Sociedad Cubana de Física y la Facultad de Física de la Universidad de la Habana y con el coauspicio de la UNESCO y el CLAF, el 18 de marzo de 2016 tuvo lugar la cuarta Olimpiada Nacional Universitaria de Física.

En la competencia participaron 64 estudiantes: 18 de la Universidad de La Habana, 11 del Instituto Superior de Tecnologías y Ciencias Aplicadas (InSTEC), uno de la Universidad de Oriente, 5 de la Universidad Central de Las Villas, 6 de la

Universidad de Camagüey y 3 de la Universidad de Holguín.

En esta ocasión participaron también estudiantes foráneos, 10 de la Universidad Nacional Autónoma de México (UNAM), 8 de la Universidad Federal de Minas Gerais (UFMG) en Brasil y dos la Universidad de El Salvador.

El examen constó de 5 problemas de Física general de nivel universitario elaborados por destacados profesores e investigadores cubanos:

- Dr. Osvaldo de Melo Pereira, Facultad de Física, Universidad de la Habana.
- Dr. Alejandro Cabo Montes de Oca, Instituto de Matemática, Cibernética y Física (ICIMAF)
- Lic. Héctor Borroto Gutiérrez, Facultad de Física, Universidad de la Habana.
- M.C. Julio C. Drake Pérez, Facultad de Física, Universidad de la Habana.
- Lic. Fermín Rodríguez Hernández, Facultad de Física, Universidad de la Habana.
- Lic. Luis Felipe Ponce Álvarez, Centro de Inmunología Molecular (CIM).

Algunos de los protagonistas de la ONUF'16. De izquierda a derecha Alejandro Alfonso Yero, José Rubiera Gimeno, Marcos Espinosa, Rafael Sosa Ricardo; Ismael Rodríguez Cuéllar, Yamil Divó Matos, Juan Carlos Acosta Matos, María Sánchez-Colina, Hernán Fernández, David Machado, Danyer Pérez, y Joan Nieves Cuadrado. (Foto: E. Altshuler).

Resultados IV Olimpiada Universitaria de Física, ONUF 2016

	Nombre	**Carrera y Universidad**	**Medalla**
1	Alejandro Lázaro Alfonso Yero	3er año. Ingeniería Automática Universidad Central de las Villas, Cuba	ORO
2	Jorge Torres Ramos	3er año. Licenciatura en Física, Universidad Nacional Autónoma de México	ORO
3	Danyer Pérez Adán	5to año. Licenciatura en Física Nuclear, **INSTEC**, Cuba	ORO
4	Siddharta E. Morales Guzmán	2do año. Licenciatura en Física, Universidad Nacional Autónoma de México	ORO
5	Hernán Fernández García	1er año. Licenciatura en Física, Universidad de la Habana, Cuba	PLATA
6	Rafael Eduardo Sosa Ricardo	4to año. Licenciatura en Física Nuclear, **INSTEC**, Cuba	PLATA
7	Joan Andrés Nieves Cuadrado	1er año. Licenciatura en Física, Universidad de la Habana, Cuba	PLATA
8	Eduardo E. García Reynaldo	3er año. Licenciatura en Física, Universidad de la Habana, Cuba	BRONCE
9	José A. Rubiera Gimeno	2do año. Licenciatura en Física Nuclear, **INSTEC**, Cuba	BRONCE
10	Christian A. Benítez Abarca	2do año. Licenciatura en Física, Universidad Nacional Autónoma de México	BRONCE
11	David Machado Pérez	2do año. Licenciatura en Física, Universidad de la Habana, Cuba	BRONCE
12	Marcos Espinosa Cuartas	1er año. Licenciatura en Física, Universidad de la Habana, Cuba	BRONCE
13	Ailier Rivero Acosta	3er año. Licenciatura en Física, Universidad Central de las Villas, Cuba	BRONCE
14	Eduardo Leite Lima	Universidad Federal de Minas Gerais, Brasil	BRONCE
15	Carlos E. Fernández Noa	3er año. Licenciatura en Física, Universidad Central de las Villas, Cuba	BRONCE
16	Yamil E. Divó Matos	5to año. Licenciatura en Física Nuclear, INSTEC, Cuba	BRONCE
17	Guillermo Mauricio Rivera Alfaro	1er año Ingeniería Eléctrica, Universidad de El Salvador	BRONCE
18	Juan C. Acosta Matos	2do año. Licenciatura en Física, Universidad de la Habana, Cuba	BRONCE
19	Ismael Rodríguez Cuéllar	2do año. Licenciatura en Física, Universidad de la Habana, Cuba	BRONCE

Los profesores responsables de organizar la olimpiada en las universidades extranjeras participantes fueron:

- Dr. Victor Romero Rochín. Instituto de Física (UNAM).
- Dr. Fernando Augusto Batista (UFMG).
- Br. Adverdi Ventura, Coordinador de Física, Programa Jóvenes Talento de la Universidad de El Salvador.

Los estudiantes ganadores se resumen en la tabla.

Felicitamos a todo los ganadores, que, además, demostraron cómo se puede escalar el podio de la ONUF no sólo desde Cuba, sino desde cualquier país.

María Sánchez-Colina
Presidente, Comité Organizador ONUF IV

MATHEMATICA NOS VISITA

Seminario científico con estudiantes y profesores de la facultad de física brindado por el representante de Wolfram Research, en el Salón "250 Aniversario" de la Universidad de La Habana (Foto: A. Pentón).

Del 9 al 15 de marzo visitó nuestro país, a partir de una invitación de la Sociedad Cubana de Física, el Sr. Roy Álvarez, representante para Latinoamérica y el Caribe de Wolfram Research (WR). Durante su estancia visitó la Facultad de Física de la Universidad de la Habana, e intercambió experiencias con usuarios del programa Mathematica –producido por WR-.

Se desarrolló un seminario donde, entre otras cosas, estudiantes y profesores expusieron parte de los resultados de su trabajo docente y de investigación haciendo uso de Mathematica. Como resultado de la visita se logró un acuerdo en el que la Wolfram Research le cede a la Facultad de Física de la Universidad de La Habana una licencia para operar Mathematica 10.4 por un período inicial de tres meses y prorrogable cada tres meses hasta que la ley del bloqueo se elimine. Llegado ese momento, la licencia sería indefinida. En este momento se encuentra instalada la versión Mathematica 10.4 en las 10 máquinas del laboratorio de computación y se distribuyeron entre profesores y alumnos un conjunto de licencias individuales.

Se acordó igualmente realizar para inicios del próximo año un taller orientado a exponer aplicaciones desarrolladas sobre Mathematica, así como impartir cursos afines a esta herramienta. Se gestionó la posibilidad de que nuestros profesores reciban la certificación Wolfram Research, para lo cual deben pasar un examen. Esto permitiría, por ejemplo, poder recibir estudiantes de nuestra área geográfica para formarlos y entrenarlos en el uso de Mathematica.

Dr. Arbelio Pentón
Facultad de Física
Universidad de La Habana

EL VII TIBERO, EN SAN GERÓNIMO

Superconductividad en la Enseñanza de la Física. Laura Green, Presidenta electa de la American Physical Society, imparte la conferencia inaugural del VII TIBERO, titulada "High T_c Superconductivity: taming serendipity" (foto: E. Altshuler).

Del 7 al 11 de marzo del 2016, sesionó en el Colegio Universitario San Gerónimo de La Habana, La Habana, Cuba, el VII Taller Iberoamericano de Enseñanza de la Física Universitaria (TIBERO 2016) y el XXXIII Curso Centroamericano y del Caribe de Física (CURCCAF) respectivamente. El evento TIBERO 2016 tuvo como tema central "La Física y los problemas ambientales". Entre los conferencistas invitados se encontraban Laura Green (National High Magnetic Field Lab, USA), Manuel Yuste (UNED, España), Betsabeé Marel Monroy (UNAM, México), Jaime Santoyo Salazar. (IPN, CINVESTAV, México), Guillermo Santana (UNAM, Máxico), y los profesores de la Universidad de la Habana Ernesto Altshuler, Melquiades de Dios, Osvaldo de Melo y Elena Vigil (Universidad de la Habana, Cuba).

En el CURCCAF se impartieron dos cursos de actualización en temas de enseñanza de la Física: (a) Nuevo enfoque de la Termodinámica basado en la entropía como medida del calor. Dr. Friedrich Herrmann, Karlsruhe University, Alemania y (b) Temas selectos de la enseñanza de Mecánica a nivel universitario. Prof. Raúl Portuondo Duany, Catedrático Departamento de Física, Universidad de Mayagüez, Puerto Rico.

Dr. Octavio Calzadilla
Facultad de Física
Universidad de La Habana

DE CAYO HUESO A LA UNIVERSIDAD DE LA HABANA: EUDALDO R. GARCÍA TARAJANO

(11 mayo 1936 - 18 enero 2015)

Quien viera a Tarajano, tan jovial y sereno, tan entusiasta y dispuesto a ciertas formas de la aventura, no habría podido calcular su edad ni imaginar los numerosos avatares de su vida. El desconocedor de su historia no habría sabido, viéndolo tan comprometido y participante en nuestra Facultad, que antes de ser físico se graduó de ingeniero; ni viéndolo tan criollo adivinar que sus padres eran españoles, ni que había recibido formación y trabajo en diferentes lugares del mundo.

Eudaldo Rolando García Tarajano (1937-2015)

A pesar de su progenitura, Eudaldo Rolando García Tarajano, quien seguramente perdió temprano sus dos nombres y su primer apellido, para ser solo el Tara, era —cosa rara hoy día— habanero, pero no de las zonas del Vedado o Miramar, como nos podía hacer esperar su natural elegancia, sino de Cayo Hueso, de las mismas entrañas del pueblo, y desde muy temprano se vio obligado a trabajar para vivir: hoy como ayudante de bodega, mañana de carpintero, al día siguiente de mandadero, y un montón de pequeñas labores con remuneraciones aún más pequeñas.

Pero Tarajano siempre comprendió la necesidad de estudiar: la enseñanza general primero, luego comercio. Quien viera al capaz profesor universitario que fue después, no hubiera sabido que realizó sus estudios universitarios de día, mientras realizaba trabajos de contabilidad y de operador nocturno en la compañía de teléfonos.

Para él, como para todos, el triunfo de la Revolución significó una subversión de su vida anterior. De la conciliación de sus intereses con las necesidades de aquel entonces, surgió la extraña situación de que estudiaba ingeniería eléctrica, al tiempo que impartía clases de Física en nuestra Universidad, hacía labores de seguridad, intervenía instituciones privadas, se movilizaba cuando la Crisis de Octubre, o era delegado de los estudiantes de su curso.

Al graduarse de su primera carrera fue enviado a fundar la de Física en la Universidad Central “Martha Abreu” de Las Villas, adonde regresó para servir un curso más como subdirector y director, después de cuatro años de estudios en la Cátedra de Física teórica en la casa de altos estudios de Kíev, en la antigua URSS. Pero la Universidad de La Habana será su entrañable alma mater: a ella regresará, y allí permanecerá como profesor desde el curso 1974-75 hasta su jubilación, aunque distintas ciudades recibieron también sus conocimientos y su huella: de Moscú a León en Nicaragua, de Kíev a Zacatecas, de Monterrey o Pachuca.

Dispuesto y presente, hizo lo que hacía falta: impartió Electromagnetismo, pero también Mecánica, Óptica, Termodinámica, Física Molecular. Fue jefe de departamento, vicedecano, coordinador de maestrías, dirigente sindical, asesor, tutor, y su amor más constante fue la investigación sobre las propiedades magnéticas de las ferritas.

Pero para saber realmente quién era esta persona, bastaría leer los correos electrónicos que circularon cuando se supo la noticia triste de su muerte. Su esposa dice que no quería que hicieran nada ni molestar a nadie. Alguien no comprende lo sucedido porque acaba de verlo en la Facultad, otro recuerda que se llevaba bien con todos, por su humildad y trato amable. Hay quien hace anécdotas de cuando organizó grupos de jóvenes mexicanos que vinieran a estudiar a Cuba, o cuando reunió a quienes habían sido maestros voluntarios y se los llevó como homenaje a escalar el Pico Turquino, y quien habla de su condición de fundador de uno de los seis grupos de investigación que se iniciaron en la Facultad, allá por la década de los 1970s.

A Tarajano, entonces, le debemos todos. Pero no silencio y tristeza, sino el aplauso por su vida alegre y útil, en que amó y crió hijos aunque no fueran suyos, y cultivó la familia, una grande de la que son parte no solo su esposa, sus hijos, sobrinos y seres más cercanos, sino también nosotros, por el derecho de la profesión y del afecto, y por el deber de continuar las tareas que dejó sin completar.

Julio Vidal,
Departamento de Física General,
Facultad de Física,
Universidad de La Habana

Revista Cubana de Física
ISSN 0253-9268
Online ISSN 2224-7939

Revista Cubana de Física
ISSN 0253-9268
Online ISSN 2224-7939

Revista Cubana de Física
ISSN 0253-9268
Online ISSN 2224-7939